

**Best  
Available  
Copy**

AD-772 639

COHERENT OPTICAL ADAPTIVE TECHNIQUES  
(COAT)

P. T. Brunner, et al

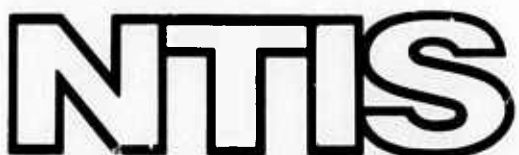
Hughes Research Laboratories

Prepared for:

Rome Air Development Center  
Defense Advanced Research Projects Agency

July 1973

DISTRIBUTED BY:



National Technical Information Service  
U. S. DEPARTMENT OF COMMERCE  
5285 Port Royal Road, Springfield Va. 22151

AD - 772 639

UNCLASSIFIED

SECURITY CLASSIFICATION OF THIS PAGE (When Data Entered)

REPORT DOCUMENTATION PAGE		READ INSTRUCTIONS BEFORE COMPLETING FORM
1. REPORT NUMBER RADC-TR-73-384	2. GOVT ACCESSION NO.	3. RECIPIENT'S CATALOG NUMBER
4. TITLE (and Subtitle) Coherent Optical Adaptive Techniques (COAT) (U)		5. TYPE OF REPORT & PERIOD COVERED Interim 27 Mar to 26 Jun 73
7. AUTHOR(s) P.T. Brunner S.P. Lazzara T.A. Ilussmeier		6. PERFORMING ORG. REPORT NUMBER Technical Report No. 1
9. PERFORMING ORGANIZATION NAME AND ADDRESS Hughes Aircraft Co. Hughes Research Labs 3011 Malibu Canyon Rd Malibu, Calif. 90265		8. CONTRACT OR GRANT NUMBER(s) F30602-73-C-0248
11. CONTROLLING OFFICE NAME AND ADDRESS DARPA 1400 Wilson Blvd Arlington, Va. 22209		10. PROGRAM ELEMENT, PROJECT, TASK AREA & WORK UNIT NUMBERS Program Code: 3E20 12790016
14. MONITORING AGENCY NAME & ADDRESS (if different from Controlling Office) Rome Air Development Center (OCTM) Griffiss AFB, NY 13441		12. REPORT DATE July 1973
		13. NUMBER OF PAGES 116
		15. SECURITY CLASS. (of this report) UNCLASSIFIED
		15a. DECLASSIFICATION/DOWNGRADING SCHEDULE
16. DISTRIBUTION STATEMENT (of this Report) Approved for Public Release. Distribution Unlimited.		
17. DISTRIBUTION STATEMENT (of the abstract entered in Block 20, if different from Report)		
18. SUPPLEMENTARY NOTES Robert F. Ogrodnik OCTM AC315 330-4306		
Reproduced by NATIONAL TECHNICAL INFORMATION SERVICE U.S. Department of Commerce Springfield VA 22151		
19. KEY WORDS (Continue on reverse side if necessary and identify by block number) COAT Atmospheric Turbulence Optical Radar Active Optics Phased Arrays Optical Phase-Shifters Adaptive Systems Computer Simulation		
20. ABSTRACT (Continue on reverse side if necessary and identify by block number) Coherent optical adaptive techniques (COAT) can be applied to overcome the deleterious effects of atmospheric turbulence. This report covers the design phase of an experimental program to design, fabricate and evaluate an eighteen-element, self adaptive, optical phased array. In addition, a computer simulation program developed to aid in system design and performance prediction is also described. Results are presented on preliminary experiments (cont.)		

DD FORM 1 JAN 73 1473 EDITION OF 1 NOV 65 IS OBSOLETE

UNCLASSIFIED

SECURITY CLASSIFICATION OF THIS PAGE (When Data Entered)

UNCLASSIFIED

SECURITY CLASSIFICATION OF THIS PAGE(When Data Entered)

Item 13. Abstract (cont.)

performed with an existing seven-element COAT system. Further experiments were performed with different piezoelectric ceramic phase-shifter configurations and with improved servo control electronic systems and are described here. Techniques for offset pointing of the phased array are discussed. A flexible phaser matrix structure is described in which radiating array patterns can be easily changed. Atmospheric characterization measurements performed on the 94 meter test range are described. The design of a dynamic multiglint target system is given. Parameters are listed for the experimental equipment to be fabricated during the next phase of the program. Calibration and on-range measurements for the final phase of the program are described.

UNCLASSIFIED

SECURITY CLASSIFICATION OF THIS PAGE(When Data Entered)

ia

**COHERENT OPTICAL ADAPTIVE TECHNIQUES (COAT)**

P. T. Brunner  
S. P. Lazzara  
T. A. Nussmeier  
T. R. O'Mera  
T. J. Walsh

**Contractor:** Hughes Aircraft Company  
**Contract Number:** F30602-73-C-0248  
**Effective Date of Contract:** 27 March 1973  
**Contract Expiration Date:** 26 March 1974  
**Amount of Contract:** \$249,648.00  
**Program Code Number:** 3E20

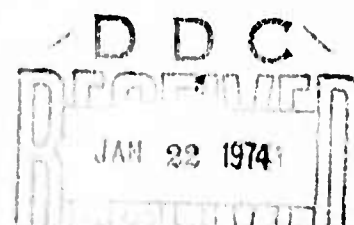
**Principal Investigator:** W. B. Bridges  
**Phone:** 213 456-6411

**Project Engineer:** Robert F. Ogrodnik  
**Phone:** 315 330-4306

**Contract Engineer:** Robert Hawkins  
**Phone:** 315 330-4731

**Approved for public release;  
distribution unlimited.**

This research was supported by the Defense Advanced Research Projects Agency of the Department of Defense and was monitored by Robert F. Ogrodnik, RADC (OCTM), GAFB, NY 13441 under contract F30602-73-C-0248.



## FOREWORD

This quarterly report was prepared by Hughes Research Laboratories, Malibu, California, under Contract No. F30602-73-C-0248. It describes work performed from 27 March to 26 June 1973. The principal investigator and principal scientist is Dr. William B. Bridges.

## SUMMARY

Coherent Optical Adaptive Techniques (COAT) can be used to provide near-diffraction-limited laser beam propagation through the atmosphere to desired target points even in the face of distorting agents: a turbulent atmosphere, target motion, mechanical vibration of the transmitter optics, internal phase distortions in the source laser, etc. It also seems likely that COAT systems will reduce the distortion resulting from non-linear propagation effects such as thermal blooming.

There are two primary objectives of the present program. The first objective is to determine experimentally the performance limits of coherent optical adaptive techniques through operation of an experimental, visible prototype COAT system through a representative turbulent atmosphere against a complex dynamic target. The second objective is to determine the best methods of employing COAT in high power laser systems and to assess the status of necessary key high power components.

During the first quarter, analyses for several aspects of the COAT system have been carried out. A computer simulation has been written and successfully compared with the experimental performances obtained on the existing 3-element system. The computer program was used to study the influence of the system parameters (e.g. modulation index, loop gain, filter specifications, array distribution) on overall performance.

A variety of piezoelectric drivers for phase shifter use have been evaluated for improved characteristics. A one-half inch diameter, PZT bimorph has been selected for the control phase shifter and a one-half inch diameter by one inch long PZT cylinder for the tagging phase shifter.

A new version of the control system electronics has been breadboarded and has demonstrated greatly improved performance in a two-element COAT test fixture.

A dc type automatic gain control system with over 50 dB dynamic range has been developed. A new type of optomechanical beam splitter/combiner arrangement has been conceived and demonstrated by construction and alignment of an 8-element model.

A design for a versatile dynamic target system employing glints with integral detectors has been developed. A video recording system with a level quantizer has been specified as the prime on-range data recording system.

Two high-speed microthermometers, a laser scintillometer and a photographic MTF system have been built to use for atmospheric turbulence characterization on the outdoor range.

#### PUBLICATION REVIEW

This technical report has been reviewed and is approved.

Robert F. Ogrodnik

Robert F. Ogrodnik  
RADC Project Engineer

## ABSTRACT

Coherent optical adaptive techniques (COAT) can be applied to overcome the deleterious effects of atmospheric turbulence. This report covers the design phase of an experimental program to design, fabricate and evaluate an eighteen-element, self-adaptive, optical phased array. In addition, a computer simulation program developed to aid in system design and performance prediction is also described. Results are presented on preliminary experiments performed with an existing seven-element COAT system. Further experiments were performed with different piezoelectric ceramic phase-shifter configurations and with improved servo control electronic systems and are described here. Techniques for offset pointing of the phased array are discussed. A flexible phasor matrix structure is described in which radiating array patterns can be easily changed. Atmospheric characterization measurements performed on the 94 meter test range are described. The design of a dynamic multiglint target system is given. Parameters are listed for the experimental equipment to be fabricated during the next phase of the program. Calibration and on-range measurements for the final phase of the program are described.

## TABLE OF CONTENTS

FOREWORD . . . . .	ii
SUMMARY . . . . .	iii
ABSTRACT . . . . .	v
LIST OF ILLUSTRATIONS . . . . .	viii
LIST OF TABLES . . . . .	xi
I. INTRODUCTION. . . . .	1
A. Program Objectives . . . . .	1
B. Research Program Plan . . . . .	1
C. Organization of This Report . . . . .	2
II. ANALYSIS . . . . .	3
A. Philosophy of Analytical Tasks . . . . .	3
B. Seven-Element System Experiments . . . . .	4
C. Computer Simulation. . . . .	11
D. Beam Offset Techniques . . . . .	40
E. Alignment Error Analysis . . . . .	44
III. DESIGN . . . . .	51
A. Phasor Matrix . . . . .	51
B. Phase Shifters and Taggers . . . . .	59
C. Electronic Design. . . . .	67
D. Overall Transmitter/Receiver Specifications . . . . .	78
E. Array Pattern Design . . . . .	81
F. Range Design . . . . .	85
G. Target Design . . . . .	89
H. Instrumentation . . . . .	96
IV. MEASUREMENT PROGRAM. . . . .	101
A. Calibration Measurements . . . . .	101
B. On-Range Measurements . . . . .	101
V. PLANS FOR THE NEXT QUARTER . . . . .	107
APPENDIX I - Incremental Open Loop Gain . . . . .	109
DD FORM 1473	

**Preceding page blank**

## LIST OF ILLUSTRATIONS

Fig. 1.	COAT tasks and scheduling . . . . .	1
Fig. 2.	Arrangement used to determine convergence time of the seven-element COAT system . . . . .	5
Fig. 3.	Power on the glint and power returned to the COAT receiver . . . . .	7
Fig. 4.	Three measurements of the convergence process with nominally identical condition, showing the statistical nature of convergence process . . . . .	8
Fig. 5.	Moving glint measurements . . . . .	10
Fig. 6.	COAT functional flow chart for simulation. . . . .	12
Fig. 7.	Computer program block diagram for COAT simulation . . . . .	13
Fig. 8.	Two element COAT quantities as a function of the total phase difference between channels . . . . .	18
Fig. 9.	Typical computer output showing power on the glint . . . . .	21
Fig. 10.	Definitions of quantities used in analyzing computer runs . . . . .	27
Fig. 11.	Glint initial conditions for 1 x 9 and 4 x 4 array computations . . . . .	28
Fig. 12.	Final target plane power distribution for Run 4-4 . . . . .	34
Fig. 13.	Glint power as a function of dither modulation for a 1 x 9 element array . . . . .	35
Fig. 14.	System gain and convergence time as a function of modulation . . . . .	36
Fig. 15.	Dither feedthrough and synchronism for a 1 KHz dither spacing . . . . .	38
Fig. 16.	Dither feedthrough for 1.5 KHz dither spacing . . . . .	39
Fig. 17.	Intensity plot of far-field pattern from planar 4 x 4 array of contiguous square elements . . . . .	41

Fig. 18.	Target plane square-element array power pattern	42
Fig. 19.	Electronic beam offset system	45
Fig. 20.	(a) Phase-shifter drive voltage on channel No. 1	46
Fig. 20.	(b) Phase-shifter drive voltage on channel No. 2	46
Fig. 21.	Phase-shifter drive, channel No. 1	46
Fig. 22.	Power loss from random phase and amplitude errors	48
Fig. 23.	Peak power loss from element positioning errors	50
Fig. 24.	Sketch illustrating how an elemental pattern is removed from the beam	52
Fig. 25.	COAT phasor matrix array optomechanical test	54
Fig. 26.	8-element phasor matrix test setup	55
Fig. 27.	Output beam from 8-element test setup	56
Fig. 28.	Mask layout for 8 x 8 thinned arrays	57
Fig. 29.	Mask layout for 0-6-12 array	58
Fig. 30.	Phase shifter resonance effects	60
Fig. 31.	1 in. diameter bimorph response	62
Fig. 32.	Response of 1 in. and 1/2 in. bimorphs compared	64
Fig. 33.	A passive notch filter with the characteristics shown has been introduced to partially compensate the bimorph resonance	64
Fig. 34.	Tagger configurations	66
Fig. 35.	18-element system block diagram	68
Fig. 36.	Single channel test system	68
Fig. 37.	Single channel COAT test interferometer	69

Fig. 38.	<b>Basic AGC system</b>	71
Fig. 39.	<b>Chopper stabilized or 30 MHz upconversion AGC</b>	72
Fig. 40.	<b>Measured AGC performance</b>	73
Fig. 41.	<b>Breadboard 30 MHz upconversion AGC system</b>	74
Fig. 42.	<b>Element electronics</b>	75
Fig. 43.	<b>Measured breadboard transient response</b>	77
Fig. 44.	<b>Overall layout of COAT transmitter and receiver components</b>	80
Fig. 45.	<b>Rectangular 1 x 9 array</b>	82
Fig. 46.	<b>Rectangular 4 x 4 array</b>	83
Fig. 47.	<b>Axisymmetric 0-6-12 array</b>	84
Fig. 48.	<b>Pseudo random 18-element array on 8 x 8 grid</b>	86
Fig. 49.	<b>Recordings of the dual temperature probe bridge rms output</b>	88
Fig. 50.	<b>Glint return spatial distribution measurements</b>	91
Fig. 51.	<b>Glint return spatial distribution measurements</b>	92
Fig. 52.	<b>Schematic cross-section of cat's eye glint</b>	93
Fig. 53.	<b>Three-glint mounting for multiglint target</b>	94
Fig. 54.	<b>Overall target configuration</b>	95
Fig. 55.	<b>Instrumentation and recording system</b>	97
Fig. 56.	<b>Target simulator and diagnostic sensors</b>	98
Fig. 57.	<b>Target plane beam recording panel</b>	99

## LIST OF TABLES

Table

I	Hardware/Simulation Comparison . . . . .	20
II	1 x 9 Array Configuration . . . . .	23
III	4 x 4 Array Configuration . . . . .	24
IV	Gain Values for Initial Simulation Runs . . . . .	25
V	Summary of 1 x 9 Linear Array Data for a Two Glint and Modified Two Glint Configuration . . . . .	30
VI	Summary of 4 x 4 Planar Array Data for a Two Glint and Modified Two Glint Configuration . . . . .	31
VII	Bimorph Phase Shifter Configurations . . . . .	63
VIII	COAT Experiment Parameters . . . . .	79
IX	COAT System Calibration - Optical . . . . .	102
X	COAT System Calibration - Temporal . . . . .	102
XI	COAT System Calibration - Subsystems . . . . .	103
XII	Single-Glint Tests . . . . .	103
XIII	Static Multiple Glint Tests . . . . .	104
XIV	Moving Multiglint Tests . . . . .	104
XV	Beam Offset/Scan Tests . . . . .	105

## 1. INTRODUCTION

### A. Program Objectives

There are two primary objectives of this program. The first objective is to determine the performance limits of coherent optical adaptive techniques through operation of an experimental, visible prototype COAT system through a representative turbulent atmosphere against a complex dynamic target. The second objective is to determine the best methods of employing COAT in high power laser systems and to assess the status of necessary key high power components.

### B. Research Program Plan

The basic properties of the COAT concept have already been demonstrated by the simple experiments reported in Hughes Proposal, "COAT Planar Array", No. 73M-3186/C8902. However, to obtain the quantitative performance required by the present program, it is necessary to develop a new, fully-instrumented target system as well as review the previous system design concepts. The program plan adopted is shown in Fig. 1.

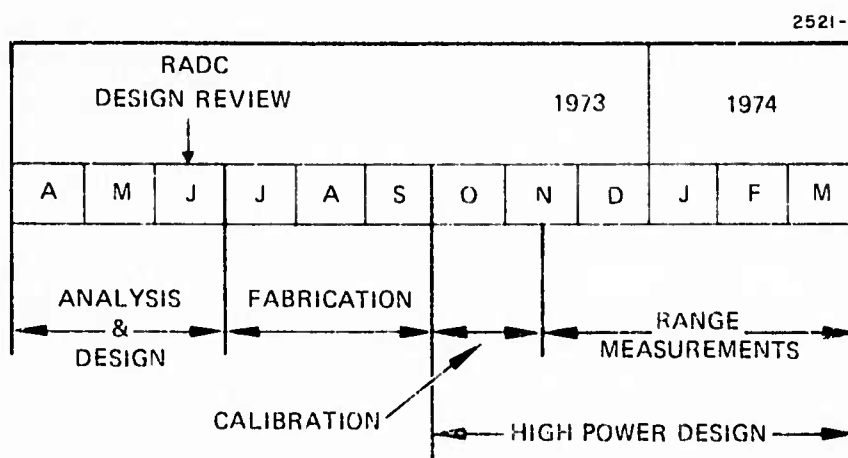


Fig. 1. COAT tasks and scheduling.

C. Organization of This Report

This first Technical Report covers the Analysis and Design tasks through the Design Review meeting held 20 June 1973 at Rome Air Development Center, Griffiss AFB, N.Y. Bound copies of the vugraphs presented at that meeting have already been supplied as line items A005 and A006, the Design Plan and Test Plan respectively. This report follows essentially the same order as that presentation.

In Section II the different analyses undertaken to answer critical questions about COAT system performance are presented; also the results obtained for convergence times using the seven-element linear array COAT system as an analog computer are described. The COAT system computer simulation developed during this quarter is described, and the results showing convergence on multiglint targets are presented. Other analyses on beam offset techniques, alignment errors, and array patterns are summarized.

In Section III the experimental COAT system design is reviewed, including the optomechanical layout and phaser matrix design, the phase shifter choices and the experiments that lead to these choices, and the electronic control system design. The layout of the optical propagation range is described, and the target design and data recording instrumentation are specified.

The laboratory calibration and on-range measurements program is discussed in Section IV. Plans for the next quarter are described in Section V.

## II. ANALYSIS

### A. Philosophy of Analytical Tasks

While the basic properties of multidither COAT systems were demonstrated by the three- and seven-element systems described in our proposal, there remained several unknown factors that needed further study before an improved system could be designed. Some of these factors were understood qualitatively but not quantitatively; for example, we knew that higher servo loop gain would cause the system to converge faster, but how much faster? The nonlinear and multiloop nature of the COAT control system does not lend itself readily to closed-form analysis; for this reason we have endeavored to arrive at quantitative answers primarily through computer simulation. The danger in traveling this route is that while we may well be able to create phenomena through simulation, we may not see the details clearly enough to really understand them; we may not be able to determine whether the phenomena are real or artifacts of the computation introduced by improper modeling of real-world physical properties. Partly for this reason, and partly for the value of the measurements themselves, we decided to continue to perform experiments on the three- and seven-element systems to guide and check the computer simulations, even though we are aware of the serious deficiencies in these experiments. The results of some of these experimental measurements are described in Part B.

We undertook the major task of developing a computer simulation for a COAT system, hopefully including all of the physical parameters that could conceivably affect the system performance. This development, described in Part C, has been successfully carried out to the point that all key system variables appear in the program, including the radiating element size, shape, and distribution within the array; the target glint number, intensities, distribution, and motion; and the control system modulation, filter, phase shifter, and AGC characteristics. The one key factor not yet included is the atmospheric turbulence in the propagation path;

only a simple phase-screen approximation is available at present. The simulation output allows us to examine the critical system performance measures: convergence time, convergence stability, and multiglint target discrimination.

In addition to the system dynamics simulation, supporting analyses have also been performed to address specific design choices: How can we best implement beam offset pointing? What will the alignment errors add up to in the optomechanical design? What are the best arrays to use during the experimental measurements program? Each of these analyses has been addressed in a manner suited to the particular problem.

#### B. Seven-Element System Experiments

At the outset of this contract the seven-element system had already served to point up system modifications that needed to be made. Some of these modifications were subsequently incorporated, and their performance was investigated. An AGC circuit was developed and shown to have the desired effect on system performance. Its design and characteristics are discussed in Section III-D. Resonances in the bimorph phase shifters, although lying outside the range of control and dither frequencies, were seen to limit the stable servo loop gain that could be employed in the system. As a result, improved phase shifter types were sought and found, although they have not yet been incorporated in the seven-element system; this work is described in Section III-C.

Attempts were also made to establish some of the important relationships, particularly the relations between open-loop gain and convergence time, and the relation between the control system parameters and the tracking limits for a moving target. These attempts have been only partially successful. The arrangement shown in Fig. 2 was used for these measurements. A high-speed mechanical shutter ( $\approx 1$  msec opening time) was placed in front of the COAT system detector to break the control loop. The system was otherwise operational, with the same parameters given in the proposal except for the addition of the AGC described in Section III-D. The glint, with its coincident point detector, was positioned

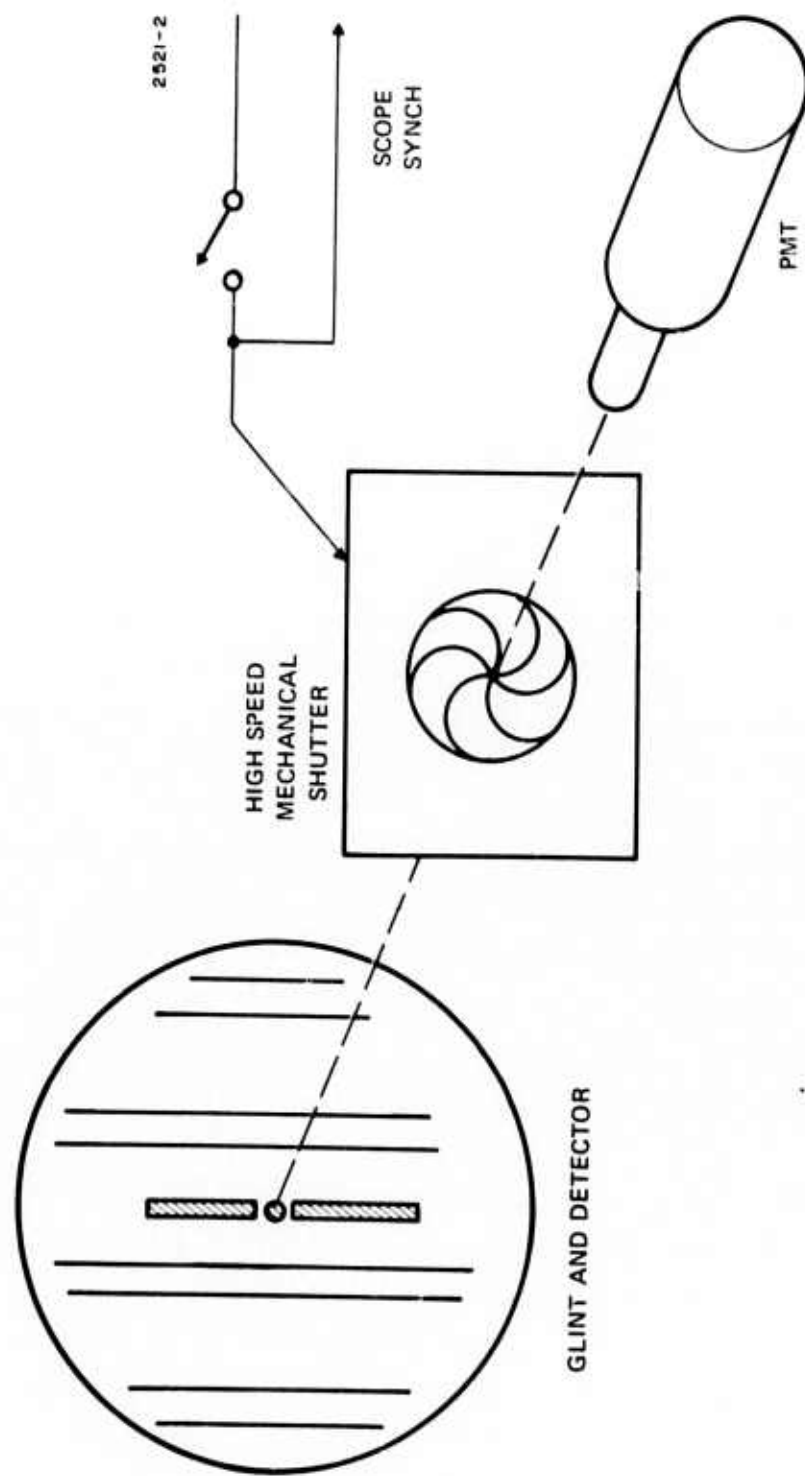


Fig. 2. Arrangement used to determine convergence time of the seven-element COAT system.

to a minimum of the random interference pattern incident on the target board. The shutter was then opened, and the build-up of both the power on the glint and the power returned to the photomultiplier were recorded. Figure 3 shows four different trials with the loop gain increasing from (a) through (d). Note that the convergence time decreases as the gain increases through (c) as expected, and that the ultimate converged power levels also increase (tighter convergence). The gain for trial (d) was high enough for the system to oscillate following an extremely rapid convergence.

It is evident from these results that the loop gain was indeed limited to low values. (Compare the results reported in Section III-D for the new electronics/phase shifter combination.) The convergence time for the curve marked "-27 dB (normal)" is about 5 msec, which is only about equal to the time constant of the 100 Hz low-pass filter employed. For high gain values, the convergence time should be much faster than the filter response time. Since we could not approach these gain values it was not possible to study the regime of interest for the new system design.

Figure 4 illustrates another important property of the COAT convergence process. The three photos were all taken with as nearly identical conditions as could be arranged. Before each shutter opening the glint was repositioned to a null in the random interference pattern. The convergence process is significantly different on the three trials. In (a) the convergence seems to take place completely in 1 msec or less, a time comparable to that of the mechanical shutter, and equal to only 2 cycles of the lowest dither frequency. Trial (b) is more typical, with a convergence time of approximately 5 msec. Trial (c) shows a step-wise convergence that occurs occasionally. This phenomenon has also been observed in the computer simulation and will be described in more detail in future reports. Note that the total convergence time is not much longer for the stepwise process, each step occurring rather fast.

This sequence of trials indicates that the details of the COAT convergence process depend rather critically on the initial state of the phase shifters and the initial phases of the dither signals. For favorable conditions the convergence can take place exceptionally fast, in a couple of dither cycles.

2521-42

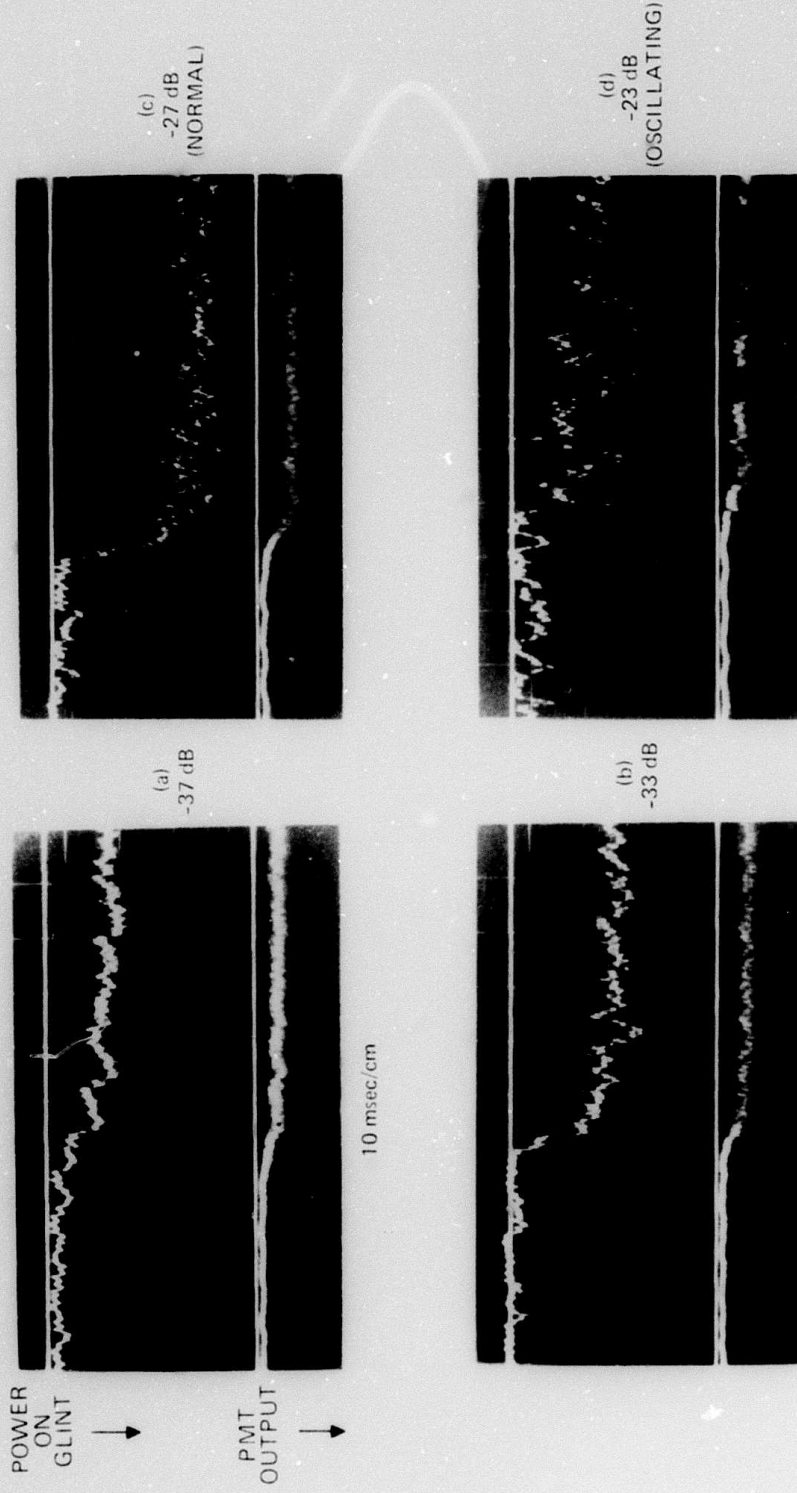


Fig. 3. Power on the glint (upper traces) and power returned to the COAT receiver (lower traces) as a function of loop gain. Loop gains shown indicate settings of an attenuator placed in the loop.

2521.43

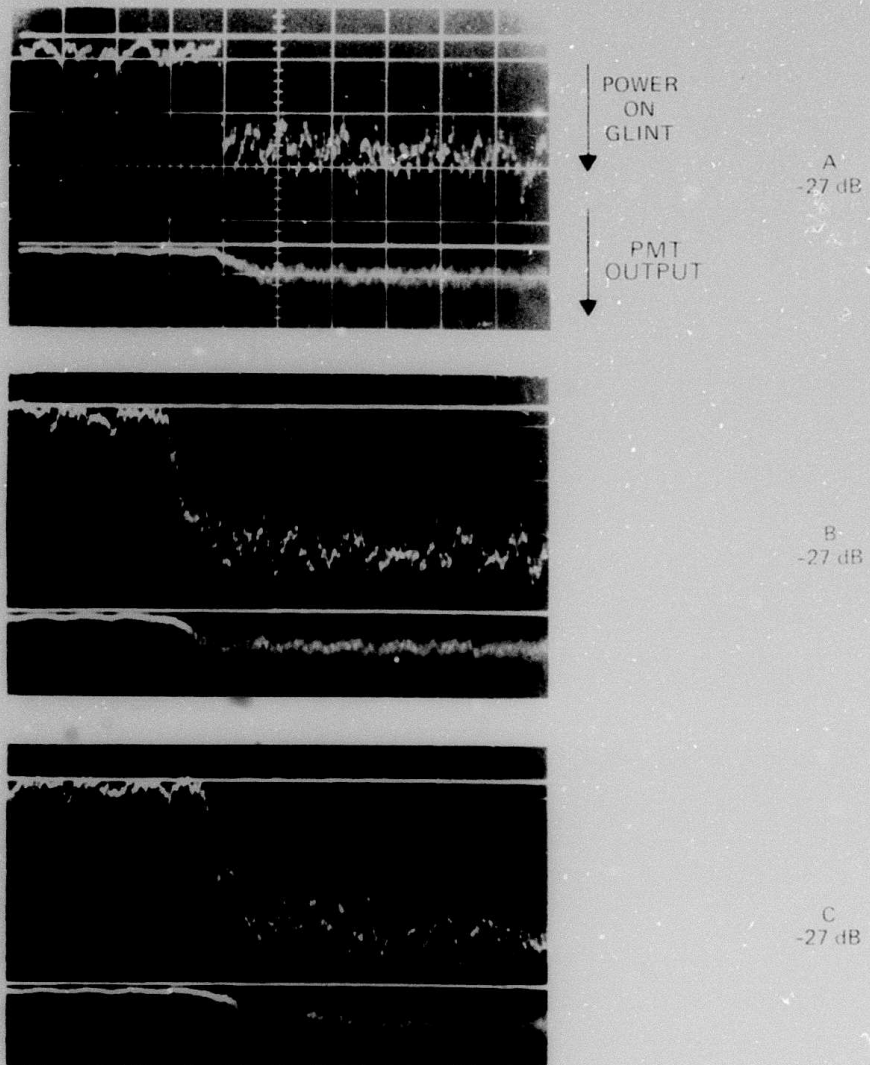


Fig. 4. Three measurements of the convergence process with nominally identical condition, showing the statistical nature of convergence process.

For unfavorable initial conditions, the convergence process may require very long times. It is apparent that "convergence time" is actually a random variable, having a certain distribution with a mean value, a characteristic width, etc. While this complicates the measurement of "convergence time", it in no way harms the practical aspects of the system. This description of random variation of convergence details has been confirmed by the computer runs, and we are now trying to catalog these and understand the details. The successful interplay of experiment and computer simulation in this instance verifies the wisdom of carrying on both approaches simultaneously.

Figure 5 shows a typical result from the moving target measurements. A glint and point detector were mounted on a parallelogram pendulum to provide sinusoidal motion over one grating lobe spacing at velocities higher than those previously used with the x-y recorder traverse (described in the proposal). The COAT system was disabled with the shutter in front of the photomultiplier as before. The left side of the photo (Fig. 5) shows the random interference pattern being intercepted by the moving detector. When the system is turned on by opening the shutter, it converges and tries to follow the glint. The sharp upward spikes on the right half of the photo show that the system is reconfiguring twice per round trip target motion. The reconfiguration in this case is another manifestation of the low loop gain. With low gain the error voltage can actually "go over the peak" in the sinusoidal synchronous detector transfer characteristic of output voltage versus input phase. The phase shifter can "slip" a number of wavelengths before it runs out of range or before the required relative phase conditions change. If the loop gain can be made sufficiently high, the error voltage for a given phase error is reduced by  $(1 + \text{Gain})^{-1}$ , and the control channel will always drive the phase shifter against its stop before any "slip" can occur. We could not reach that gain level in the seven-element system. This phenomenon was discussed in more detail in our earlier COAT report (Ref. 1) but observed for the first time in the seven-element system.

We plan to carry out computer simulation studies of both the convergence time statistics and the low-gain reconfiguration problem during the next quarter. The computer program being used for these studies is described in the following part of this report.

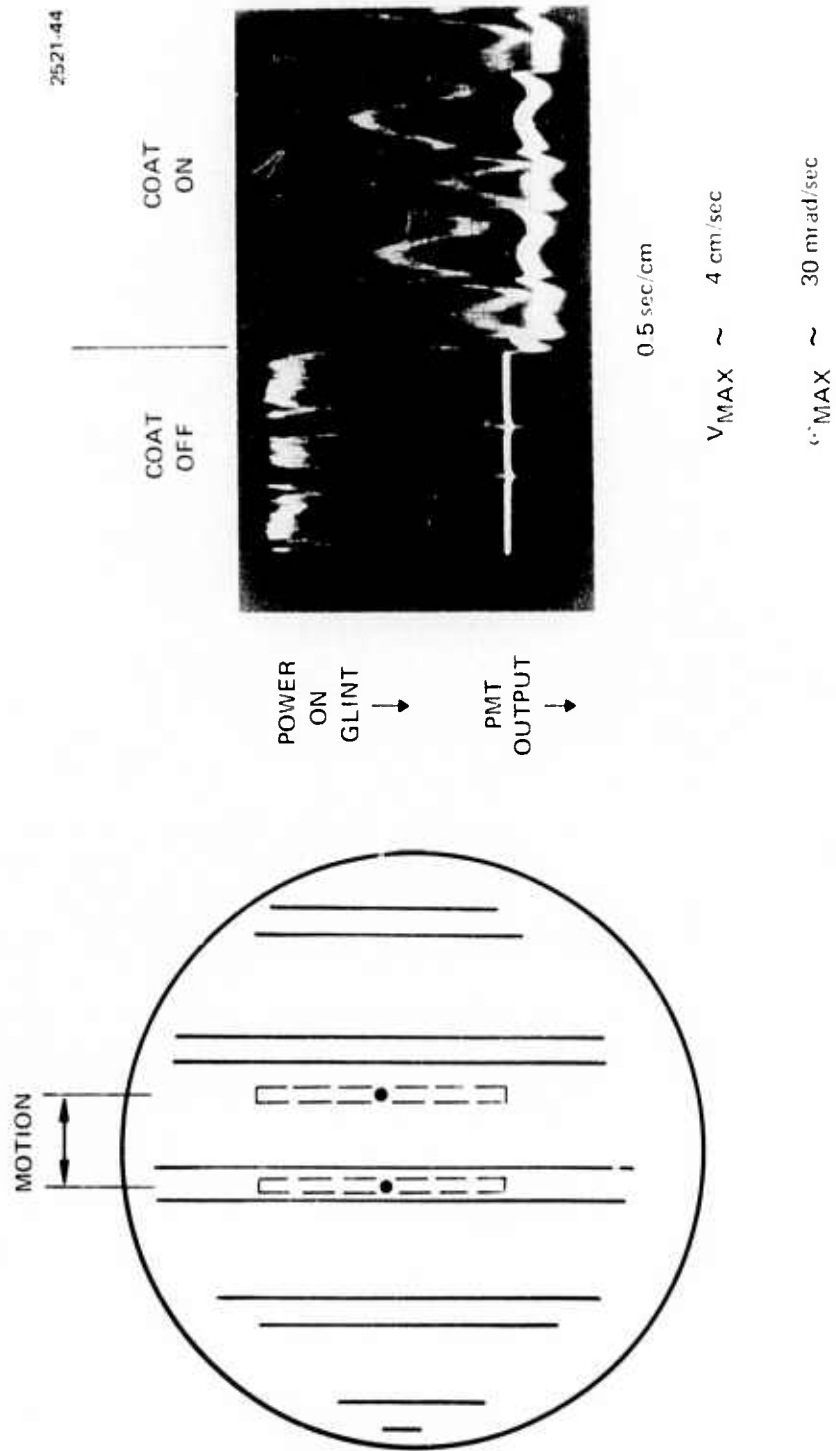


Fig. 5. Moving glint measurements. The drawing at left shows the extent of the sinusoidal target motion obtained with a parallelogram pendulum. Photo on right shows the power on the glint with the COAT system OFF and then ON as the target oscillates back and forth with a period of about 2 seconds.

### C. Computer Simulation

#### 1. Introduction

The COAT computer simulation was developed to aid in understanding the multidither convergence process and for use as a design tool. No assumptions were made to force convergence or to artificially enhance any particular system properties.

The functional flow chart used for the mathematical model is shown in Fig. 6. Briefly, the modeled system is as follows: Coherent light, divided into  $N_c$  channels, is phase modulated (dithered) and a correction phase is applied to each channel to form a specified array pattern. The radiation from this array is propagated over a specified path and is incident on the target plane. The summation of the reflections from  $N_G$  point targets is propagated back, collected in the receiver aperture, and photodetected. The ensemble signal is synchronously detected at each audio dither frequency to produce an ensemble of error voltages. These error voltages produce the channel correction voltages which are then used to adaptively phase the optical array to maximize power on the glint with the strongest weighted backscatter.

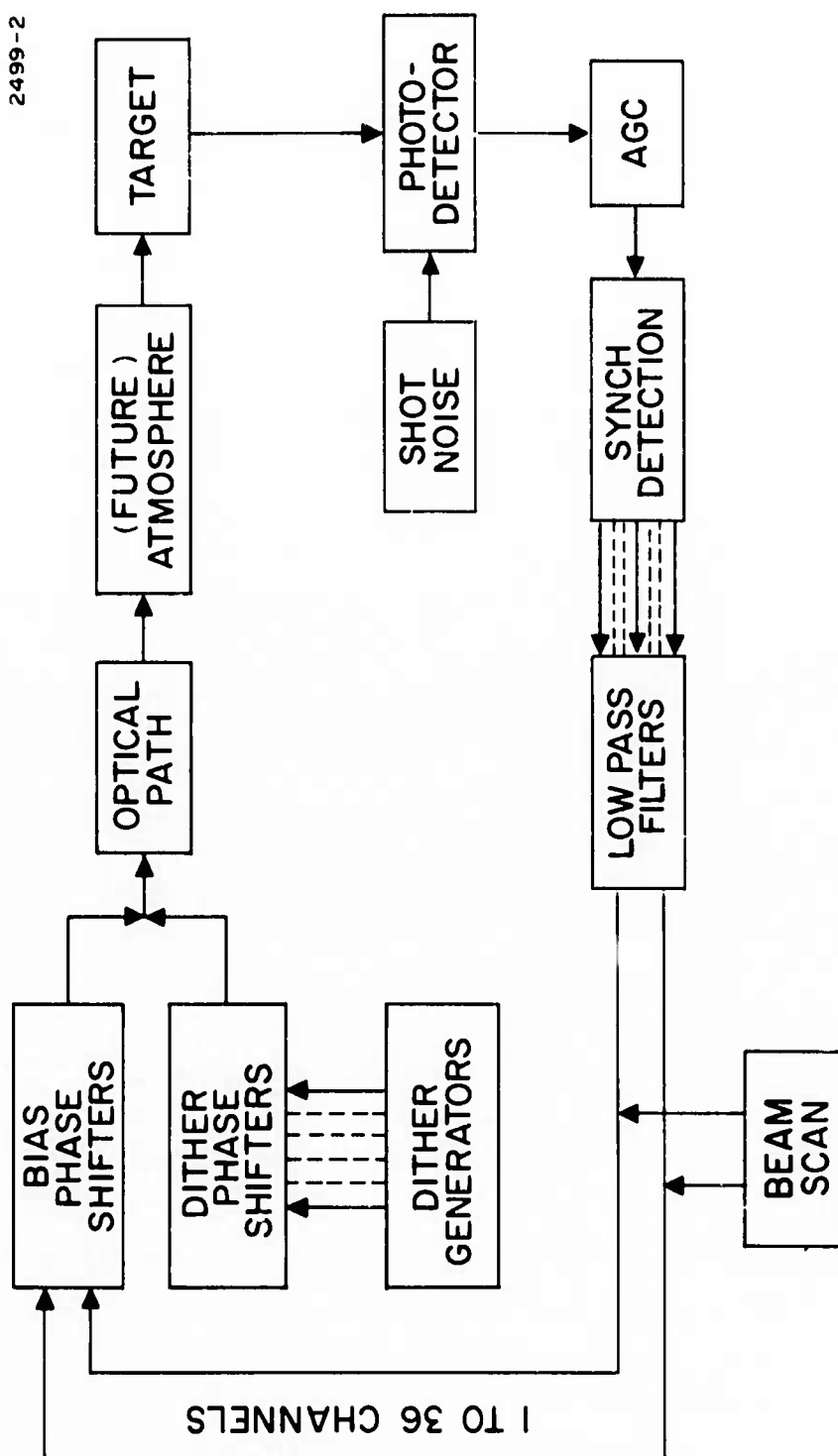
#### 2. Program Description

The mathematical model was implemented as a FORTAN IV, level G computer program for the Hughes IBM 370/165. It requires 118 K bytes of core memory after compilation, and uses one second of CPU time per transmit channel per millisecond of real time. A typical four msec test case with line plotter output for a  $4 \times 4$  array costs approximately \$10.

Figure 7 is the top level program block diagram. The main line subroutines are SHIFT, RANGE, DETECT, and FILTER. The MAIN program reads input data, sets up various counters for housekeeping tasks, sequentially calls the above subroutines, prints output data, and calls PLOTOM to format output data for line plotting. A peripheral subroutine, CLOOP, computes loop gain.

Test data is input in NAMELIST format; multiple test cases may be input in one run by tacking on NAMELIST cards which need contain only

Fig. 6. COAT functional flow chart for simulation.



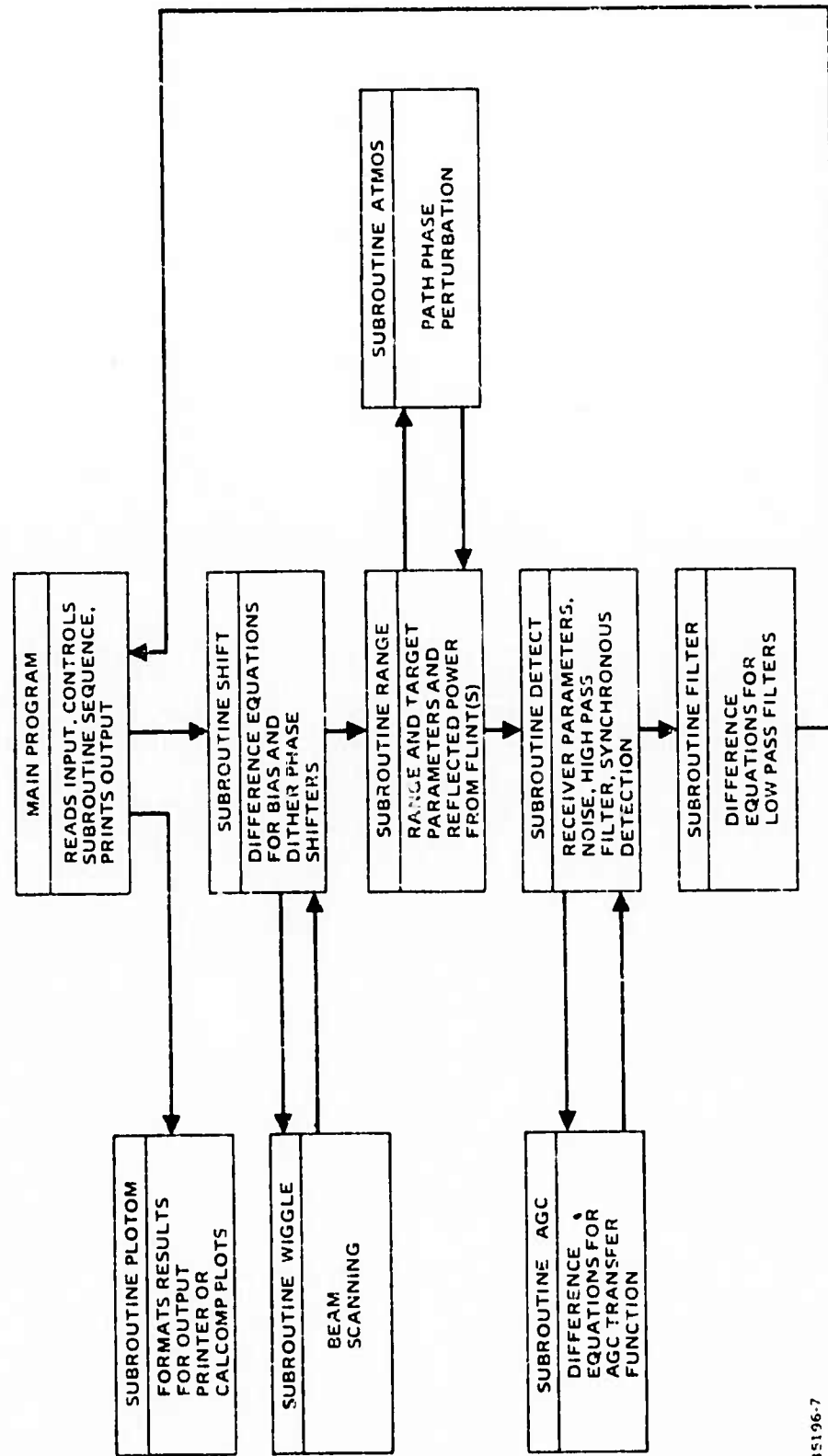


Fig. 7. Computer program block diagram for COAT simulation.

35196-7

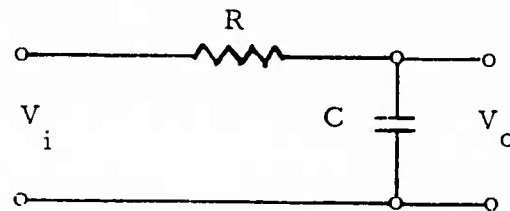
those parameters which change from test to test. Optical array phase may be initialized to any desired value; i.e., uniform, random, off-axis. The program computes initial conditions throughout based on this input. Form and substance of each subroutine will be discussed in the following.

a. SHIFT - The initial bias phase shifter voltages, low-pass filter output voltages, and dither phase shifter voltages are passed to SHIFT, which computes bias and dither phase shifter displacements at each time increment as a function of these voltages. The method used is to derive difference equations from a general form Laplace transform transfer function. The form of the transfer function is:

$$\frac{V_o(s)}{V_i(s)} = \frac{K \cdot (\tau_a s + 1)}{(\tau_b s^2 + \tau_c s + 1) (\tau_d s + 1)}$$

A separate set of difference equations is used for each bias and dither phase shifter.

A difference equation is a sampled data equivalent of the solution to a continuous differential equation describing phase shifter behavior. For example, a differential equation for the circuit:



$$v_i = RC \frac{dv_o}{dt} + v_o$$

may be written in Laplace transfer function form as:

$$\frac{V_o(s)}{V_i(s)} = \frac{1}{RCS + 1}$$

and in difference equation form as

$$V_o(t) = \exp\left(\frac{-T}{RC}\right) \cdot V_i(t - T) - \left[1 - \exp\left(\frac{-T}{RC}\right)\right] \cdot V_o(t - T)$$

In this case the output at any time  $t$  is equal to the difference of the weighted input and output at a time  $T$  seconds before.

In the program, any factor of the difference equation may be bypassed by setting the appropriate values to zero. Subroutine SHIFT also provides fixed or time dependent electronic beam scanning, and simulates the input for an open-loop incremental gain measurement when required.

b. RANGE — This subroutine computes the far-field amplitude power pattern, element-by-element, weights this pattern at the glint locations by their backscatter cross sections, and computes the optical power collected by the receive aperture. A simple subroutine (ATMOS) can be called to compute a deterministic time-variant phase perturbation for each element. This is not intended to represent a realistic atmosphere; however, it may eventually be replaced by suitable programs for turbulence or thermal blooming.

Other subroutines currently under development to be added to RANGE are MOVEIT, which will permit simulation of multiple moving targets; ARRAY, which will compute the dimensions of a 0-6-12-18 type circular array given the ID, OD, and number of rings; and SPLAT, which will compute and output a two dimensional printer map of the target plane power pattern at any point in time during a test run. These subroutines and preliminary results will be discussed in a later topic.

c. DETECT — Given received optical power as a function of time this subroutine models detection by a photomultiplier or photodetector, the difference being primarily the modeling of the detector noise behavior. Gaussian noise is added to the signal, and the result is high-pass filtered. The high-pass filter modeled in difference equation form is equivalent to the double pole filter implemented in hardware.

Following the filter, the ensemble signal is multiplied by each dither signal, appropriately phase shifted to account for round trip propagation

delay. The result is an unfiltered synchronously detected error signal for each channel, which is passed to subroutine FILTER.

DETECT also calls subroutine AGC, in which various automatic gain control schemes are modeled. The intent of these AGC schemes is to keep the mean level of the synchronous detector output at a constant value convenient for filtering.

d. FILTER - This subroutine computes difference equation outputs which model the low-pass filters used for smoothing and error signal separation. Each filter has the general form:

$$\frac{V_o(s)}{V_i(s)} = \frac{G_P \cdot (\tau_a s + 1)}{(\tau_b s + 1)(\tau_c s + 1)^M}$$
$$M = 1 \text{ or } 2$$

The filtered output for each channel is passed thru MAIN to subroutine SHIFT for the next time step.

e. GLOOP - This subroutine computes the incremental open loop gain (IOLG) for any state of the system. IOLG could be determined by fixing the state of the system during a simulation run, injecting a small bias phase shifter voltage, and propagating the change around the loop (refer to Fig. 6), to find the resultant change in the low pass filter output (error signal). This, in fact, is the experimental procedure for determining IOLG in the laboratory COAT models. The IOLG is thus defined for the  $k^{\text{th}}$  channel as

$$\text{IOLG} = 20 \log \left| \frac{\Delta V_{fk}}{\Delta V_{Bk}} \right|$$

where the units are dB and  $\Delta V_{fk}$  is the change in the low-pass filter voltage produced by  $\Delta V_{Bk}$ , the change in bias phase-shifter voltage. Note that IOLG is a time-dependent quantity which is affected by all the system parameters including receiver filter characteristics and electronic gain, propagation, target characteristics (number and strength of glints), and degree

of convergence. For computational purposes, however, it is more efficient to derive an analytical expression for the open loop gain. Such a derivation is presented in Appendix I. The procedure presently used in the computer program to compute IOLG is a special approximation of the more general result discussed in Appendix I. The use of the approximation, however, has no effect on the results described in this report. The more general result will be incorporated into the computer routine at an appropriate future date.

Figure 8 illustrates the relationship between the various quantities used in determining IOLG for a simple two-element system. The phase  $\beta_1$  or  $\beta_2$  is the total phase from the elements to the glint. Note that the open loop signal is related to the derivative of the intensity on the glint and thus minimizes at convergence. The IOLG is related to the derivative of the error signal and so maximizes at convergence.

Results of the program calculation of IOLG have been compared with measurements on the GSG laboratory 2-element model and with calculations which used the in-line simulation program to find IOLG. Agreement among all three methods was obtained within 3 dB. We do not, however, fully understand the relationship between IOLG in a particular channel and the details of the convergence process. Further study on this subject is planned for the next quarter.

### 3. Program Options and Variables

All test case options are chosen by appropriate variable selection in the program input data. Only those portions of the program required for a particular test case are actually used during that run. A textual description of the options selected with appropriate data values is printed out at the beginning of each test case.

The important program variables are those which relate directly to an adjustable system hardware parameter. Consequently, the following parameters can be varied at the input to the program:

- a. Variable number of channels (up to 36) and glints (up to 10).
- b. Single frequency per channel or quadrature operation with one frequency per two channels.

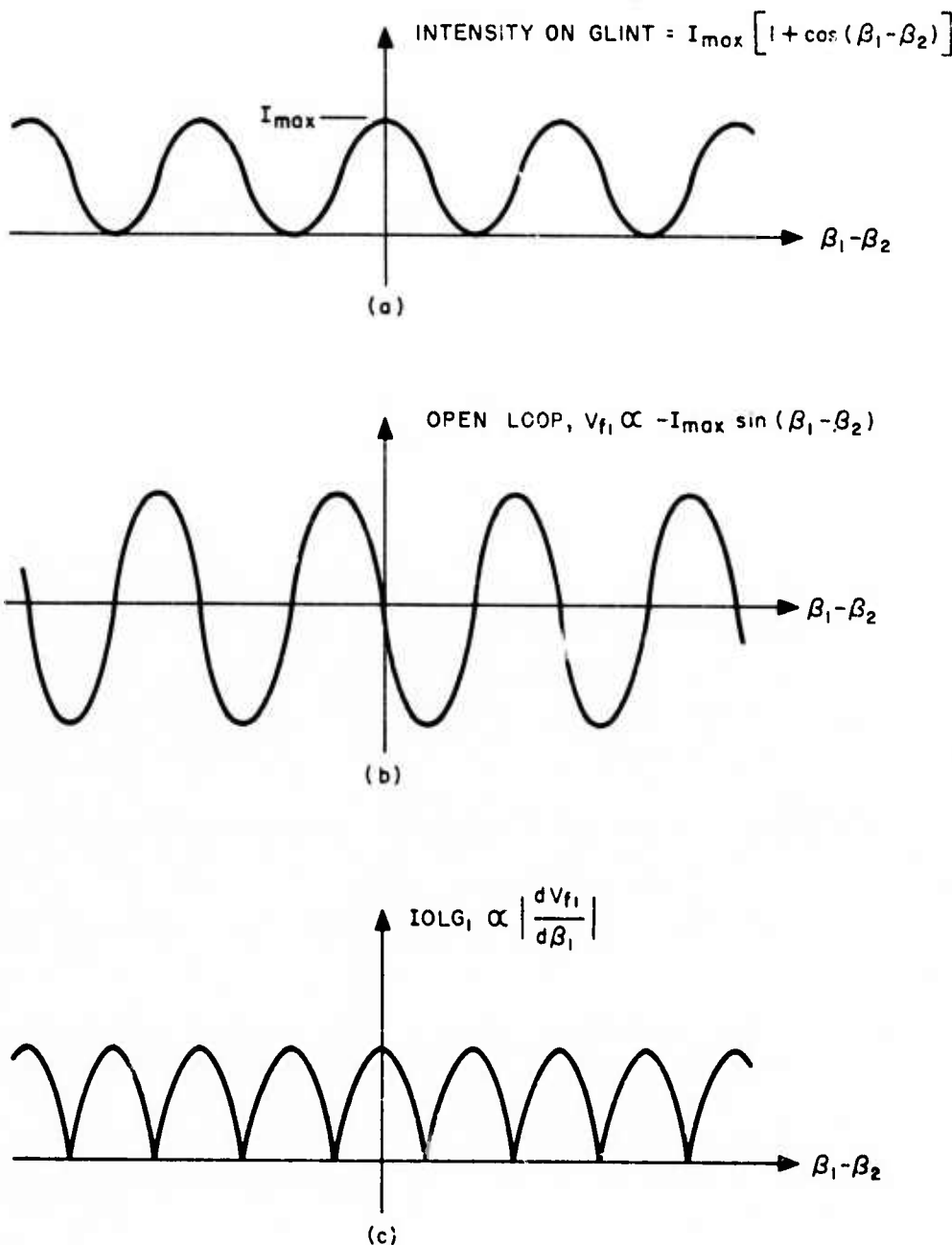


Fig. 8. Two element COAT quantities as a function of the total phase difference between channels.

- c. Single or split phase shifters per channel; in the former case control and dither voltages are added before application to the phase shifter.
- d. Bias phase shifter constant (volts/meter).
- e. Dither peak voltages and frequencies and dither phase shifter constant (volts/meter).
- f. Beam steering at fixed or time variant steering angles.
- g. Array configuration, element size, shape, and placement.
- h. Range to the target.
- i. Glint backscatter cross sections and locations.
- j. Receiver aperture.
- k. Photodetector gain constant (GFODET).
- l. Shot noise or noise free operation.
- m. Pre-detection gain (GHIP) and post-detection gain (GPASS).
- n. Square wave or sine wave synchronous detector reference.
- o. All filter time constants.
- p. Soft shoulder limiter threshold voltage.
- q. Feedforward or feedback AGC.
- r. Output in printed form, printer plot, or continuous line plot.

CURRENTLY BEING ADDED

- s. Rectilinear or circular array.
- t. Arbitrarily specified motion for each glint target.
- u. Target plane two-dimensional power density map.

In most of the tests to date, all variables except GFODET, GHIP, GPASS, have been set to values which were consistent with the design for the 18-element system now under construction. For simplicity, GHIP and GPASS were set to unify so that GFODET, the photodetector voltage gain, is the only

variable electronic gain. The AGC option in the program was not used for all of the simulation runs discussed in this report.

#### 4. Simulation Verification

A series of comparison tests were run on the simulation and on a two-element version of the GSG three-element system. System constants measured in the laboratory (e.g., electronic gain) were employed in the simulation whenever possible. The results shown in Table I indicate good agreement between the simulation and the hardware. The simulation incremental loop gain was computed from the derived equation discussed in a previous topic and in Appendix I.

TABLE I  
Hardware/Simulation Comparison

	Convergence Time (msec)	Control Voltage Overshoot (%)	Converged Incremental Loop Gain (dB)
Hardware Experiment	1.2	40.0	15.4
Computer Simulation	1.2	37.0	12.8

The simulation results also proved intuitively satisfying. Figure 9 is typical of the plots obtained during these tests. The glint power density curve is inked in heavily. Note that the power variation due to dither of one channel at a 4 kHz rate shows frequency doubling near the center of the plot as the array beam is dithered about the point of maximum convergence on the glint. The glint power density also peaks at the theoretical maximum in this area.

The run shown in Fig. 9 also shows the phenomenon of "dither feed-through." Initially, the 2-element array is almost fully converged on the glint, but the low-pass and high-pass filters\* are not fully charged. The

---

\*The high pass filter follows the photodetector to remove any dc component in the signal.

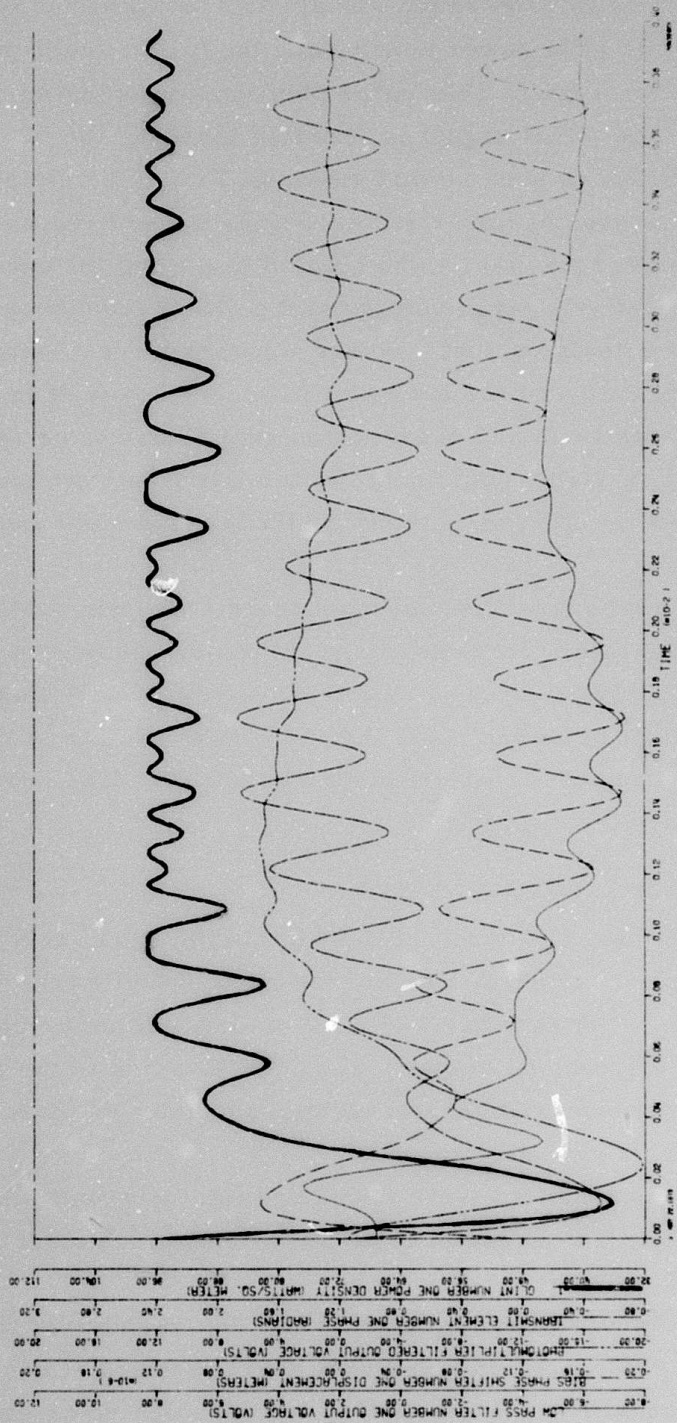


Fig. 9. Typical computer output showing power on the glint (heavy curve), low-pass filter output, phase shifter displacement, photomultiplier output, and element phase (see legend at left for curve identification.)

time required for the filters to reach steady state is the cause of both the initial decrease in the glint power density and the higher frequency content of the low-pass filter output. This latter phenomenon is known as "dither feedthrough" since the dither signal is "feeding through" the low-pass filter.

Dither feedthrough such as that shown in Fig. 9 is related to the filter transient response characteristics. First, an uncharged high-pass filter will allow some dc voltage to be applied to the synchronous detector. This results in a relatively large voltage at the dither frequency appearing at the synchronous detector output. If this signal is large enough, some of it will appear at the output of the low-pass filter. The result is a dither signal of unknown amplitude and phase which gets added to the applied dither signal and which appreciably contributes to the initial system transients. The effects of dither feedthrough are currently being studied under the IR&D program at HRL.

At the present time, all equations and their implementation in the simulation are being reviewed by an analyst who was not involved in their initial development. The purpose of this review is to insure that all underlying assumptions are reasonable and that no errors remain in the program code. At this point only a few small errors have been found, none of which affect the results obtained to date.

### 5. Initial Simulation Results

The results of these initial simulation runs should be viewed as very preliminary; no general conclusions about COAT systems should be inferred from them. These runs were used to effect further improvements in the simulation program, to improve our understanding of the simulation, and to lay the foundations for future simulations which will more exactly model experimental situations.

Two sets of parameters were developed for the initial single- and multi-glint analyses. The array configurations and parameters are shown in Tables II and III.

The first step was to run a baseline test for each array to determine optimum values of photodetector gain. The test consisted of two single-glint run sequences, each with eight test cases, with photodetector gain (GFODET) as the only variational parameter. The single glint was located one-half

TABLE II

1 x 9 Array Configuration

2521-3

1	2	3	4	5	6	7	8	9
---	---	---	---	---	---	---	---	---

Fixed Parameters	Variational Parameters
Element Size: $0.555 \times 10^{-3} \times 0.555 \times 10^{-3}$ M	Number of glints
Element (peak-null) beamwidth $8.78 \times 10^{-5}$ rad	Glint location
Array (peak-null) beamwidth $0.976 \times 10^{-5}$ rad	Glint backscatter cross section
Wavelength: $0.488 \times 10^{-6}$ M	Electronic gain (GFODET)
Range to target: 100 M	Dither amplitude
High pass filter cutoff: 400 Hz	Dither frequencies
Low pass filter cutoff: 160 Hz	
Bias Phase Shifter Transfer Function	
Noise Suppressed	
Maximum Power Density on Optical Axis $1.2 \times 10^5$ Watts/M <sup>2</sup>	
Pre-detection Gain: Unity	
Post-detection Gain: Unity	

TABLE III  
4 x 4 Array Configuration

2521-5

1	2	3	4
---			
		---	16

Fixed Parameters	Variational Parameters
Element Size: $1.25 \times 10^{-2} \times 1.25 \times 10^{-5}$ M	Number of glints
Element (peak-null) Beamwidth $3.9 \times 10^{-5}$ rad	Glint location
Array (peak-null) Beamwidth $0.976 \times 10^{-5}$ rad	Glint backscatter cross section
Wavelength: $0.488 \times 10^{-6}$ M	Electronic Gain (GFODET)
Range to Target: 100 M	Dither amplitude
High Pass Filter Cutoff: 400 Hz	Dither frequencies
Low Pass Filter Cutoff: 160 Hz	
Bias Phase Shifter Transfer Function	
Noise Suppressed	
Maximum Power Density on Optical Axis $1.1 \times 10^6$ Watts/M <sup>2</sup>	
Pre-detection Gain: Unity	
Post-detection Gain: Unity	

array beamwidth from the optical axis. From the eight test cases, two values of photodetector gain were selected for each array. These values and the resulting calculated values of initial incremental open loop gain (IOLG) are shown in Table IV.

TABLE IV

Gain Values for Initial Simulation Runs

Array	4 x 4		1 x 9	
GFODET	1000	2000	5000	15000
IOLG(initial)	11.99	16.54	5.27	14.04

Several test runs were then made to study the convergence process of both arrays in a multi-glint environment and to answer some specific questions about the effects of modulation index and dither separation on convergence. Results of these tests are discussed in the next topic.

#### 6. Analysis of Multi-Glint Convergence

As a primary analysis task the computer program was used to study the COAT system behavior in a multi-glint environment, with the result that the COAT simulation did maximize on the largest resolvable glint as expected and as observed experimentally. As a secondary task, the simulation also provided data on the effects of modulation index and dither frequency separation.

The glint configurations used are far from a complete set, but were chosen for ease of understanding the resulting data. Other configurations will be investigated in the future that reflect more closely the range of situations expected during experimental operation. The results obtained in these preliminary calculations for three specific areas are summarized in the following text:

- Selectivity and energy build-up rates on a single glint in a multiple glint environment.
- Effects of modulation index on peak power and convergence time.

- Effects of closely spaced dither frequencies.

a. Multi-glint Environment — The output of the simulation for this analysis consisted of line plots of the power on each glint as a function of time. Three specific quantities were analyzed on each plot and compared: (1) glint power buildup rates, (2) convergence time, and (3) the final average power on the glints. Figure 10 illustrates a typical output format and shows the straight line approximations used in defining these quantities.

Both the  $1 \times 9$  linear and  $4 \times 4$  planar arrays of Tables II and III were investigated for various glint arrangements in a two-glint and modified two-glint environment.

Figure 11 indicates the glint arrangements with respect to the initial element and array patterns. The relative glint reflectivities are indicated as a cross-section in Tables V and VI. These numbers correspond to the squared magnitude of the amplitude reflectivities discussed in Appendix I. For each run the array was initialized to form a boresight maximum; convergence of the array pattern on a glint then occurred as discussed below. The final converged conditions are not shown in the figure, but are indicated by the "Final Power" column in Tables V and VI.

All gains in the simulation were set to 1 with the exception of the photodetector gain which was changed between runs. All dither spacings were fixed at 1 KHz except in runs 4-7, 4-8, and 4-9 where "random" spacings of greater than 1 KHz were used.

Tables V and VI summarize the results for the  $1 \times 9$  and  $4 \times 4$  arrays, respectively (see Tables II and III for the array parameters in each case). When no convergence occurred on a particular glint, no convergence time is shown in the tables and the buildup rate is shown as zero. The final power on each glint is shown for comparison purposes.

For the  $1 \times 9$  array, tests 9-1, 9-2, 9-5, and 9-6 show that convergence occurs on the stronger of two resolvable glints and that higher gain (runs 9-5 and 9-6) gives a shorter convergence time. Run 9-3 shows convergence on the centroid of 2 unresolvable glints as expected. Note that this type of convergence puts most of the power, but not the beam maximum, on the stronger glint. Runs 9-4 and 9-8 with equal unresolvable

2521-6R1

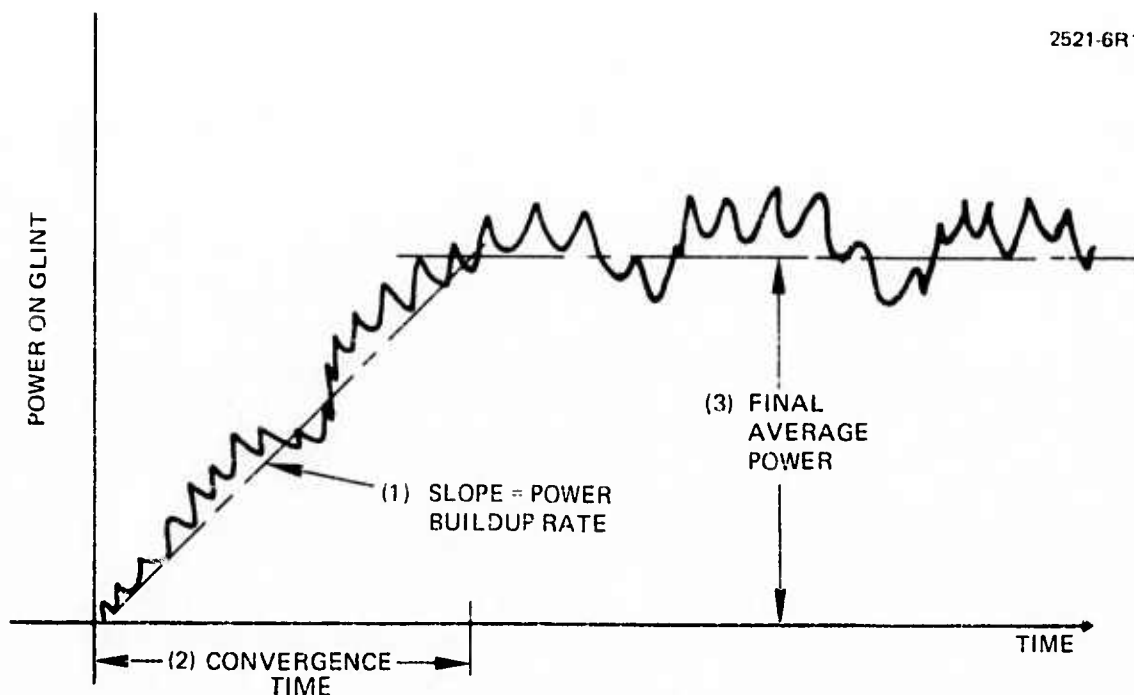


Fig. 10. Definitions of quantities used in analyzing computer runs.

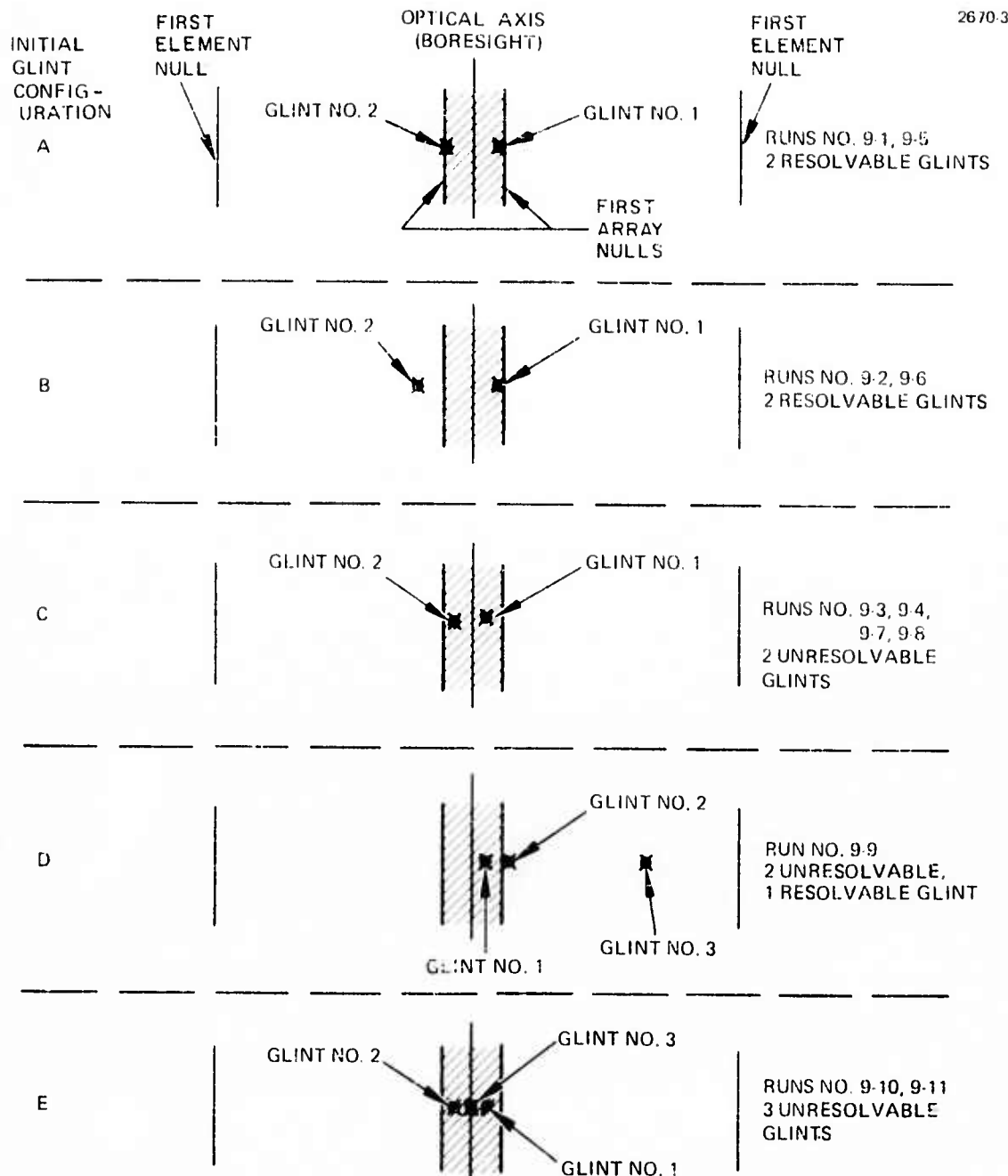


Fig. 11(a).  
 Glint configurations for 1x9 linear array with respect to initial array and element 3-dB intensity contours. The array pattern is one-dimensional with a beam width (shaded) equal to 1/9 of the element beam width. The array maximum is initially converged on the transmitter boresight and moves from that condition.

2670·4

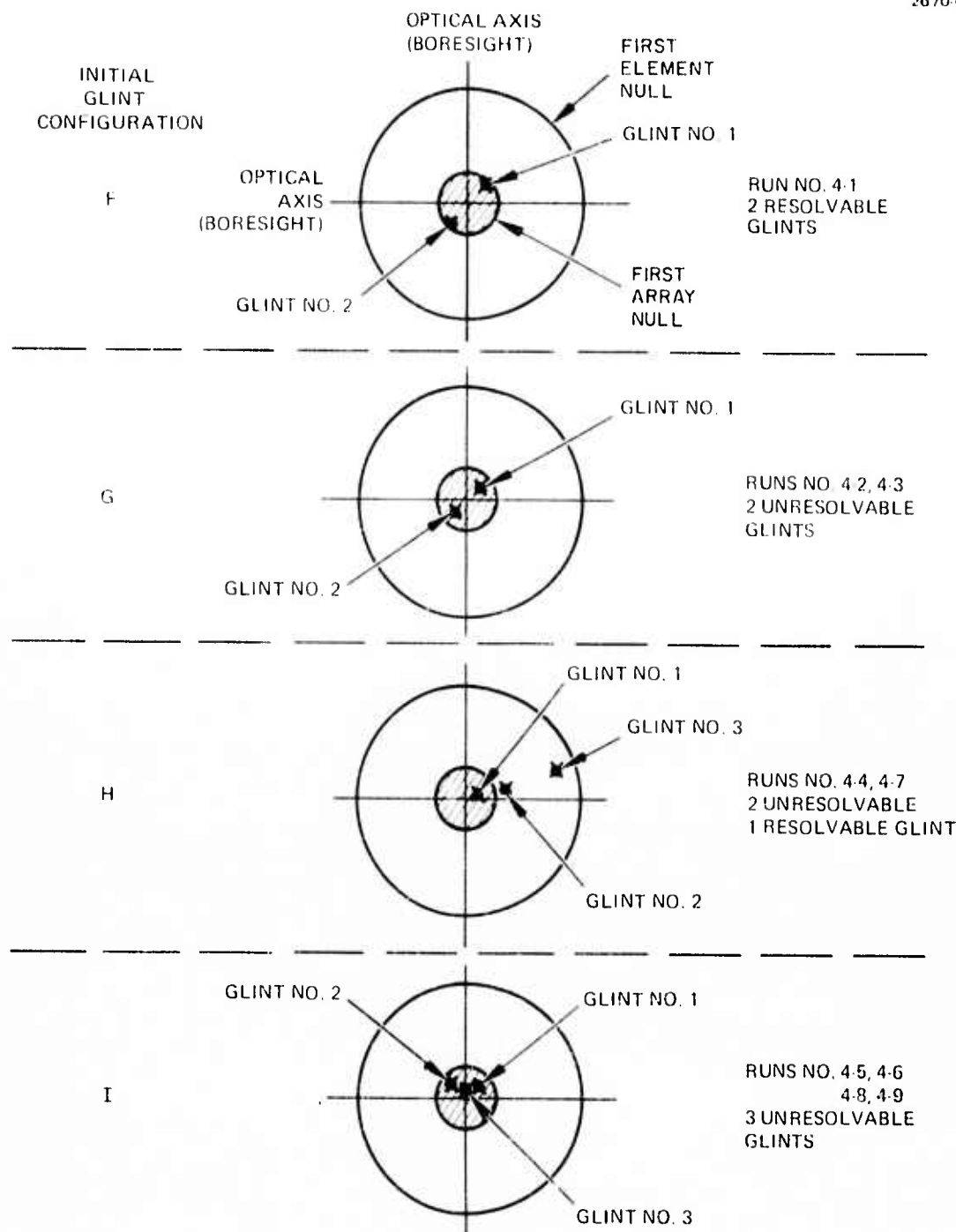


Fig. 11(b).

Glint configurations for 4x4 planar array with respect to initial array and element 3-dB intensity contours. The array pattern is two-dimensional with a beam width (shaded) equal to  $1/4$  of the element beam width. The array maximum is initially converged on the transmitter boresight and moves from that condition.

TABLE V

**Summary of 1 x 9 Linear Array Data For  
A Two Glint and Modified Two Glint Configuration  
Maximum boresight intensity =  $12 \times 10^4$  W/M<sup>2</sup>**

Simulation Number	Detector Gain (GFODET)	GLINT No. 1			GLINT No. 2			GLINT No. 3			See Note	Simulation Glint Configuration (see Fig. 11a)
		Cross Section M <sup>2</sup>	Final Power, W/M <sup>2</sup>	Buildup Rate, sec	Cross Section M <sup>2</sup>	Final Power, W/M <sup>2</sup>	Buildup Rate, sec	Cross Section M <sup>2</sup>	Final Power, W/M <sup>2</sup>	Buildup Rate, sec		
9-1	5000	10	$0.2 \times 10^4$	0	--	31.6	$8 \times 10^4$	$2.5 \times 10^7$	3.2	0	--	--
9-2	5000	10	$1.6 \times 10^4$	0	--	31.6	$10 \times 10^4$	$3.57 \times 10^7$	2.8	0	--	--
9-3	5000	10	$4 \times 10^4$	0	--	31.6	$10 \times 10^4$	$5.5 \times 10^7$	1.8	0	--	--
9-4	5000	10	$7 \times 10^4$	0	0	10	$7 \times 10^4$	0	0	0	--	--
9-5	15000	10	$0.2 \times 10^4$	0	--	31.6	$8 \times 10^4$	$4 \times 10^7$	2	0	--	--
9-6	15000	10	$1.5 \times 10^4$	0	--	31.6	$9 \times 10^4$	$5.6 \times 10^7$	1.6	0	--	--
9-7	15000	10	$7 \times 10^4$	0	--	31.6	$8 \times 10^4$	0	--	0	--	--
9-8	15000	10	$7 \times 10^4$	0	0	31.6	$7 \times 10^4$	0	0	0	--	--
9-9	5000	10	$8 \times 10^4$	$6 \times 10^7$	0.9	31.6	$6 \times 10^4$	$6 \times 10^7$	0.9	100	$0.6 \times 10^4$	0
9-10	5000	10	$6 \times 10^4$	0	--	31.6	$5 \times 10^4$	0	--	100	$1.0 \times 10^4$	$3.33 \times 10^7$
9-11	5000	10	$7.5 \times 10^4$	0	0	10	$6.5 \times 10^4$	0	0	10	$1.2 \times 10^4$	0

Notes: 1. Equal, symmetrically placed, unresolvable glints. No change in beam formation; initial condition is fully converged.

2. No stable convergence due to instability caused by high gain. Final power is power on glints at the end of the run.

3. Convergence on the centroid of two unresolvable glints.

TABLE VI

**Summary of 4 × 4 Planar Array Data For  
A Two Glint And Modified Two Glint Configuration  
Maximum boresight intensity =  $11 \times 10^5 \text{ W/M}^2$**

Simulation Number	Detector Gain (GF ODET)	GLINT No. 1			GLINT No. 2			GLINT No. 3			Conv. Time, m/sec	Buildup Rate w/M <sup>2</sup> /sec	Buildup Rate w/M <sup>2</sup> /sec	Conv. Time, m/sec	Glint Configuration (see Fig. IIb)	See Note
		Cross Section M <sup>2</sup>	Final Power, W/M <sup>2</sup> -sec	Conv. Time, nsec	Cross Section M <sup>2</sup>	Final Power, W/M <sup>2</sup>	Conv. Time, msec	Cross Section M <sup>2</sup>	Final Power, W/M <sup>2</sup>	Conv. Time, msec						
4-1	1000	10	$0.4 \times 10^5$	0	--	$31.6 \times 10^5$	$9.5 \times 10^5$	$3.65 \times 10^8$	2.6	0	--	--	--	--	--	F
4-2	1000	10	$4 \times 10^5$	0	--	$31.6 \times 10^5$	$10 \times 10^5$	$6.25 \times 10^8$	1.6	0	--	--	--	--	--	G
4-3	1000	10	$6.2 \times 10^5$	0	0	$10 \times 10^5$	$0.2 \times 10^5$	0	0	0	--	--	--	--	--	H
4-4	1000	10	$6.5 \times 10^5$	$4 \times 10^8$	1.6	$31.6 \times 10^5$	$6.5 \times 10^5$	$4 \times 10^8$	1.6	100	$0.06 \times 10^5$	0	--	--	--	P
4-5	1000	10	$0.5 \times 10^5$	0	--	$31.6 \times 10^5$	$2 \times 10^5$	0	--	100	$2.4 \times 10^5$	0	--	--	--	I
4-6	1000	10	$6 \times 10^5$	0	--	$10 \times 10^5$	$5.5 \times 10^5$	0	--	10	$11 \times 10^5$	$3.6 \times 10^8$	3	3 unres.	I	2
4-7	1000	10	$4 \times 10^5$	$2 \times 10^8$	3.0	$31.6 \times 10^5$	$6.5 \times 10^5$	$2 \times 10^8$	3.0	100	$0.06 \times 10^5$	0	--	--	--	I
4-8	1000	10	$1.5 \times 10^5$	0	--	$31.6 \times 10^5$	$1.3 \times 10^5$	0	--	100	$2 \times 10^5$	0	--	--	--	H
4-9	1000	10	$7 \times 10^5$	0	--	$10 \times 10^5$	$5 \times 10^5$	0	--	10	$11 \times 10^5$	$5 \times 10^8$	2.2	3 unres.	I	2

\* "Random" dither spacings; see text

Notes:

1. Equal, symmetrically placed, unresolvable glints. No change in beam formation; initial condition is fully converged.
2. No stable convergence due to instability caused by high gain. Final power is power on glints at the end of the run.
3. Convergence on the centroid of two unresolvable glints.

glints placed symmetrically about the boresight axis showed no change in the convergence state from the start to the finish of the runs. This means that the initial condition (convergence on the glint centroid) is the same as the best converged condition. Test 9-7 exhibited no stable convergence due to the onset of instability at the higher loop gain.\*

Runs 9-9, 9-10, and 9-11 are similar to other runs with this array, but another unresolved glint is added to the target. Run 9-9 demonstrated convergence at the centroid of glints 1 and 2, ignoring the largest glint at the edge of the element pattern. Tests 9-10 and 9-11 indicated convergence on the centroid of three unresolvable glints although in run 9-11 the initial and final convergence states are identical.

The tests on the 4 x 4 planar array are summarized in Table VI. The conclusions are the same as for the 1 x 9 linear array: (1) convergence on the larger of 2 resolvable glints (run 4-1); (2) convergence on the centroid of multiple unresolvable glints with the most power on the largest glint (runs 4-2, 4-3, 4-5, 4-6); (3) convergence on the centroid of two unresolvable glints when a larger, resolvable glint is at the edge of the element pattern (run 4-4); and (4) instability due to excessive gain (run 4-6).

The last three entries in Table VI are identical to runs 4-4 to 4-6 but with random dither frequency spacings of greater than 1 KHz. The results are comparable to the runs with equally-spaced dither frequencies. Although there is a large difference in convergence times between runs 4-4 and 4-7, the variation is primarily due to difficulty in interpreting the stepwise convergence which was observed in these runs. This type of convergence has also been observed experimentally (see Fig. 4) and will be described in more detail in future reports.

As a general assessment of these initial runs, we may say that the COAT simulation is operating correctly. However, the simulation run times were initially limited to 4 msec to minimize costs. In the

---

\*The net loop gain is a function of the strength (cross-section as well as the number and location of all the glints).

future, run times will be extended to the order of 10 msec to ascertain whether or not the system reached a true steady state. Contour plots of the final power distribution at the target will also be printed out; these should be extremely helpful in determining the system performance. As an example, a contour plot derived in a post-run program from the final phase shifter settings was made from run 4-4. The data in Table VI suggests that the system had maximized on the centroid of glints 1 and 2. The conclusion seems reasonable since glint 3 is near the edge of the element pattern and glints 1 and 2 are near the boresight axis and within a beamwidth spacing (not resolvable). The final power contour is shown in Fig. 12 and it does, indeed, confirm this conclusion.

6. Modulation Index — It is desirable to operate the COAT system with a minimum modulation index in order to maximize the ultimate power on the glint. On the other hand, the greater the modulation index the faster the system converges because an increasing modulation index permits a higher loop gain for a given noise level. Hence, there is a trade-off in modulation index between maximum power on the glint and quick convergence. A series of runs were made to investigate these effects and to select an optimum modulation index for a given set of system conditions.

The set of system parameters chosen were: a  $1 \times 9$  linear array, photodetector gain of 5000, no external system noise, and a single glint target located half way between the optical axis and first antenna null. The modulation angle was varied from  $\pm 10$  to  $\pm 120$  degrees in steps of  $\pm 10$  degrees; each step required a separate computer run. The results are plotted in Fig. 13 and 14.

Figure 13 shows glint power as a function of modulation index. For low modulation indices and no external system noise, the system should approach full power on target; however, noise is introduced by computer roundoff error, and hence the power appears to decrease below 20 degrees as shown. As indicated in the figure, this particular system should operate between 20 to 30 degrees to ensure maximum glint power. Even though this apparent optimum is a computer artifact, when real noise is introduced a similar

0-2521-36

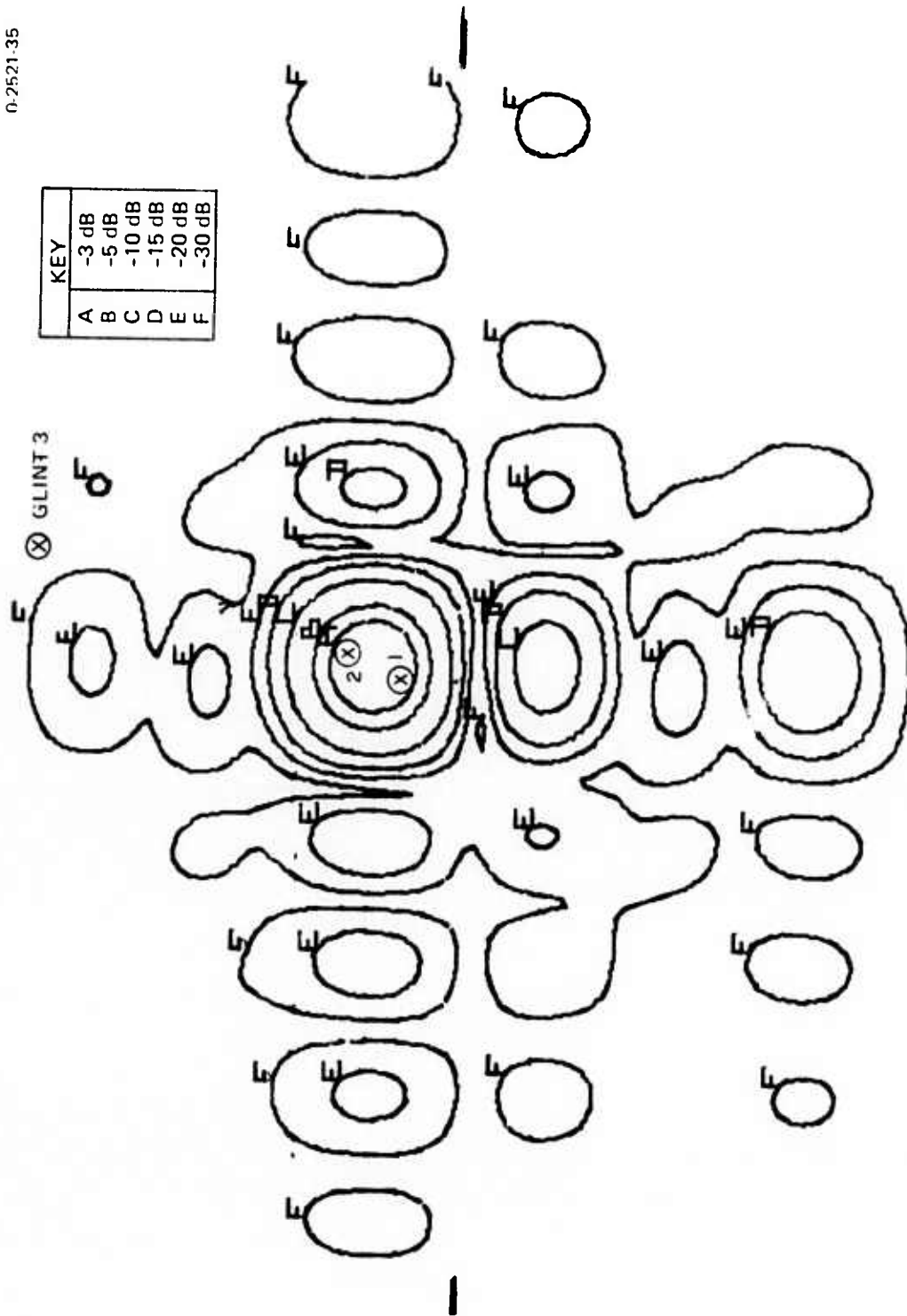


Fig. 12. Final target plane power distribution for Run 4-4.

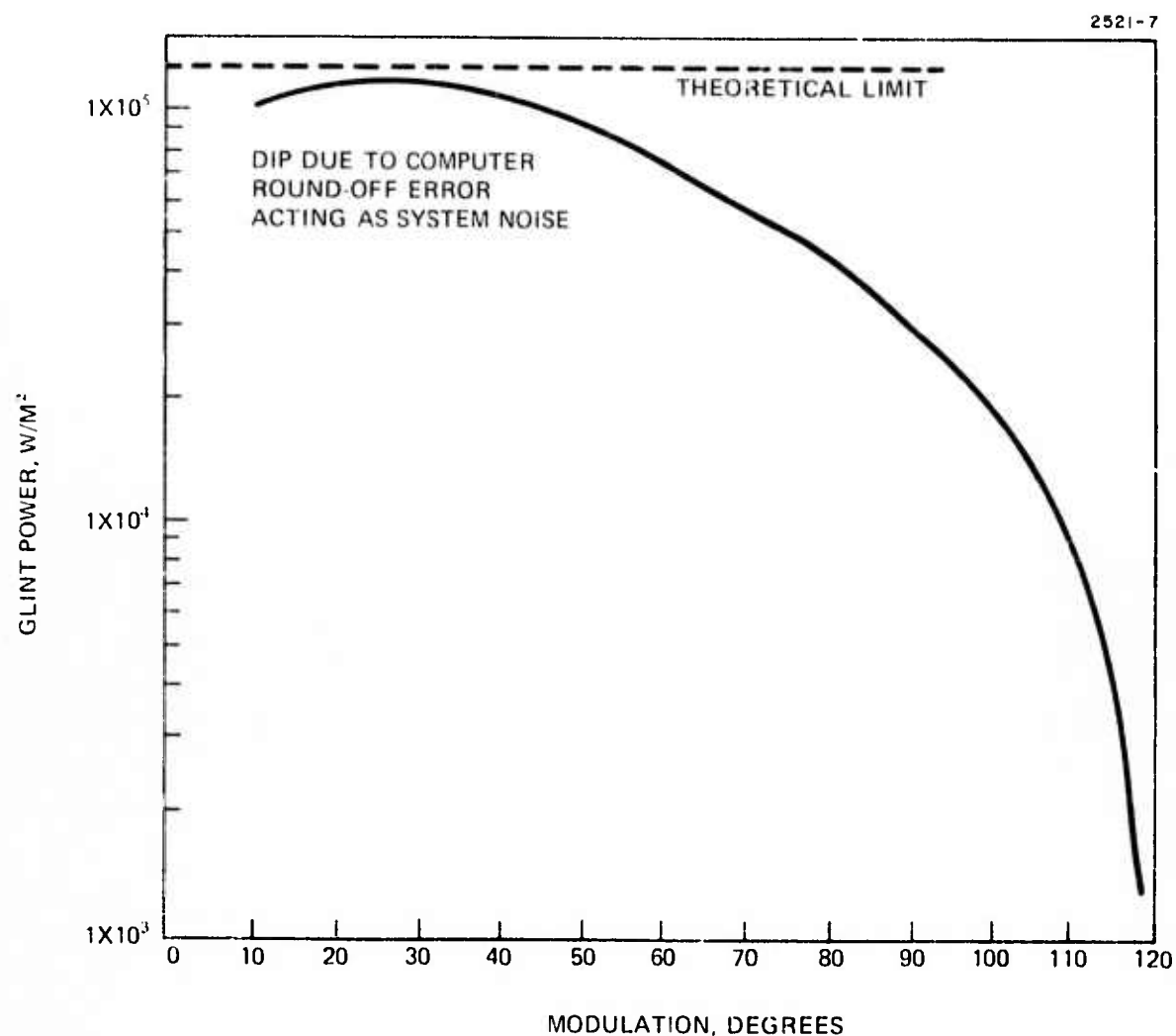


Fig. 13. Glint power as a function of dither modulation for a 1 x 9 element array.

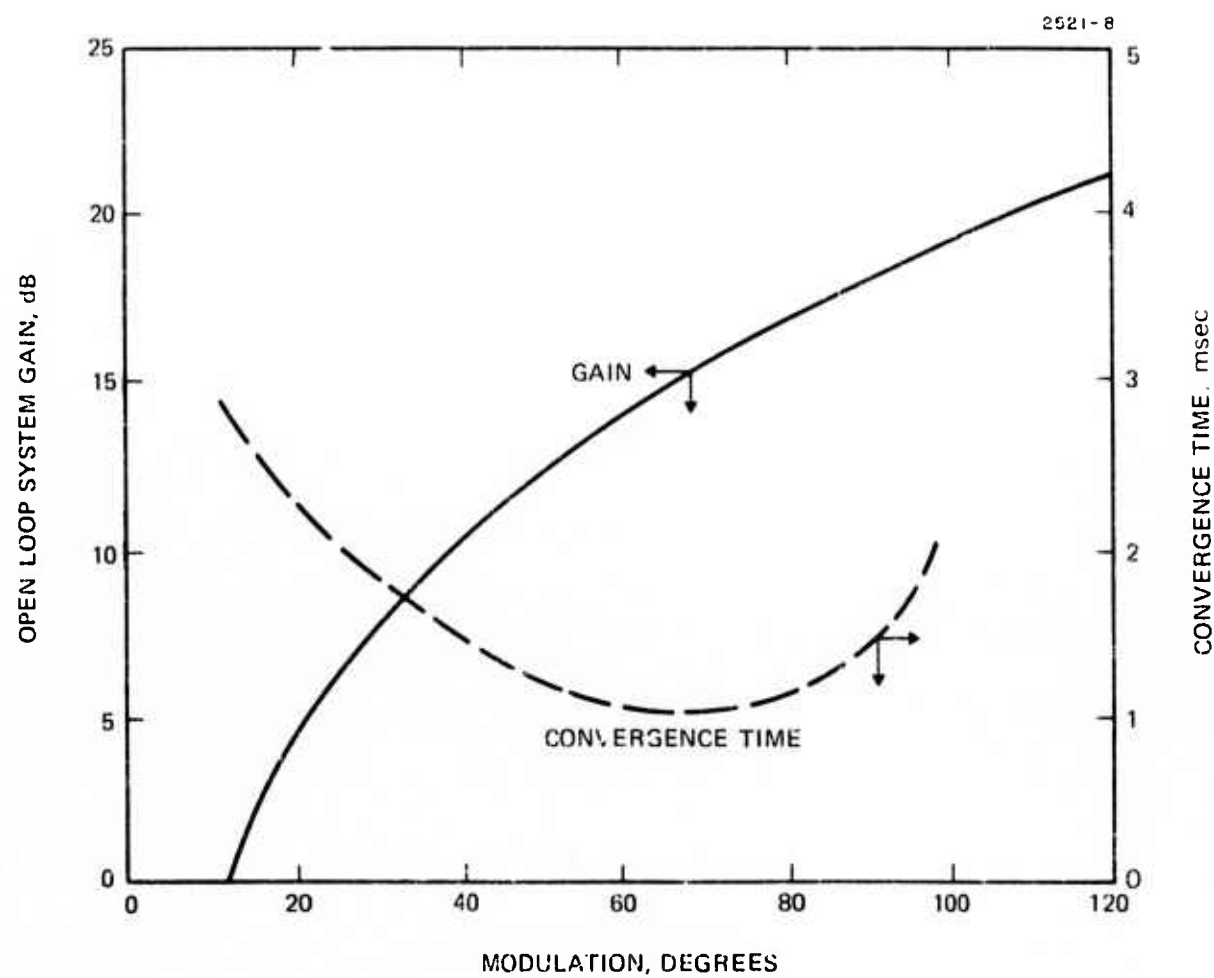


Fig. 14. System gain and convergence time as a function of modulation.

optimum will exist. Figure 14 shows open-loop gain and convergence time as a function of modulation index. System gain is increased by greater modulation as expected and the system does converge faster as a result of the higher gain. But at the minimum convergence time ( $\approx \pm 70^\circ$  modulation) the glint power is decreased by 3 dB, and beyond this point the time to converge greatly increases while power decreases rapidly due to large beam excursions. The criterion of maximum power delivered on target would probably govern, so that lower indices (20 to  $30^\circ$ ) would be employed, and the convergence time decreased by changing some other gain-controlling parameter.

c. Dither Spacing - The separation between dithers, the relative phasing of the dither generators, and the low-pass filter roll-off characteristic, all impact on the amount of modulation feedthrough seen on each control channel and on the power at the point. The purpose of these runs was to determine the amount of feedthrough obtained using the proposed filtering scheme. Figures 15 and 16 show the results of shifting from 1 kHz to 1.5 kHz dither spacing. It should be noted that the computer program generates dither signals that are phase coherent; i.e., they all zero cross at  $t = 0$ . Thus, there are periodic points where the phases align. These points are denoted in Fig. 15 as the 1- and 2- kHz feedthrough points, and the peak excursions are between 25 to 35% of the average glint power. By increasing the glint spacing to 1.5 kHz the peak fluctuation decreases to less than 15% of the average power as seen in Fig. 16. In the actual hardware, however, the dithers will be generated by employing an independent dither oscillator either per channel or every 2 channels; such oscillators will have randomly-distributed initial phases, thus suppressing the large "synchronous" dips in glint power. Therefore, operation at 1 kHz spacings with the present filter design would probably be acceptable. To be on the safe side, logarithmically spaced frequencies will probably be employed in the experimental model.

#### 7. Work in Progress

Since the design review meeting in mid-June, work has concentrated in four areas:

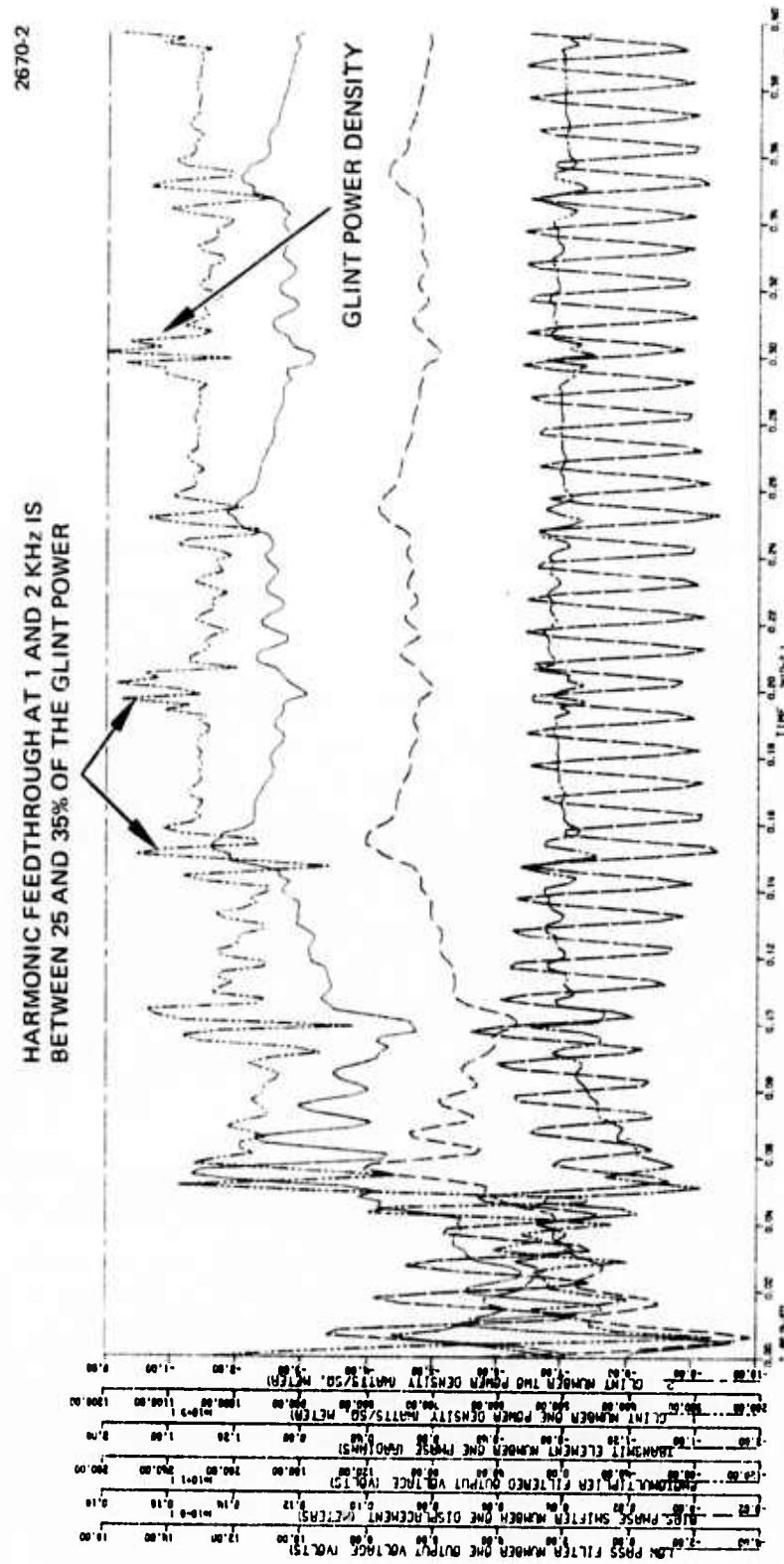


Fig. 15. Dither feedthrough and synchronism for a 1 KHz dither spacing.

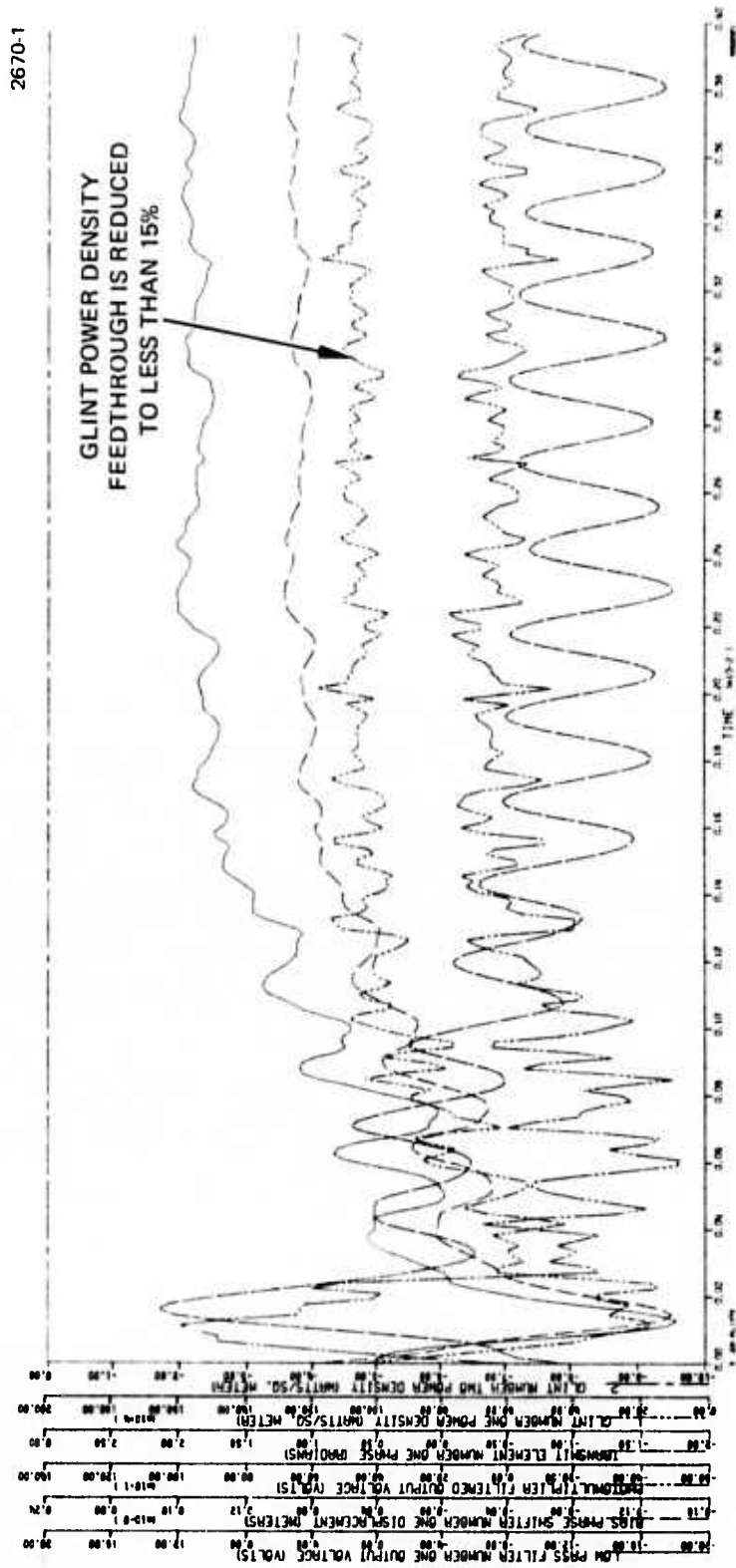


Fig. 16. Dither feedthrough for 1.5 KHz dither spacing.

- Independent verification of simulation analysis
- Development of moving target subroutine
- Modification to incorporate 0-6-12-18 near-circular array configuration
- Development of a subroutine to compute and plot target plane power density.

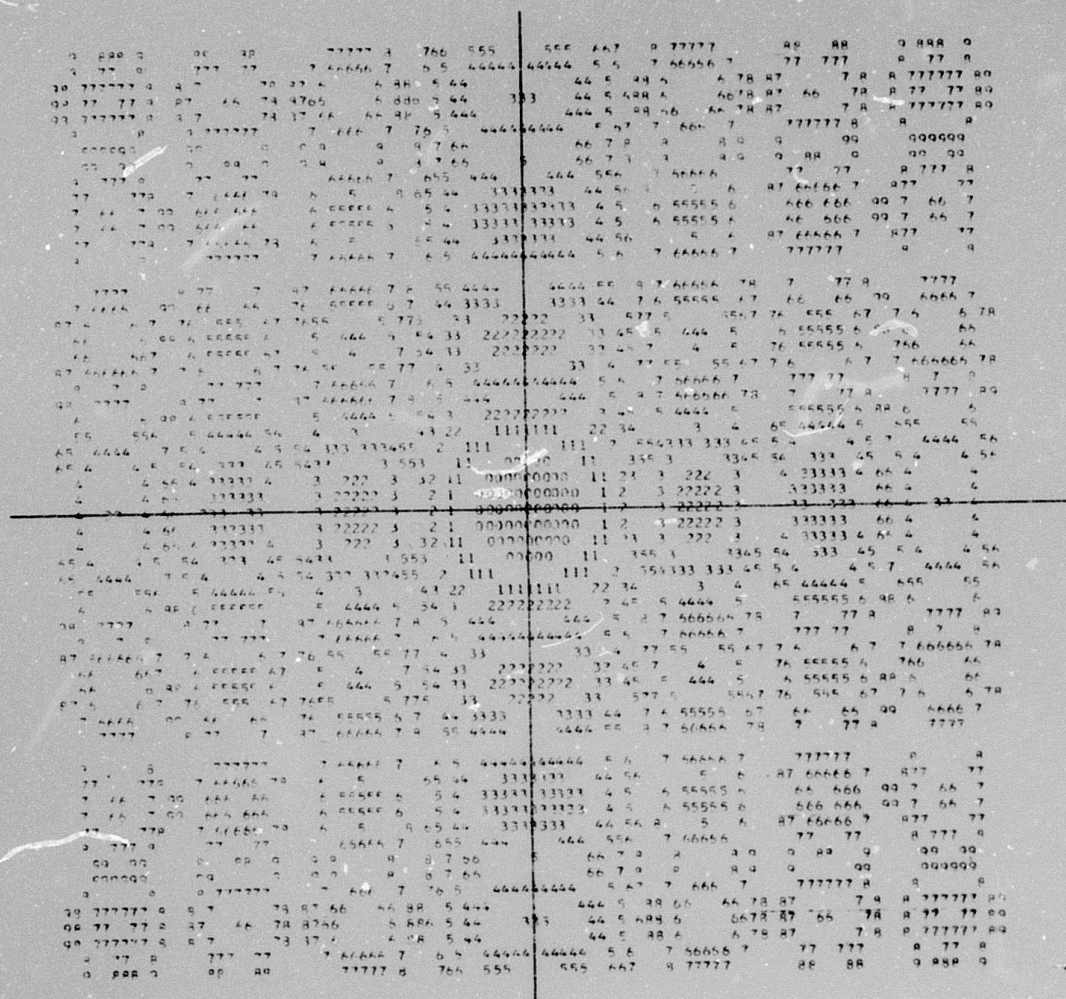
As mentioned previously, the first of these tasks has verified the accuracy and completeness of prior work. In the second area, the subroutine (MOVEIT) has been coded and debugged. The fourth task is complete for arrays of square elements. The near-circular array coding is currently being tested to verify its accuracy, and when this has been done, the target plane power pattern map computation follows naturally.

Figure 17 is a target plane power map produced for a 4 x 4 array of square elements. It is fairly easy to see the power contours and sidelobe structure. The total size of the map is 1 x 1 element beamwidths, therefore, we would expect a main lobe and three sidelobes in each direction. It can be seen that the sidelobe levels are near theoretical values for a square array. Figure 18 used the same subroutine, but with array phase data taken from the 4 x 4 baseline test discussed previously. Final control phase shifter voltages were used without editing. The plot showed the glint position at the location of the star. The beam had formed almost directly centered on the glint, and the sidelobe structure was somewhat muddled. The appearance of a small grating lobe on the right side is obvious.

It is anticipated that program checkout will be complete by mid-August; and simulation of planned range tests will begin at that time.

#### D. Beam Offset Techniques

The basic objective of a COAT system is to create a well-formed beam on a reference point — historically a strong glint. Unfortunately, a strong glint is frequently not a desirable aim point and even if it is, there will be problems in holding the beam on it, particularly under conditions of target-beam interaction.



LEGEND	
CHARACTER	POWER (dB)
0	0 - 3
1	-6 - 9
2	-12 - -15
3	-18 - -21
4	-24 - -27
5	-30 - -33

Fig. 17. Intensity plot of far-field pattern from planar  $4 \times 4$  array of contiguous square elements.  
Array converged on bore sight.

Reproduced from  
best available copy.

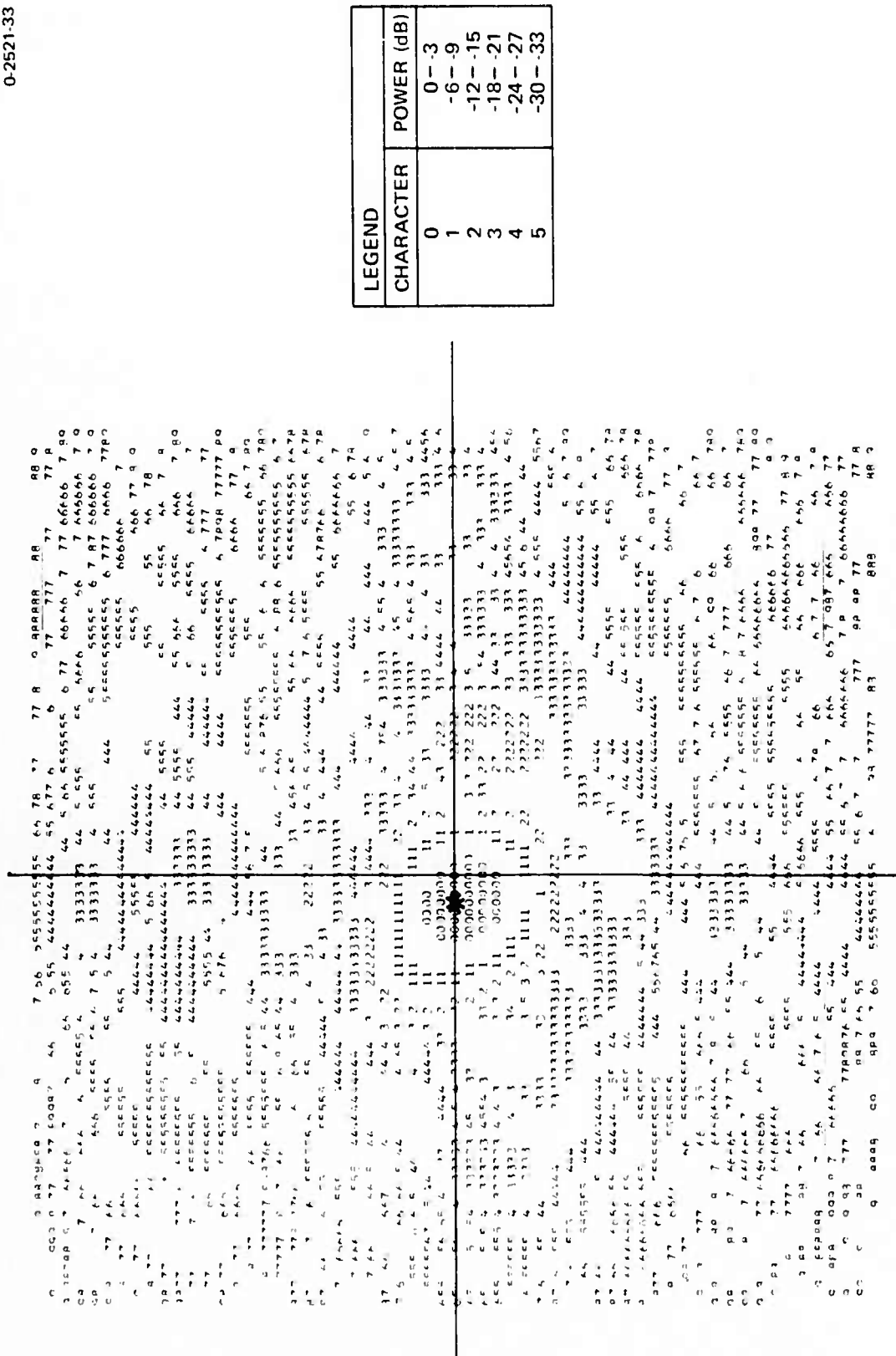


Fig. 18. Target plane square-element array power pattern.

There are two basic ways of handling this problem: (1) The control system can be modified so that it converges on other types of references, and (2) one may employ beam offset systems which move the beam (or some portion of it) to target areas which are not natural reference points. These offset systems can be separated into two basic types: (1) Time-shared systems, and (2) simultaneous or ghost-beam systems. We have considered only the time-shared systems in this report. Ghost-beam systems were discussed briefly in our proposal.

Time-shared offset systems operate in two cycles that may either be one-shot (for short pulse operation) or iterated (for long pulse or cw operation). In a time-shared system, the first cycle is devoted to forming the beam on the reference, while the second cycle, which must be accomplished within one atmospheric time constant, scans the beam to the selected offset point. This is achieved by placing the phase shifter control voltages in a hold condition while an additional slewing command is employed to quickly move the formed beam to a new target position before the state of the atmosphere can change. If the beam must remain in its offset position for more than an atmospheric time constant, which is the most frequent case of interest, then recycling of the beam-forming operation is required.

There are two approaches to the slewing function: (1) An electronic phase control with progressive phase shift signals applied to the phase shifters, and (2) a high-speed microslewing mirror. Each approach to time-shared offset has certain advantages. The use of electronic offset slewing has a potential speed advantage, provided that advanced electro-optic or acousto-optic phase shifters are employed; however, a high-speed slewing mirror is probably the more attractive solution when employing mechanical phase shifters since it reduces demands on settling times and dynamic range in the phase shifters. We will study both techniques in the experimental program.

An electronic beam-offset system employs four basic functions, which are replicated in all control channels: (1) A memory or hold circuit which samples the atmospheric compensating voltage on the phase shifter, in a converged state, and holds it constant during the offset scan. (2) a technique for introducing additional offset voltages which are constant during

the offset interval for any one control channel but which progressively increase in value across the ensemble of channels (assuming equal bimorph sensitivity). (3) a protective switch which prevents transient error signals, generated by the offset process, from impacting the control system. (4) a "state-return" system which, after the removal of the scan voltages, returns the input of the servo filter to its initial state before the commencement of the scan process. Of course, this original state is only an approximation of the desired correction voltage, at the completion of the offset cycle, since the atmosphere has slightly changed its state during the offset interval. Nevertheless, the original state information should be sufficiently accurate that "glint" reacquisition time is appreciably reduced by returning to it.

The microscanning mirror approach requires similar functions except that in place of the introduction of scan voltages to the phase shifters, function (2), one applies an appropriate voltage to the microscanning mirror.

The block diagram which achieves these functions for electronic offset is illustrated in Fig. 19. Switches  $S_1$  and  $S_2$  are operated in synchronism. Switch  $S_1$  supplies the protective function while  $S_2$  separates the "last" capacitor in the loop filter from its discharge resistor to supply the holding function. Switch  $S_3$  is the state-return switch.

The time development of these functions for "typical" elements (#1 and #2) is illustrated in Figs. 20(a) and 20(b). The slowly varying waveform represents the control system error signal as it responds to atmospherically induced error signals.

Alternatively, if the microscanning mirror approach is employed, typical slew-dwell-recycle sequence waveforms are illustrated in Fig. 21.

#### E. Alignment Error Analysis

There exists four basic classes of "alignment" errors in phased arrays which may result in peak power or array gain loss: (1) Gain or excitation variations from element to element, (2) phasing errors from element to element, (3) element centering or position errors, and (4) element pointing errors.

2521-10

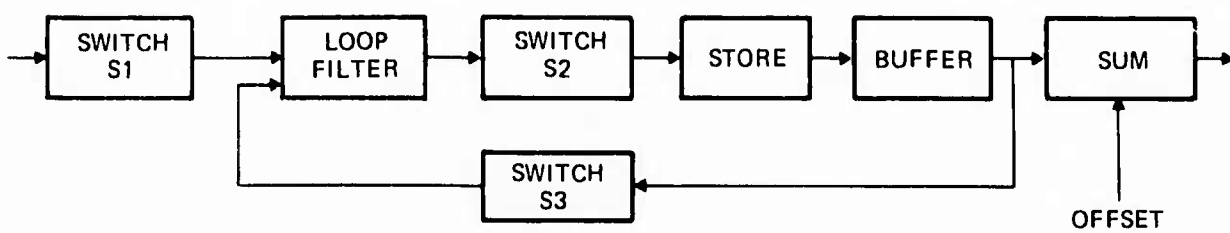


Fig. 19. Electronic beam offset system.

2521-11

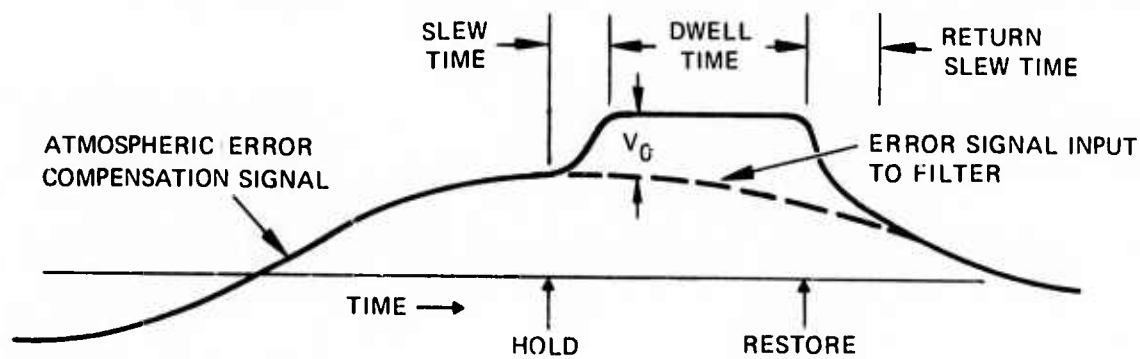


Fig. 20(a). Phase-shifter drive voltage on channel No. 1 (electronic offset).  $V_0$  is the offset voltage.

2521-12

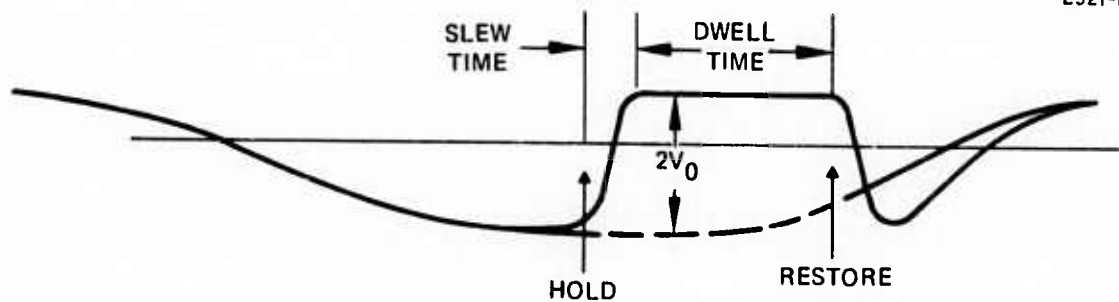


Fig. 20(b). Phase-shifter drive voltage on channel No. 2 (electronic offset).

2521-13

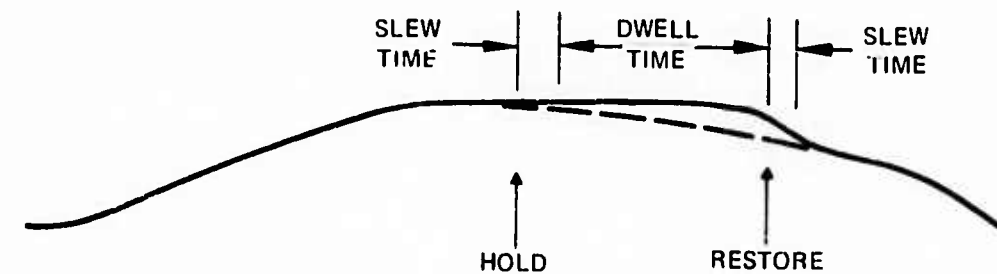


Fig. 21. Phase-shifter drive, channel No. 1 (microslewing offset).

A fifth "alignment" problem results from electronically scanning the array pattern away from the center of the element pattern. In microwave systems this pointing error or mismatch is generally accepted as inevitable. However, it can be eliminated or at least minimized in the case of optical systems by repointing the elements to bring their peak back into registration with the array peak (auto blazing).

The first two classes of error have been extensively studied in the literature on microwave phased arrays. Given a perfect control system, element-to-element phasing errors are eliminated by the COAT control system. Similarly, the servo system can be designed to eliminate amplitude errors (on an element-to-element basis); however, the present system does not include this capability. Both types of error are included in the mean (normalized) gain degradation equation

$$\frac{\langle G \rangle}{G_0} = \frac{(1 - \langle \alpha \rangle)^2 e^{-\Delta^2}}{1 + 2\langle \alpha \rangle + \langle \alpha^2 \rangle}$$

where

$\Delta^2$  = mean-square phase error (radians)

$\langle \alpha \rangle$  = mean amplitude error

$\langle \alpha^2 \rangle$  = mean-square amplitude error

and the nonuniform (degraded) field distribution which defines  $\alpha$  is

$$A(R') = A_0(R') [1 - \alpha(R')]$$

where  $A_0$  is the desired or uniform distribution and  $\alpha(R')$  is the (undesired) variation in field distribution as a function of vector position,  $R'$ . The effective gain loss is plotted in Fig. 22 over a limited range of  $\Delta^2$  with  $\langle \alpha^2 \rangle$  as a parameter. The solid curves assume

$$\langle \alpha \rangle = \sqrt{2/\pi \langle \alpha^2 \rangle}$$

while the dashed curves assume  $\langle \alpha \rangle = 0$ .

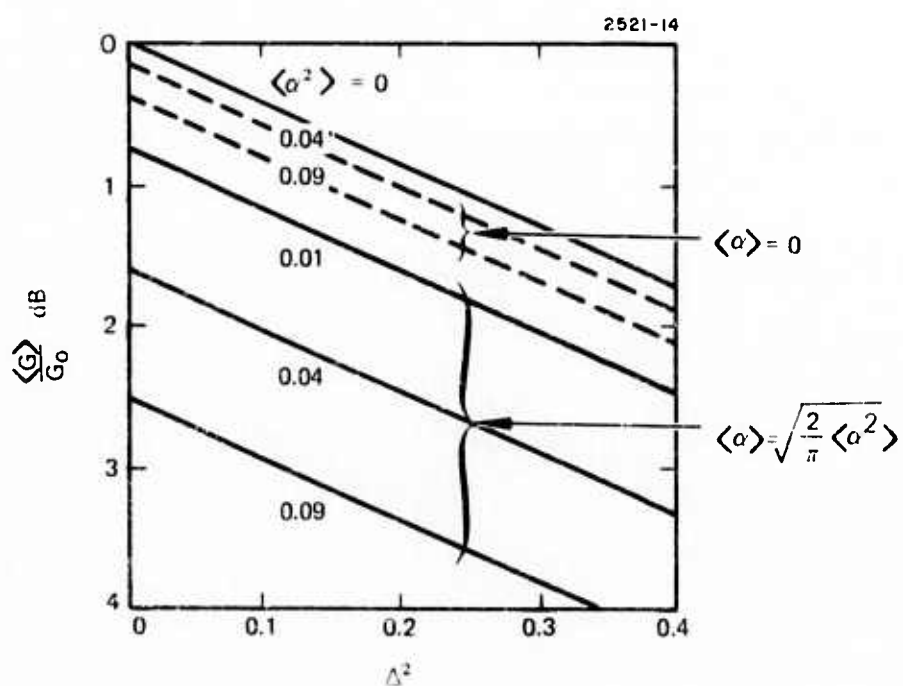


Fig. 22. Power loss from random phase and amplitude errors.

The alignment errors associated with element pointing variations are of little consequence with a microwave system since the elements are normally a fraction of a wavelength in length and, in consequence, the element beamwidths are quite wide with respect to normal mechanical tolerances. In a typical optical phased arrays this is no longer true. For the cophased condition ( $\Delta = 0$ ) the element pattern exhibits an essentially quadratic reduction in power delivered as a function of pointing error for large classes of excitations (e.g., uniform rectangular, uniform circular, truncated Gaussian, etc.), however, with the "constant" having a weak dependence on the error. Thus the normalized power loss over  $N$  elements is well approximated by

$$\frac{P_{AE}}{P_A} = 1 - \frac{0.33}{N} \sum_{n=1}^N K_n^2, \text{ for small errors}$$

$$\frac{P_{AE}}{P_A} = 1 - \frac{0.3}{N} \sum_{n=1}^N K_n^2, \text{ for medium-sized errors}$$

where  $K_n$  is the fractional pointing error of the  $n^{th}$  element. If one defines an rms fractional pointing error,

$$K_{rms} = \left\langle \frac{1}{N} \sum K_n^2 \right\rangle^{1/2}$$

then these results are summarized by the curve illustrated in Fig. 23.

The actual element pointing errors to be expected of the system arise from several uncorrelated effects.

Static Errors,  $\sigma_{stat}$ : The static mirror mount errors are expected to be 0.3 sec rms in each of two mounts.

Thermal Error,  $\sigma_{therm}$ : The dominant thermal error effect is assumed to arise from flexure of the support plate. This is computed to be 0.2 arc sec rms.

Dynamic Error,  $\sigma_{dyn}$ : The assumed seismic inputs are negligible. A noise level between 65 to 75 dB is assumed, which vibrates two masks and two mirrors, giving

$$\sigma_{\text{dyn, mount}} = 0.7 \text{ arc sec rms}$$

$$\sigma_{\text{dyn, mask}} = 1.4 \text{ arc sec rms}$$

The composite rms angular error then becomes

$$\begin{aligned}\sigma_{\text{tot}} &= \sqrt{2(\sigma_{\text{dyn, mount}})^2 + 2(\sigma_{\text{dyn, mask}})^2 + 2(\sigma_{\text{stat}})^2 + (\sigma_T)^2} \\ &= 1.6 \text{ arc sec.}\end{aligned}$$

Given an allowable error of 7.0 arc sec (1/10 element diffraction angle), this allows a budget of 6.7 arc sec for error sensing.

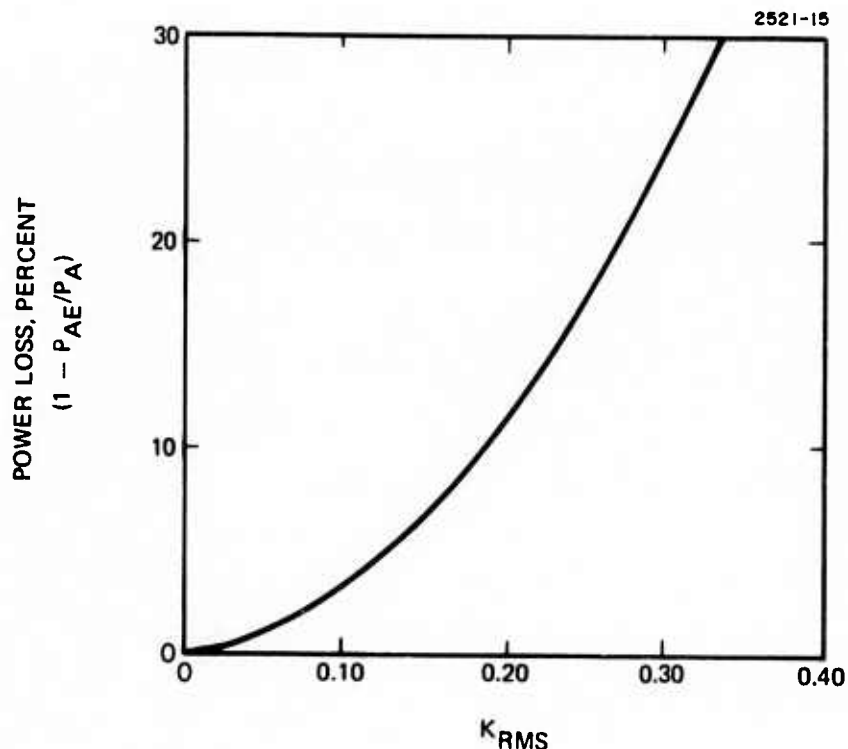


Fig. 23. Peak power loss from element positioning errors.

## SECTION III

### DESIGN

In this section we present the design of the COAT experimental equipment, target system and instrumentation. Experimental results supporting specific design details are also reported here rather than under the previous analysis section.

#### A. Phasor Matrix

The phasor matrix in the COAT system is that portion that takes the beam from the laser, divides it spatially into separate paths for phase shifting and then recombines it in the desired radiating array pattern. Different phasor matrix configurations were discussed in our proposal with respect to their applicability to ultimately operational COAT systems and also with respect to their flexibility for the present experimental program. In the proposal the axisymmetric spindle or "Christmas Tree" structure was identified as a prime candidate for operational systems. The key requirement of the present program, however, is the ability to change radiating array patterns easily without major reconfirmation of the system. The Christmas tree arrangement was not flexible in that sense and so was not considered for the present experiment. Instead, a multiple reflective mask structure was proposed. A careful analysis of the alignment and flatness tolerances required of the configuration described in the proposal indicated that version would be difficult to fabricate.

A superior substitute has been found for that design, one that may be thought of almost as the dual. In the old version a single large beam was reflected back and forth between two mirrors, with clear mask patterns etched in the reflecting coatings. An elemental portion was removed through a clear portion of the mirror on one pass, reflected off a phase shifter and then recombined into the main stream on the next pass.

The principle used in the new version is illustrated in Fig. 24; it is the dual in the sense that an elemental portion is removed and recombined by

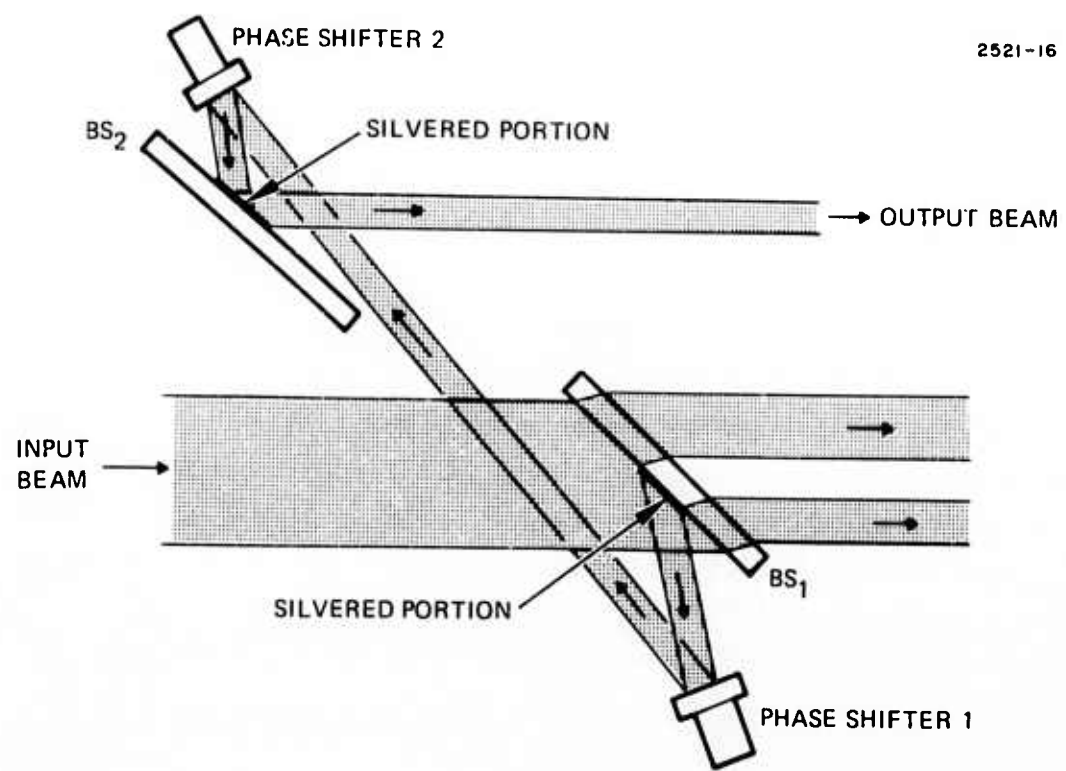


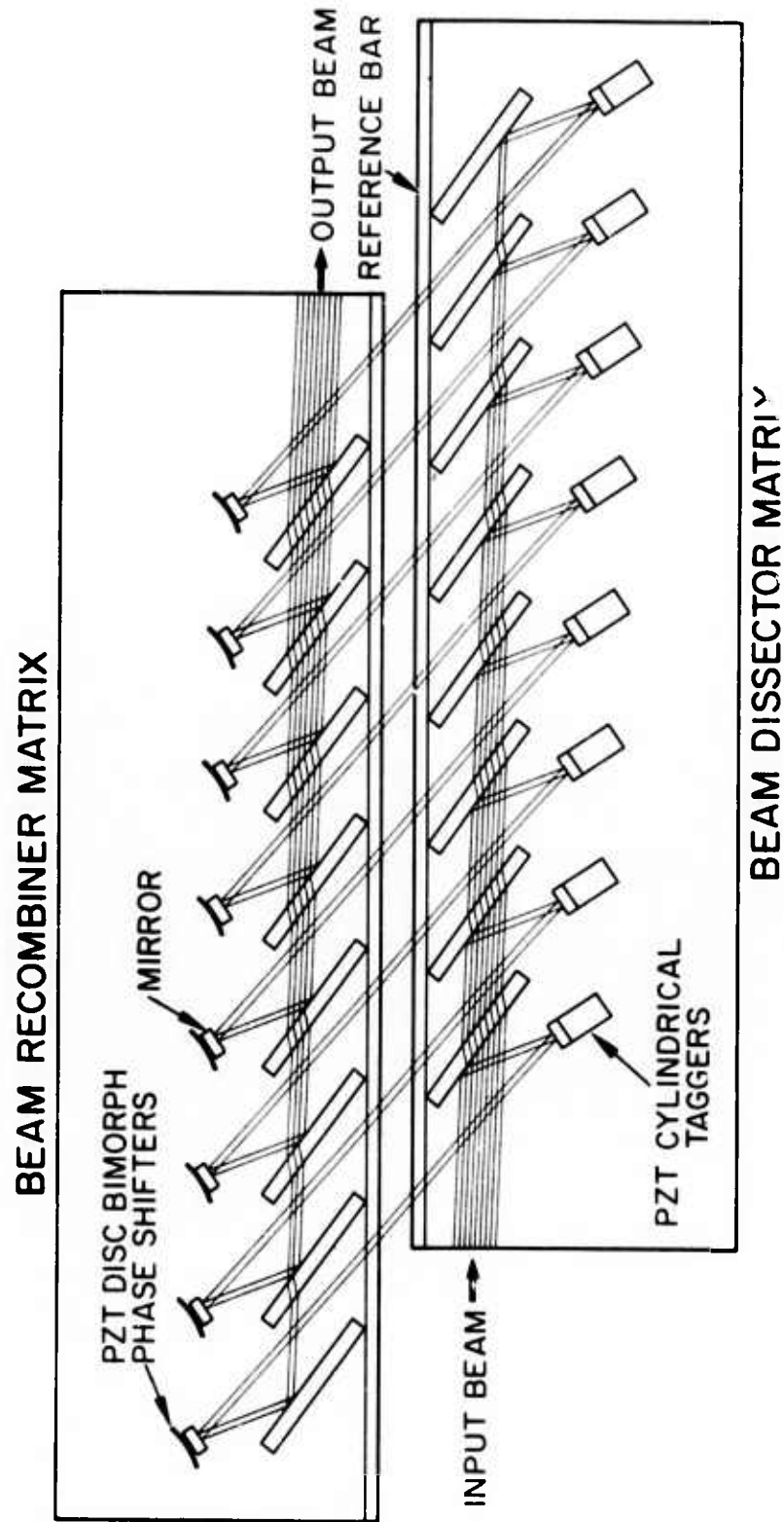
Fig. 24. Sketch illustrating how an elemental pattern is removed from the beam, tagged, phase shifted, and then returned to an array.

reflection rather than transmission while the main streams are passed on by transmission rather than reflection. In the sketch shown, a large collimated beam is incident on a glass plate oriented at Brewster's angle, to minimize first surface reflections. A small silvered portion in the shape and location of one element of the desired array reflects a portion of the incident beam toward the first of two mirrors mounted on piezoelectric drivers which serve as the dither tagging and control phase shifters respectively. The second phase shifter mirror directs the beam toward similarly shaped and located silvered spot on another plate which serves to reflect the elemental beam in a direction approximately parallel to, but displaced from, the incident beam. Figure 25 illustrates how a series of such "reflective dot" plates can be used to form an array of independently phase shifted elements. The advantage of this scheme is that more adjustment is available for alignment over that described in the proposal.

In order to test the practicality of this scheme, an 8-element version was built using simple mirrors in place of the phase shifters. A photograph of the test setup is shown in Fig. 26 (which has approximately the same orientation as Fig. 25 for comparison). Eight rectangular dots are employed in a horizontal  $1 \times 8$  array in this simple test. An alignment procedure was developed which allows rapid adjustment of the phase shifter mirrors once the masks have all been properly oriented and fixed in place (a one-time alignment). A photograph of both the "spent" beam from which eight elements have been removed and the "output" beam consisting of the eight recombined elements is shown in Fig. 27.

In the 18-element version, pattern interchange will be accomplished by interchanging sets of masks. The entire set of 36 masks will be mounted and separately aligned on a single plate that may be removed from the setup independently of the phase shifters. In this way, array patterns may be interchanged and the system realigned in less than an hour.

Two basic layout grids for 18-element arrays were chosen and are illustrated in Figs. 28 and 29. For rectangular patterns, a 64-element  $8 \times 8$  layout was chosen for the purpose of allowing a variety of choices of 18-element arrays, including thinned arrays. The axisymmetric pattern, 0-6-12 (Fig. 29) was chosen as the prime candidate for the experimental program (see the later discussion of array choice).



BREWSTER ANGLE  $\approx 33^\circ$   
 BEAM SPLITTER REFERENCE ANGLE  $2.25^\circ$   
 ELEMENT BEAM WIDTH  $3\text{mm} \times 3\text{mm}$   
 BEAM WALK-OFF  $3\text{mm}$  PER PLATE

Fig. 25. COAT phasor matrix array optomechanical test.

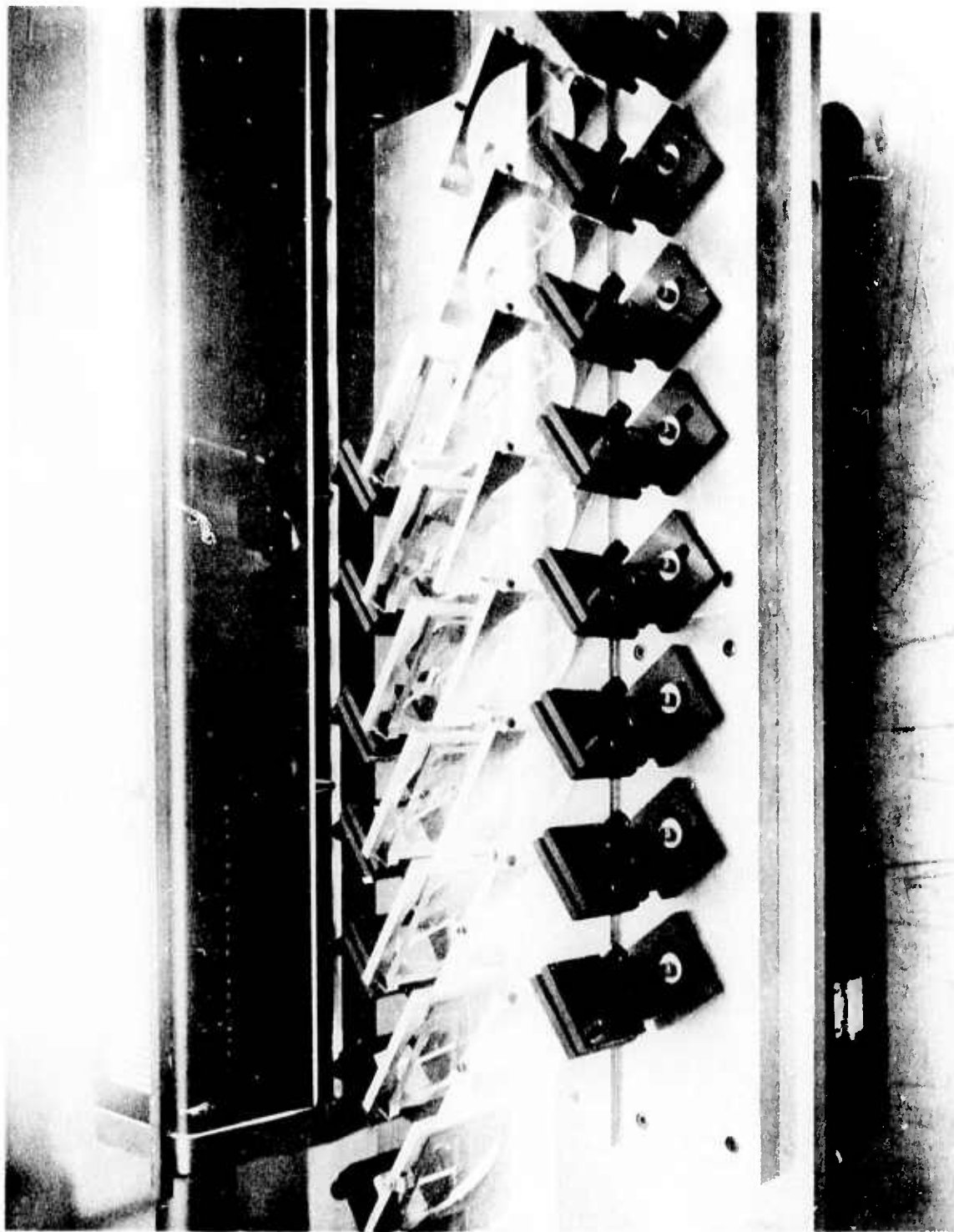


Fig 26 8-element phasor matrix test setup

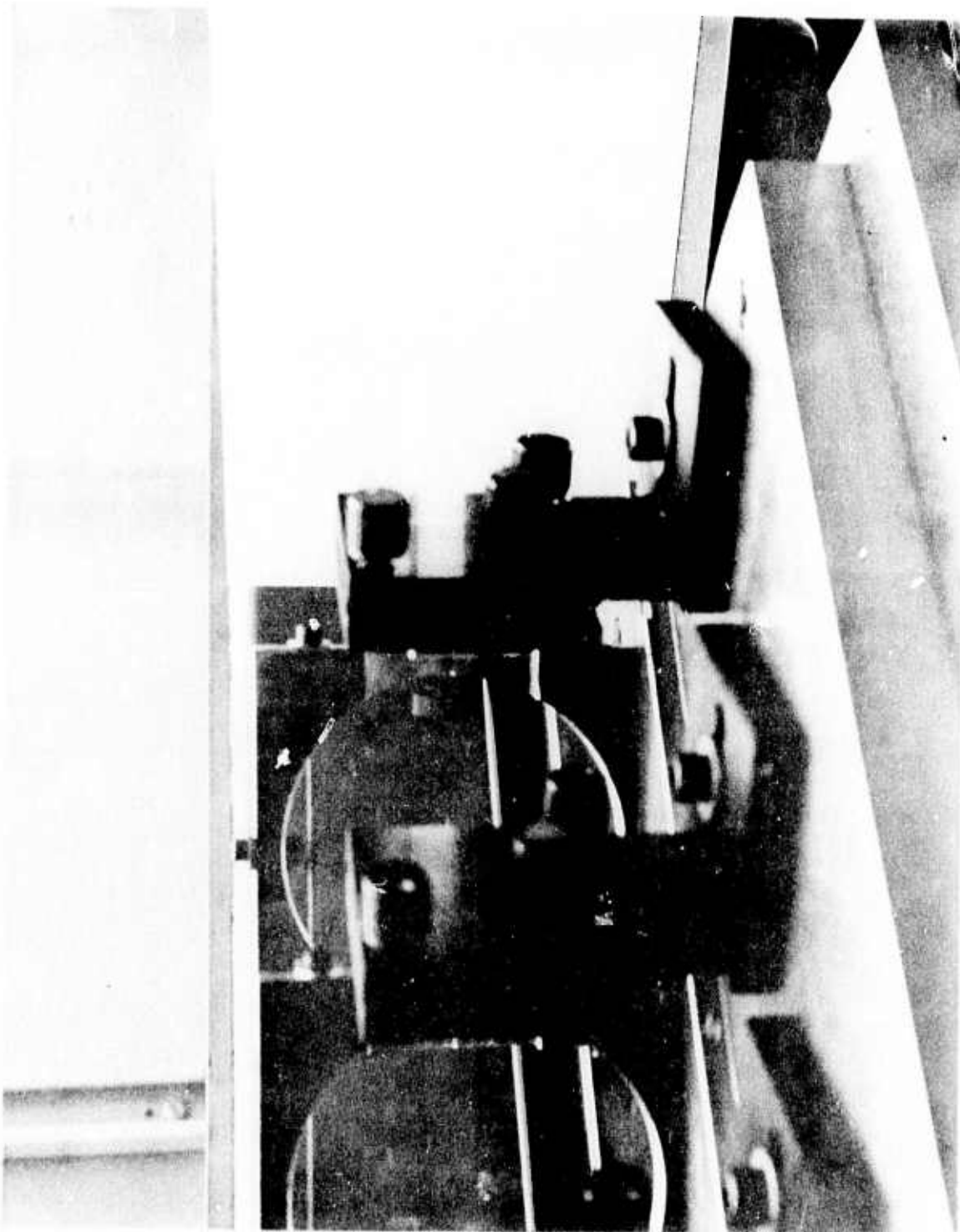


Fig 27 Output beam from 8-element test setup

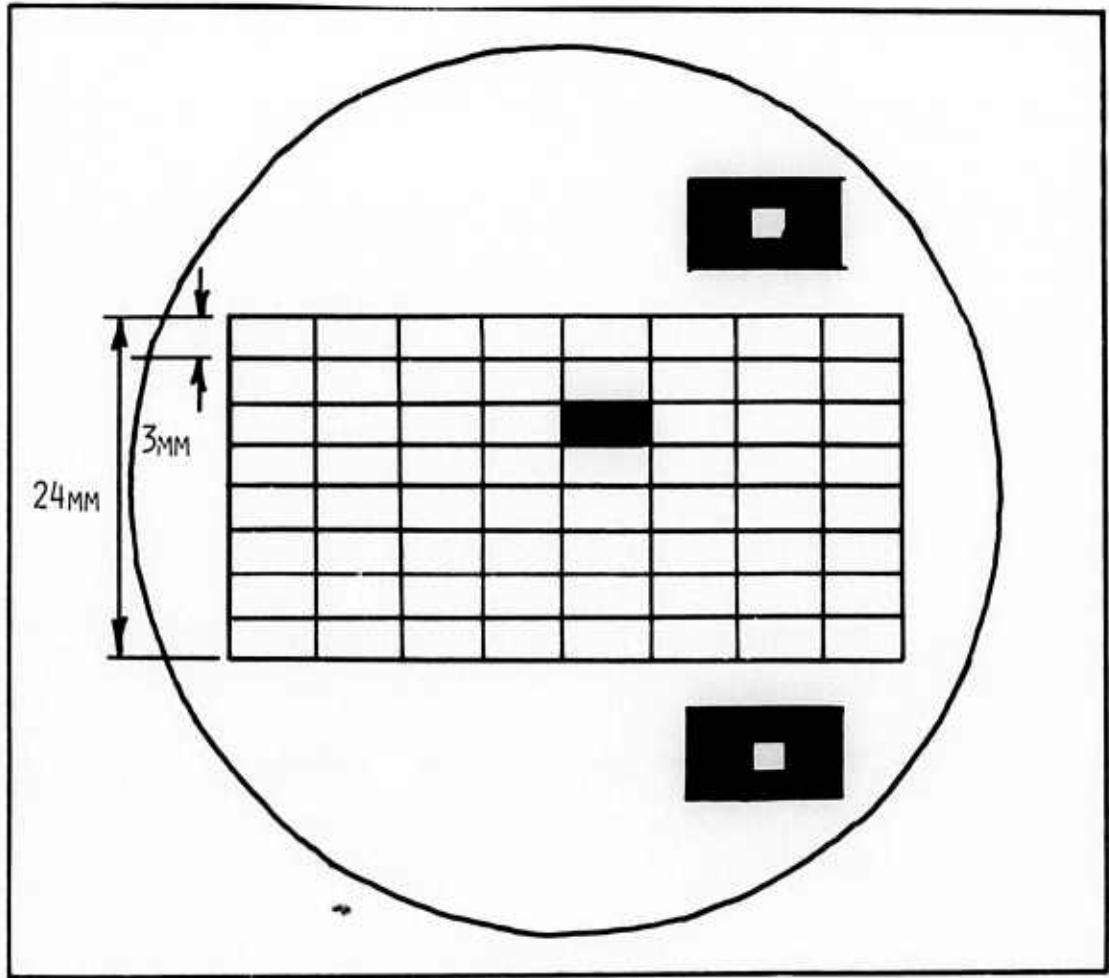


Fig. 28. Mask layout for 8 x 8 thinned arrays.

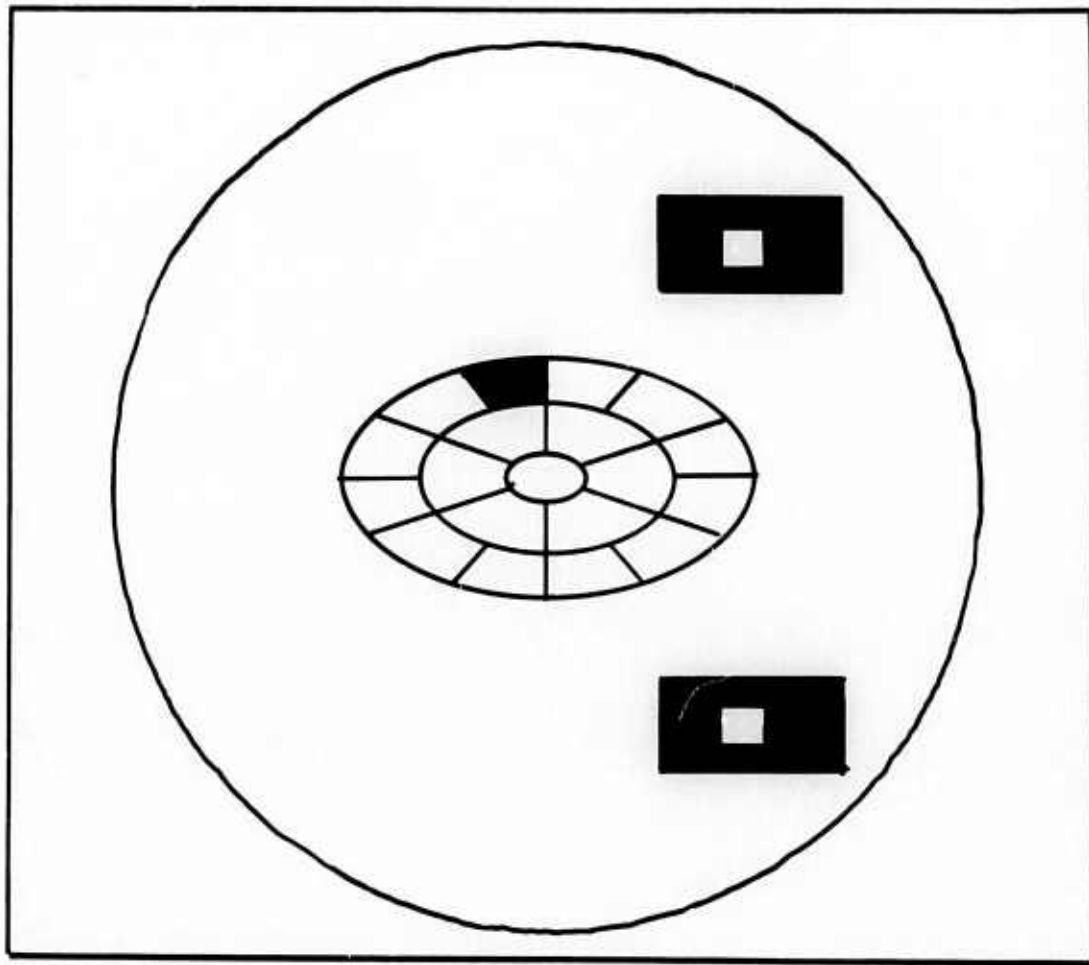


Fig. 29. Mask layout for 0-6-12 array.

B. Phase Shifters and Taggers

Selection of transducers for optical phase shifting in the experimental COAT system requires a tradeoff among sensitivity, speed, dynamic range, stability, and cost. These criteria were first applied to the various available approaches to eliminate the less desirable techniques. As an example, electro-optic techniques were eliminated on the basis of low sensitivity and high cost as discussed in the proposal. Electromagnetic techniques were investigated briefly using a selection of commercial and custom transducers but were eliminated due to high driving power, thermal drift, and high fabrication costs.

After elimination of the less desirable approaches, attention was focused on piezoelectric effects for the required transducers. Piezoelectrics in general offer low power dissipation, good stability and relatively low cost. By varying the material and configuration of the transducers, many combinations of speed, dynamic range and sensitivity may be achieved. The main thrust of the transducer selection program was expended in an investigation of the characteristics of various piezoelectric configurations to determine the best compromise for this application.

1. Phase Shifter Requirements

Piezoelectric devices are basically field sensitive devices, generally providing increasing displacement directly with voltage. A search was made for an electronic amplifier capable of providing high voltages at reasonably high frequencies. The Philbrick/Nexus 1022 operational amplifier was chosen as a high speed, stable device capable of providing  $\pm 135$  volts. All transducer selection is based on this driver. Based on a minimum dynamic range of  $\pm 2\pi$  rad, a wavelength of  $0.488 \mu m$ , and the mechanical layout discussed earlier in this report, it was determined that the phase shifter must have sensitivity of at least  $450 V/\mu m$ .

System decisions placed a closed loop bandwidth requirement of 400 Hz on the individual servo loops. To achieve this bandwidth in a stable manner, the fundamental resonance of the phase shifter must fulfill certain criteria. The gain and phase of a servo system with a 400 Hz unity gain frequency and a 6 dB/octave filter are plotted (Fig. 30). Superimposed on these curves

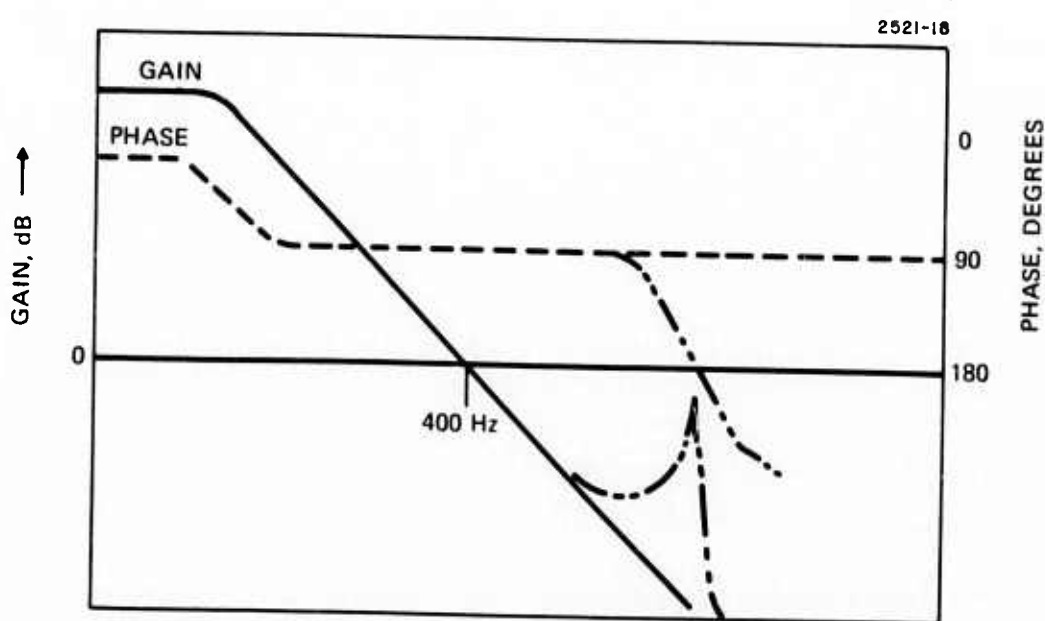


Fig. 30. Phase shifter resonance effects.

are the gain and phase introduced by a resonant device such as the mechanical phase shifter being considered. If the resonant peak shown exceeds 0 dB, the system will be unstable. Quantitatively, the peak will just touch the 0 dB line if the ratio

$$\frac{\text{resonant frequency}}{\text{peak gain}} = 400 \text{ Hz.}$$

(Peak gain is defined as the ratio of transducer sensitivity at the resonant peak to sensitivity at low frequencies.) For stable servo operation, the above ratio should be much greater than 400 Hz.

## 2. Phase Shifter Configurations

Piezoelectric materials are generally too insensitive to use directly as phase shifters and satisfy the  $450 \text{ V}/\mu\text{m}$  criterion. Some means of magnifying the sensitivity must be adopted. One technique that was investigated consists of stacking a large number of piezoelectric disks in series to form a long cylinder. These discs are then driven in parallel electrically by interconnecting alternate electrodes located between the discs. This approach maintains very high rigidity and thus a very high resonant frequency. In theory, any desired sensitivity may be achieved by increasing the number of discs. This approach was investigated, but has been temporarily ruled out due to the high cost of fabricating such stacks. In large quantities for future systems, this technique may be the preferred approach.

The most promising piezoelectric configuration for the present experiment consists of a two-layer device of oppositely-poled material that bends when a field is applied, commonly referred to as a "bender bimorph". This configuration trades the inherent high rigidity of the piezoelectric materials for increased sensitivity. Figure 31 shows the response of a 1 in. disc of Clevite PZT-5H material in a 0.020 in. thick bimorph configuration. A small mirror was cemented to the center of the disc and the edges clamped. Sensitivity is much higher than necessary, but the resonant ratio is too low for proper operation. Table VII lists some of the experimental modifications of this basic device that were tested to trade off sensitivity for better resonant characteristics. Active or feedback techniques were tried, where

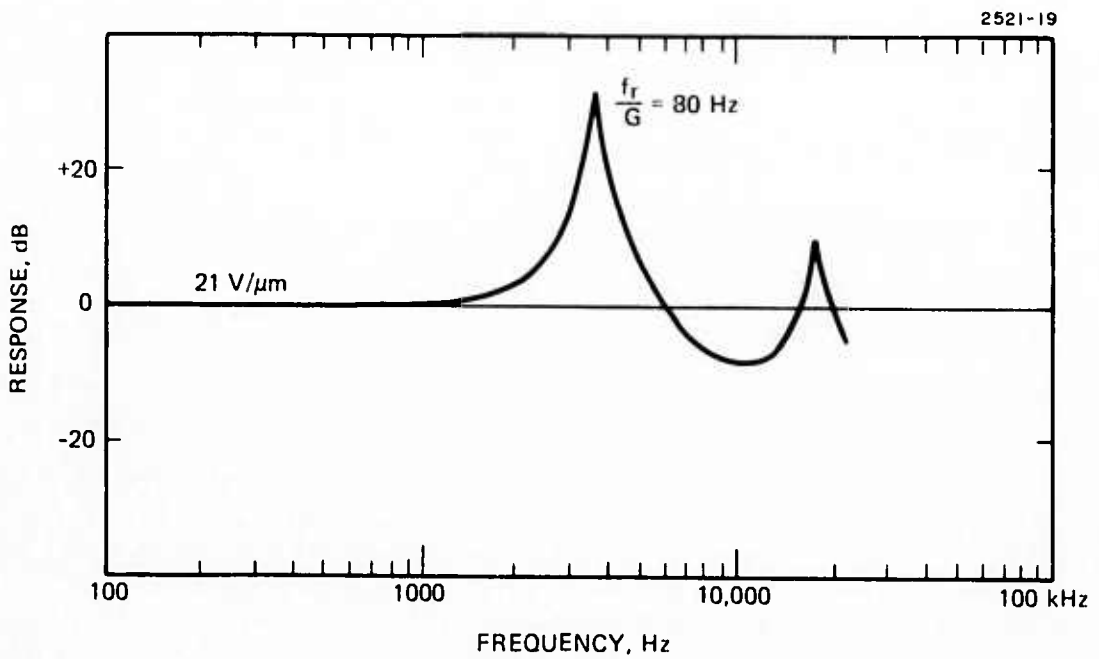


Fig. 31. 1-inch diameter bimorph response.

the displacement of the bimorph was sensed and fed back to maintain flat response, but these experiments were not satisfactory. The bimorphs were also modified mechanically, and three satisfactory configurations were found. The best of these, both from the standpoint of performance and of cost, was found to be a reduction in diameter from 1 in. to 1/2 in. Figure 32 shows the response of the 1 in. and 1/2 in. bimorphs compared. The sensitivity of the 1/2 in. bimorph is still nearly four times better than required, and the resonant ratio has been increased to nearly 1 kHz.

TABLE VII  
Bimorph Phase Shifter Configurations

Active (Feedback)	Problem
1 in. Bimorph Microphone Pickup	Nonlinear
1 in. Bimorph Strain Gage Pickup	Resonant Pickup
1 in. Bimorph Mechanical Pickup	Poor Correction
<b>Passive</b>	
1 in. Bimorph	Low Resonance
1 in. Damped Bimorph	OK - Drifts
1 in. Bimorph, 3/32 in. thick	OK
3/4 in. Bimorph	Low Resonance
1/2 in. Bimorph	Best

To further improve the resonant ratio, an electronic notch filter was placed in series with the bimorph. The combined response, shown in Fig. 33, has a resonant ratio of 4600 Hz, more than an order of magnitude greater than required.

### 3. Tagger Requirements

The dither frequency tagger is required to provide a single frequency phase modulation with a maximum phase excursion of  $\pm 30^\circ$ . Using

2521-17

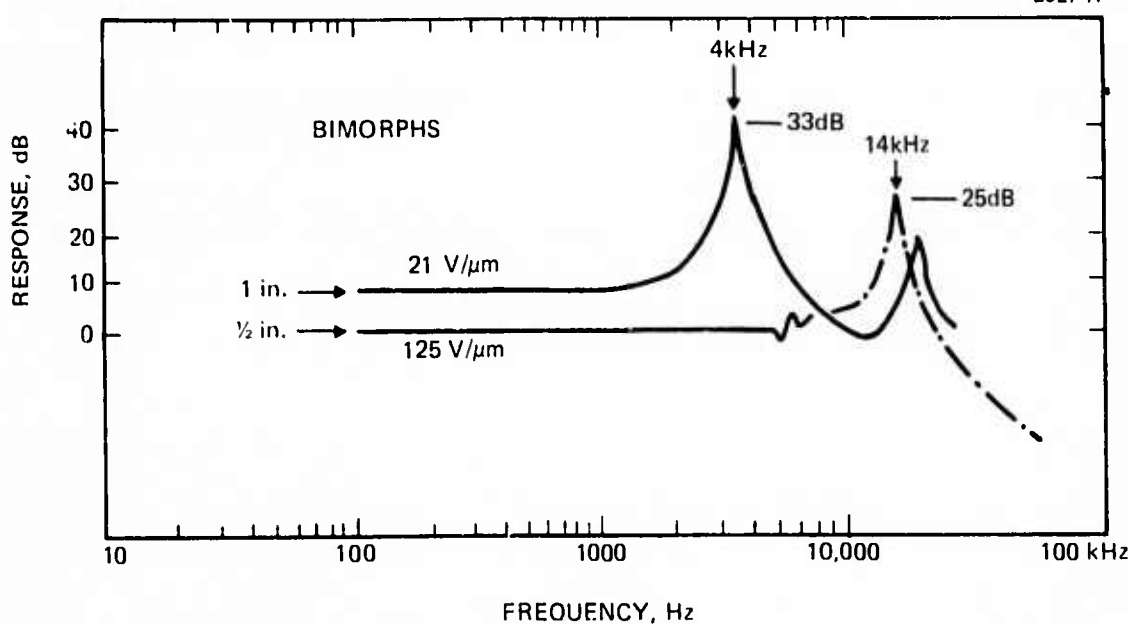


Fig. 32. Response of 1 in. and 1/2 in. bimorphs compared.

2521-20

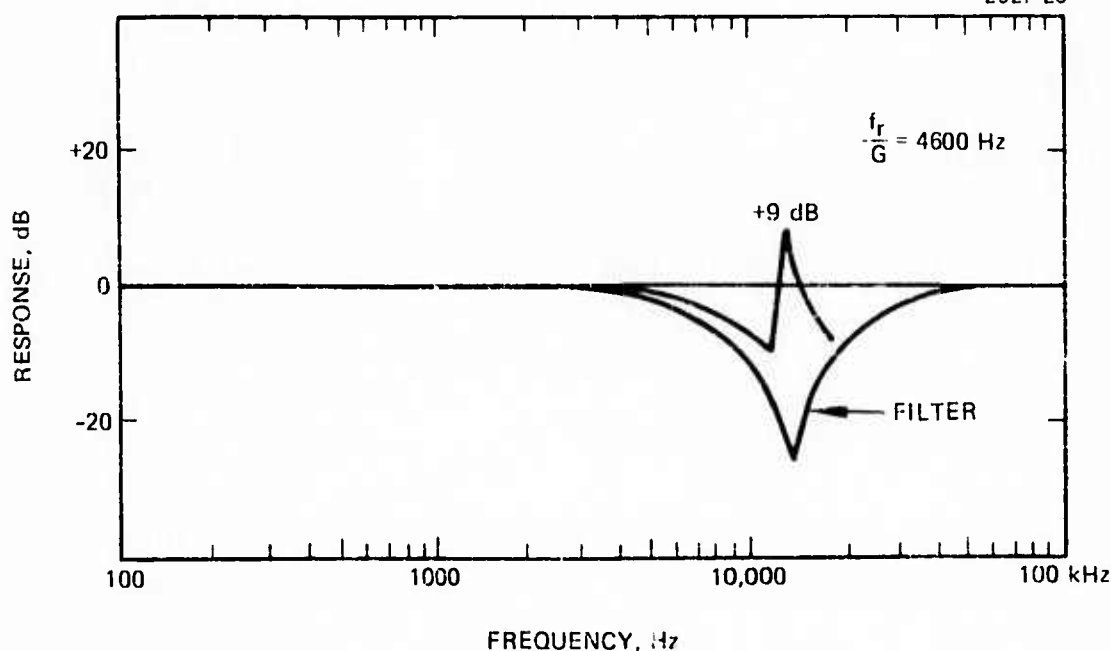


Fig. 33. A passive notch filter with the characteristic shown has been introduced to partially compensate the bimorph resonance. The resulting response curve is also shown.

the same available drive voltage, a sensitivity of  $2400 \text{ V}/\mu\text{m}$  is required. The resonant frequency of the device should be well above the operating frequency, but since the tagger is not operated in a closed loop servo system, stability is not a consideration. It is thus only necessary to find a piezoelectric with the required sensitivity and a resonant frequency above the highest dither frequency.

The dither frequencies have been chosen to maintain a minimum spacing of approximately 1 kHz, and to all fall within a single octave, to minimize the effects of harmonics. Since orthogonal (sine/cosine) operation is planned, nine frequencies are required. These two conditions can be met by 1 kHz spaced frequencies between 10 and 18 kHz inclusive, with a 10th frequency of 19 kHz available before the octave is exceeded. The resonant frequency of the tagger should be greater than 20 kHz to allow operation at those frequencies, or to allow the slightly larger range required if logarithmic spacings are chosen.

#### 4. Tagger Configuration

Since the sensitivity requirement is easily met, a single piece of piezoelectric material, rather than a bimorph, is sufficient for this application. A 1 in. long, 1/2 in. diameter, 1/8 in. wall cylinder of PZT-5H was procured and tested in two mounts as shown in Fig. 34. The mounting shown on the left, although more sensitive, coupled energy into the mounting structure and caused interference with mount resonances. The tubular transducer was remounted in the center as shown in the figure. This cylinder is now supported at a mechanical node, and thus there should be no energy coupled into the mount. The measured sensitivity was  $1300 \text{ V}/\mu\text{m}$ , and the first resonance occurred at 40 kHz with 3/8 in. diameter mirrors at both ends. A resonant frequency of 60 kHz was obtained using a similar cylinder of PZT-4. PZT-5H has different mechanical properties, hence the lowered resonance.

2521-9

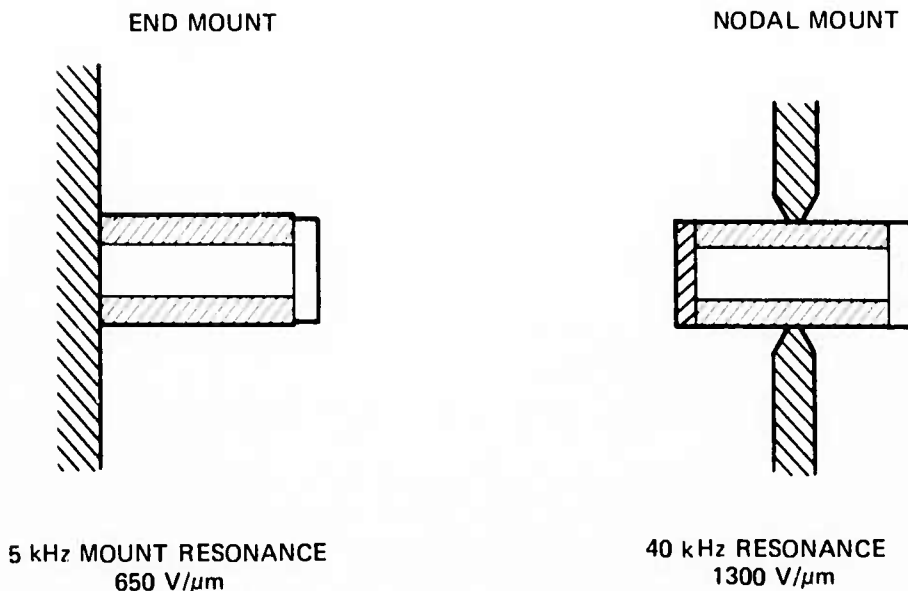


Fig. 34. Tagger configurations.

### C. Electronic Design

Figure 35 is a block diagram representing the 18-element experimental COAT system. The electronic portion of this system is comprised of the receiver, signal conditioning, and servo electronics array. The transducers that comprise the tagger and phase shifter array have been discussed in subsection III-B. The various mechanical and optical portions of the system are described in subsection III-D.

The electronics will be discussed in two groups: the receiver and signal conditioning, of which there is but one unit, and the servo electronics array, which is replicated eighteen times.

#### 1. 7-Element System

The 7-element system described in our proposal was used as a basis for design of the 18-element electronics. Limitations on the seven-element system included inadequate gain margin, inadequate test facilities, no provisions for sample and hold operation, no provision for DC offset compensation, and a drift-prone approach to phase shifter reset that was never fully tested. The new design has addressed all these problems. To improve gain margin, the single most serious limitation on the 7-element system, automatic gain control (AGC) was added to the received signal, the loop filter design was changed, and, most significantly, the phase shifter characteristics were improved, as discussed previously. The remainder of the improvements are concerned with detailed circuit design, and will be discussed briefly.

For development of the electronics, a single-channel system shown in Fig. 36 was assembled. The optical portion of this test system consists of a rigid interferometer with very short optical paths to reduce atmospheric interference with system operation. A photograph of this interferometer is shown in Fig. 37.

#### 2. Signal Conditioning and Receiver

The receiver for the COAT system will consist of a photomultiplier tube preceded by a narrow band optical filter. Output current will be monitored and controlled manually by adjustment of the dynode string voltage.

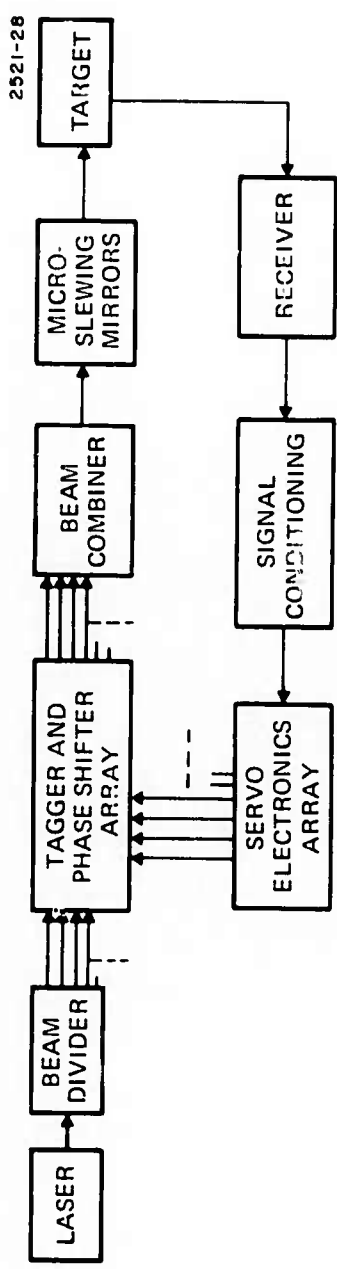


Fig. 35. 18-element system block diagram.

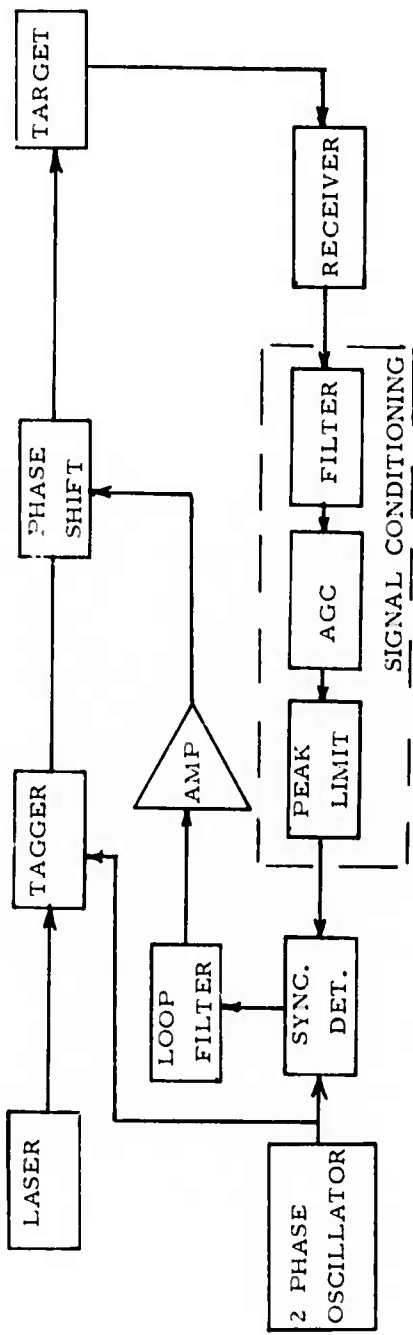


Fig. 36. Single channel test system.

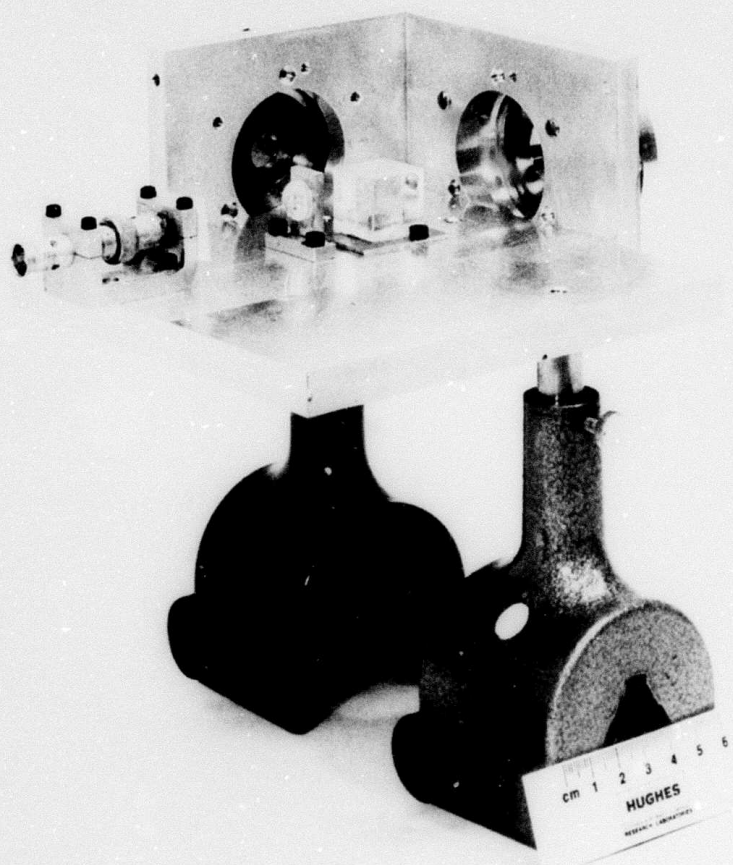


Fig 37 Single channel COAT test interferometer

Signal conditioning, shown in Fig. 36, consists of three functions: filtering, AGC, and peak limiting. The AGC function measures the average photomultiplier current and adjusts the gain of an electronic amplifier to maintain the DC response of the system constant. Figure 38 is a basic block diagram. A sample of the amplifier output is filtered to remove high frequency components, then used to control the amplifier gain. Characteristics of the low-pass filter determine the frequency response of the AGC amplifier, thus performing the filtering function of the signal conditioning subsystem.

The simple system depicted in Fig. 38 suffers from drift problems in the high gain dc amplifier. To overcome this, a 30 MHz upconversion system\* is used as shown in Fig. 39. The photomultiplier signal is used to modulate a 30 MHz carrier, which is then amplified in a conventional i. f. amplifier, then demodulated to recover the signal. The AGC function is instrumented within the i. f. amplifier.

A clipper is used after the i. f. to eliminate transient spikes that will come through the AGC system before it can respond.

Figure 40 shows the performance characteristics of the breadboard AGC/filter system. This system was designed with a 200 Hz response to allow use with the 7-element system; this will be modified to a 2 kHz response for use in the 18-element system.

Figure 41 is a photograph of the breadboard. A commercial i. f. strip is used, and the remaining circuitry is installed in well-shielded boxes to prevent RFI.

### 3. Servo Electronics Array

The servo electronics are comprised of the tagger oscillator and driver, the synchronous demodulator for recovering the error signal, the loop filter for establishing loop response, the driver amplifier for driving the phase shifter, and the sample-and-hold circuitry for slewing or offsetting the beam from the largest glint. Figure 42 is a block diagram of the electronics for these functions. There will be a total of 18 of these systems (except the oscillators).

---

\* Also sometimes referred to as "chopper stabilized". The chopping frequency is 30 MHz here.

2521-47

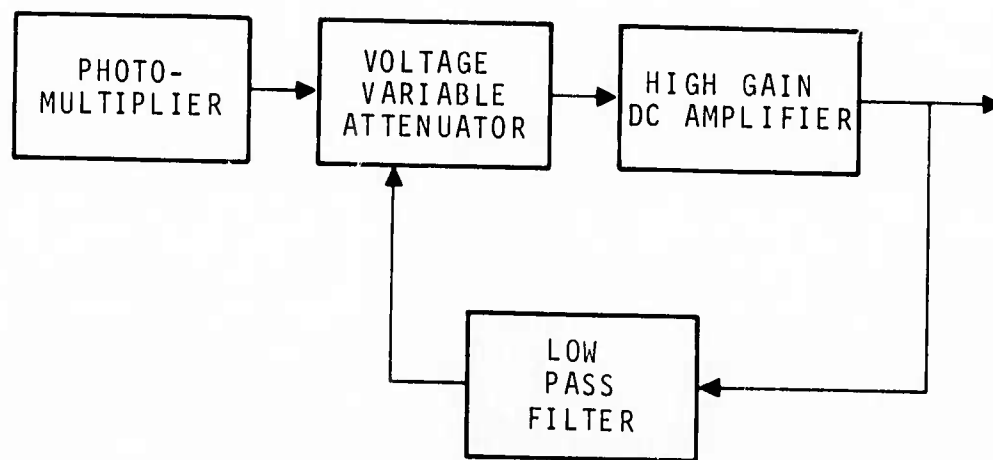


Fig. 38. Basic AGC system.

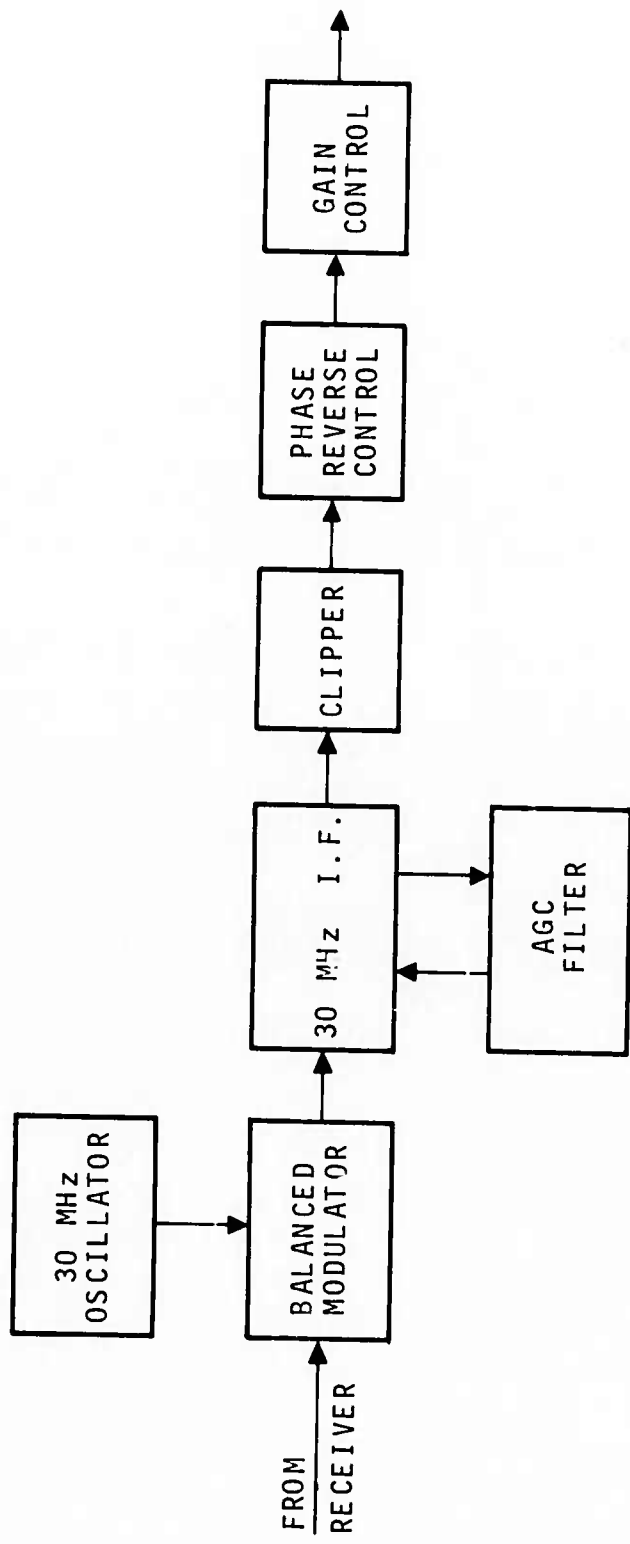
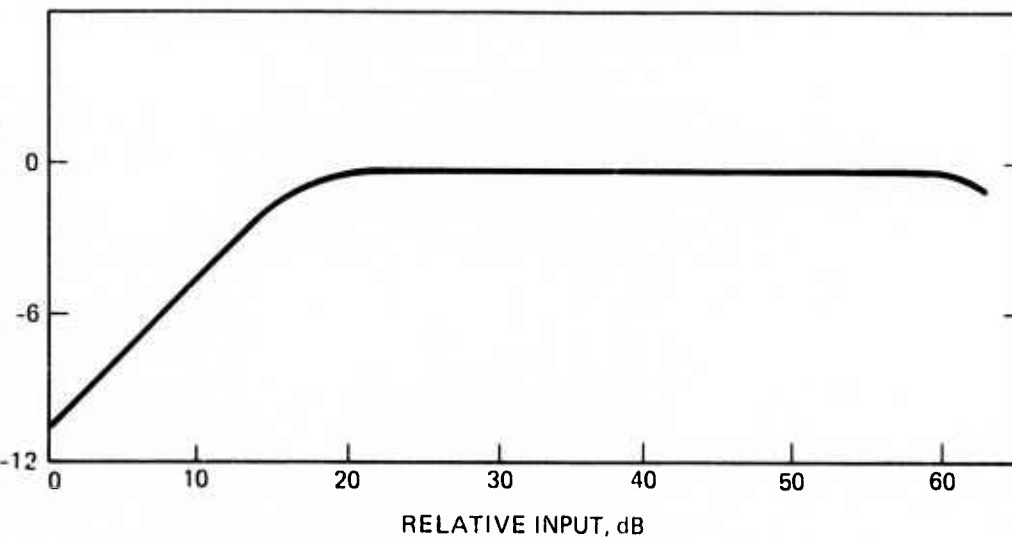


Fig. 39. Chopper stabilized or 30 MHz upconversion AGC.

2521-26

RELATIVE OUTPUT, dB



2521-27

RELATIVE OUTPUT, dB

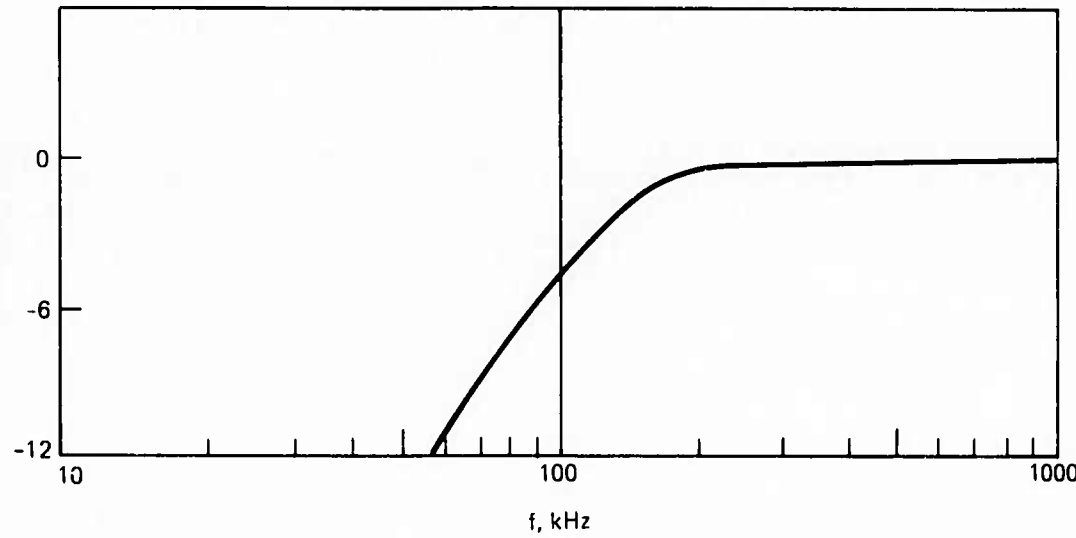


Fig. 40. Measured AGC performance.

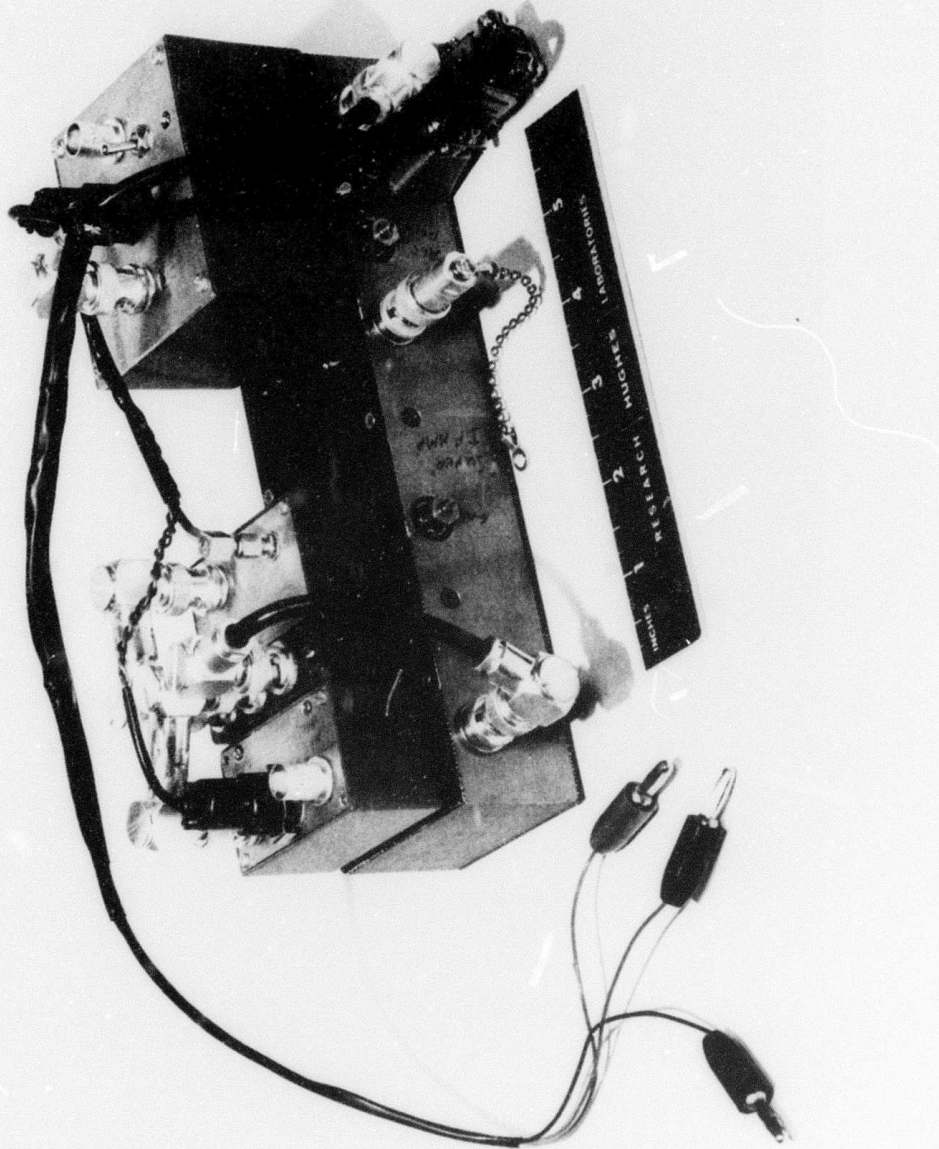


Fig 41 Breadboard 30 MHz upconversion AGC system

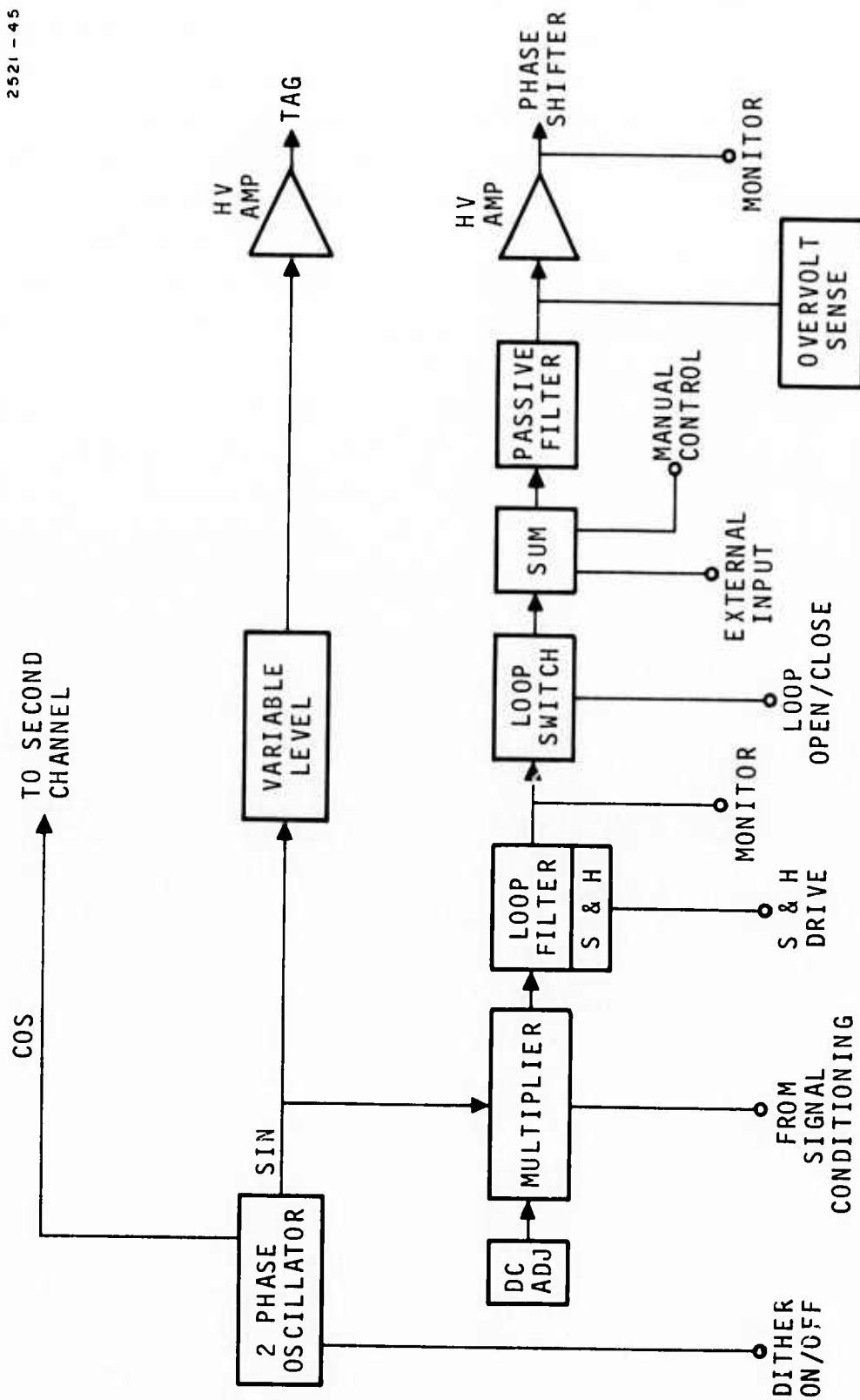


Fig. 42. Element electronics.

The tagging amplifier is a two-phase oscillator that maintains a stable frequency with low distortion. Each phase is used to drive a tagger through a high voltage driver. Both signals are also used as references for the synchronous detection process; only one of these channels is shown.

The synchronous detector is an integrated circuit 4-quadrant linear multiplier. This was chosen over the switching demodulator used in the 7-element electronics because the switching circuit is sensitive to odd harmonics of the dither frequency and also introduces switching transients into the system. A dc adjustment has been added to compensate for dc offsets throughout the amplifier chain.

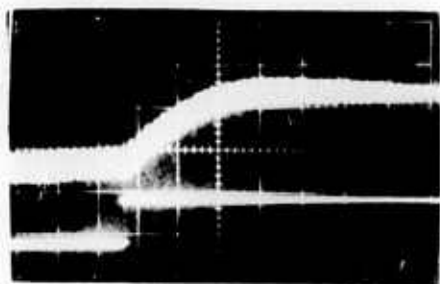
The loop filter has been modified to provide a lead-lag response in conjunction with a single pole lag. The resultant characteristic falls off initially at a faster rate than a 6 dB/octave network, but reverts to the unconditionally stable 6 dB/octave slope at higher frequencies. Care has been taken to select a network with good transient response; performance at the design gain of 27 dB is shown in Fig. 43. The filter provides higher gain margin for a given bandwidth than simple single- or double-pole filters.

The sample-and-hold circuit stores the correction voltage in the last filter capacitor and isolates the multiplier from the filter. A feedback path is provided to keep the filter charged to the sampled voltage to reduce the convergence time after the system is reactivated.

A summing amplifier is used to add a manual control voltage, an external drive signal, and a slewing signal to the error signal from the filter. In most instances, only one or two of these signals will occur at a given time. For example, a slew signal is added to the stored voltage during sample-and-hold operation to offset the beam from the converged position, as described in Section II-D.

The filter following the sum point is the notch filter used to compensate for the phase shifter resonance described in the previous Section. The high voltage driver is a 1022 high voltage operational amplifier capable of  $\pm 150$ V output.

The individual channel electronics will be built on printed circuit boards and mounted in appropriate relay rack size card cages. The signal conditioning electronics, sample-and-hold generator, offset controls, power



27 Db GAIN

Fig. 43. Measured breadboard transient response.

supplier, test equipment, target controls and data recording equipment will also be rack mounted to provide a convenient operator's console arrangement.

#### D. Overall Transmitter/Receiver Specifications

The overall COAT transmitter/receiver specifications have changed little from those listed in the proposal. Table VIII lists the major design choices. The argon ion laser was selected to assure us of adequate S/N while utilizing low transmission optical elements, small glints, etc. A coaxial receiver aperture larger than the transmitting array is used to assure proper field averaging; masks will be used to study the effects of smaller receiver apertures. The phase shifter chosen was described in Section III-B. The dither frequencies will lie in the octave 10 to 20 kHz. At the present time we plan to use approximately equally spaced dither frequencies with a 1 kHz spacing. Computer studies are now in progress to compare this choice with the alternative of using logarithmically spaced dithers in which each frequency is a factor (say 1.09) higher than the next lowest frequency. While such a spacing would require more bandwidth, the basic resonance of the PZT cylinders is at about 60 kHz, so that sufficient frequency range exists.

Provision is made in the control electronics for electronic phase scan and in the optical path for microslewing mirrors, so that both techniques can be employed.

The phasor matrix technique described in Section III-A is employed with up to 18 elements in two array arrangements: rectangular arrays of 3 mm x 3 mm elements on a 64 element, 8 x 8 grid; and axisymmetric arrays in a three-ring arrangement. A 1 x 8 rectangular array will be used for initial alignment and tests, with the 0-6-12 axisymmetric array used for most measurements. Pseudorandom arrays will be employed if time permits.

The output telescope will allow radiating aperture sizes of 6 mm to 48 mm by interchanging lenses. Figure 44 shows an overall layout of the transmitter/receiver components on a 3 x 8 honeycomb-core optical table. Drilled and tapped 1/4 in. - 20 holes on 1 in. centers allow a high degree of flexibility in locating components. The output from the argon ion laser first passes through a half-wave plate to rotate the plane of polarization so the E-vector is parallel to the table top, the desired entrance orientation for the phasor matrix Brewster plates. Next, a spatial filter is used to clean up the

laser mode. Two mirrors fold the beam into the phasor matrix; a removable beam splitter also provides a temporary beam for alignment purposes (dotted path). The output of the phasor matrix is sampled for the local convergence detector with a glass plate beam splitter. The beam passes on to two micro-slewing mirrors, a beam sizing telescope (1/4 to 2X), and finally it is reflected off a 45° mirror located on the axis of the receiving telescope. The target return is focussed on a photomultiplier located back-to-back with the 45° transmitting mirror.

TABLE VIII  
COAT Experiment Parameters

Laser	0.488 $\mu$ m, 1 Watt
Receiver	Photomultiplier
Receiver Aperture	17 cm Coaxial Plus Mask Option
Phase Shifters	PZT Bimorph Control; PZT Cylinder Dither
Dither Frequencies*	10, 11, . . . 18 kHz; Sine and Cosine
Beam Offset	Microslewing Mirrors and Phase Scan
Number of Elements	18
Arrangement	8 x 8 Rectangular Grid and 0-6-12 Axisymmetric
Array Size	24 x 24 mm (rectangular) available
Element Size	3 x 3 mm (rectangular)
Output Telescope	2X to 1/4X
Output Beam Size	48 mm to 6 mm

The system shown will be assembled and calibrated at Hughes Research Laboratories, Malibu, then transported to the Hughes Ground System Group at Fullerton for installation on range.

2521-25

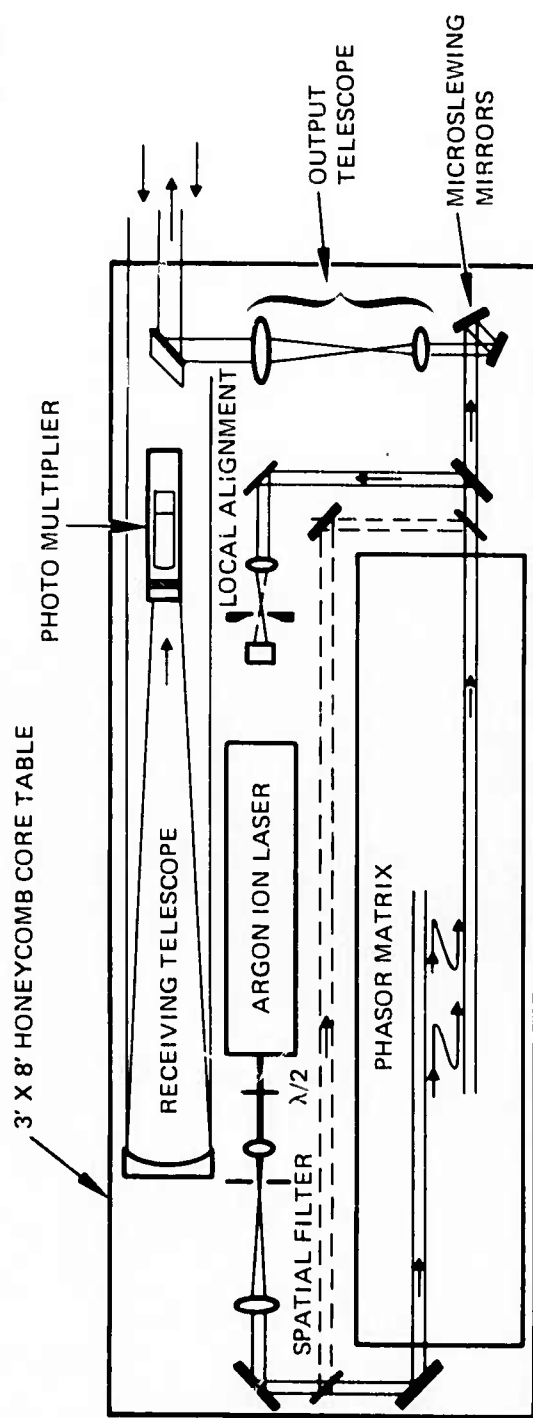


Fig. 44. Overall layout of COAT transmitter and receiver components  
on 3 ft x 8 ft flat optical table.

## E. Array Pattern Design

Several array configurations were analyzed to determine the possible utility of each in a measurements program which includes: (a) the need for an array with well-behaved and easily predicted characteristics for the purpose of debugging, verifying and calibrating the operation of the experimental apparatus; (b) the need for an array which is configurationally representative of operational systems to the extent that it is 2-dimensional and filled (with contiguous elements); (c) finally, the desire to have an array configuration which may be representative of operational systems wherein it would simulate the important characteristics of a full size matrix (e.g., 64 elements) pattern with only 18 elements.

A group of four array configurations were initially selected to meet these requirements. They are discussed in the order in which they would be used throughout the checkout and measurements program. They include the following:

1.  $1 \times 8$  linear contiguous array of square elements. This array will be used during the initial laboratory checkout, debugging and verification of the control system and optomechanical apparatus in one dimension. It provides a relatively large and convenient resolution field to work within the target plane. A  $1 \times 9$  array computer generated pattern is shown in Fig. 45. The extent of the low side lobe region between main lobe and grating lobe can be seen in Fig. 45 where the array has been phase-scanned in elevation. The nearest grating lobe is down by -10 dB (the C-contour) with the array scanned as shown, one-half grating lobe spacing off boresight.
2.  $4 \times 4$  square matrix of contiguous elements. This array was recommended for the same purpose as Fig. 45 except that it provides a 2-dimensional resolution. The computer-generated pattern for this array is given in Fig. 46. Note that the side lobe level in the region between main and grating lobes is higher, thus slightly complicating the target return.
3. Annular 0-6-12 (axisymmetric) array of contiguous elements. This array is recommended for use in making atmospheric path measurements because of its prospects for application to operational systems. All 18 channels in the experimental apparatus will be utilized for this configuration. The computer-generated pattern for this element configuration is given in Fig. 47 for both boresight, and phase-scanned conditions.



A

CONTOURS	
+	= 0 dB
A	= -3 dB
B	= -5 dB
C	= -10 dB
D	= -15 dB
E	= -20 dB
F	= -25 dB
X	= GEOMETRIC AXIS

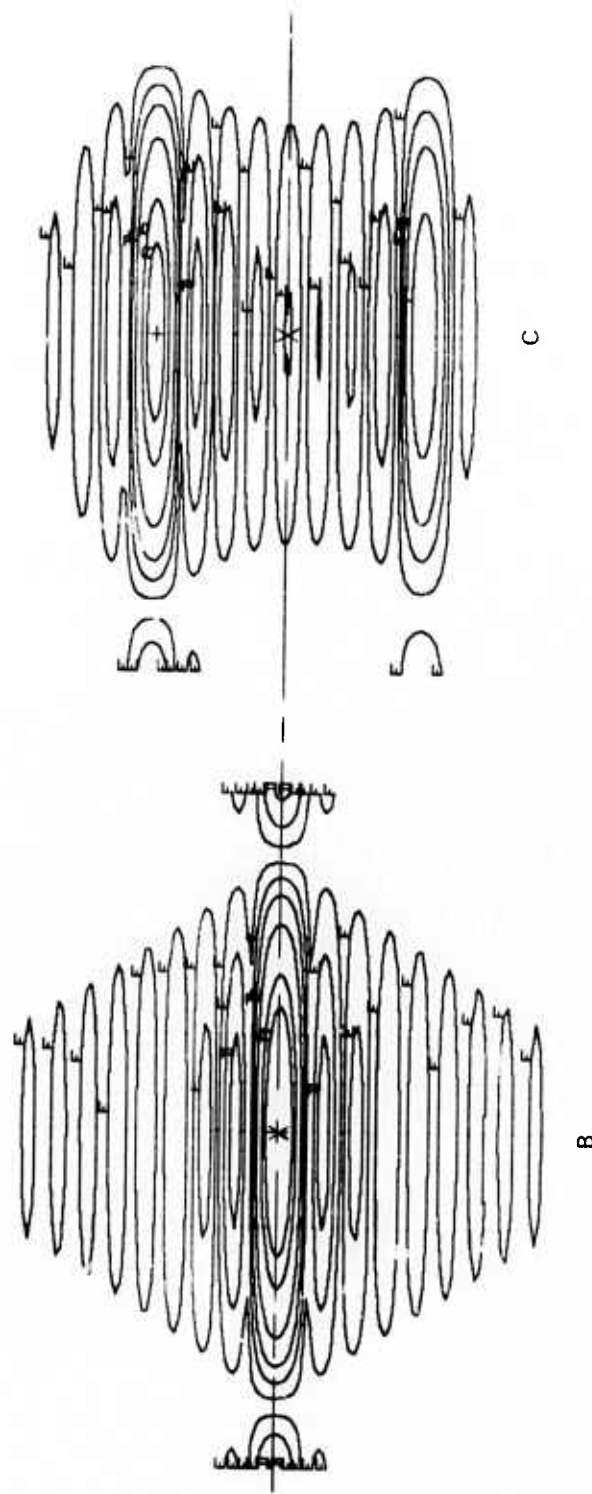


Fig. 45. Rectangular  $1 \times 9$  array. (A) Radiating element distribution. (B) Far-field pattern with array on bore sight. (C) Far-field pattern with array scanned off boresight vertically as shown.

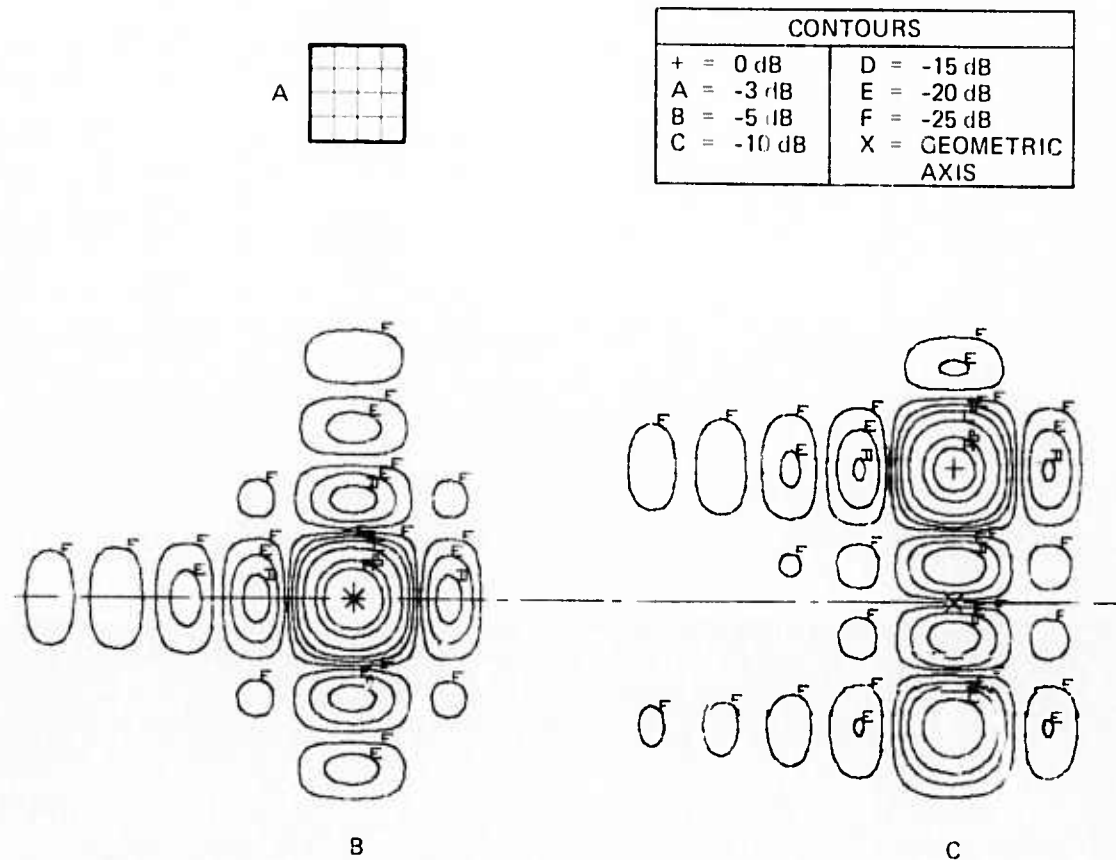
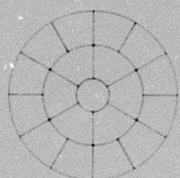


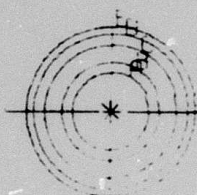
Fig. 46. Rectangular  $4 \times 4$  array. (A) Radiating element distribution. (B) Far-field pattern with array in boresight. (C) Far-field pattern with array scanned off boresight vertically as shown.



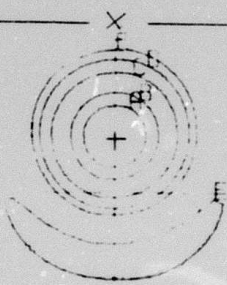
A

CONTOURS	
+	= 0 dB
A	= -3 dB
B	= -5 dB
C	= -10 dB
D	= -15 dB
E	= -20 dB
F	= -25 dB
X	= GEOMETRIC AXIS

BORESIGHT



B

BEAM  
SCAN  
DOWN

C

Fig. 47. Axisymmetric 0-6-12 array. (A) Radiating element distribution. (B) Far-field pattern with array on boresight. (C) Far-field pattern with array scanned off boresight vertically as shown.

4. Sixteen square elements randomly thinned onto 8 x 8 matrix. This configuration was also recommended for use in obtaining measurements through atmosphere. It produces a more complex far-field pattern, but offers the advantage of 2-dimensional operation with a resolution equivalent to that of a filled 8 x 8 matrix array. Figure 48 shows the computer-generated bore-sight and phase-scanned off-boresight patterns. The bore-sight pattern contains side lobes which are approximately 16 dB down in intensity from the main lobe. This would tend to place some restrictions on the relative glint strengths which can be used.

As a result of the recommendations of the RADC Project Engineer given at the time of the Design Review, the order of priority in implementing these arrays will be 1, 3, and 4. The 1 x 8 rectangular and 0-6-12 axisymmetric arrays will be fabricated and used for checkout and the majority of the on-range measurements. The pseudorandom 18 element 8 x 8 array will be implemented if time permits. The 4 x 4 array will not be implemented.

#### F. Range Design

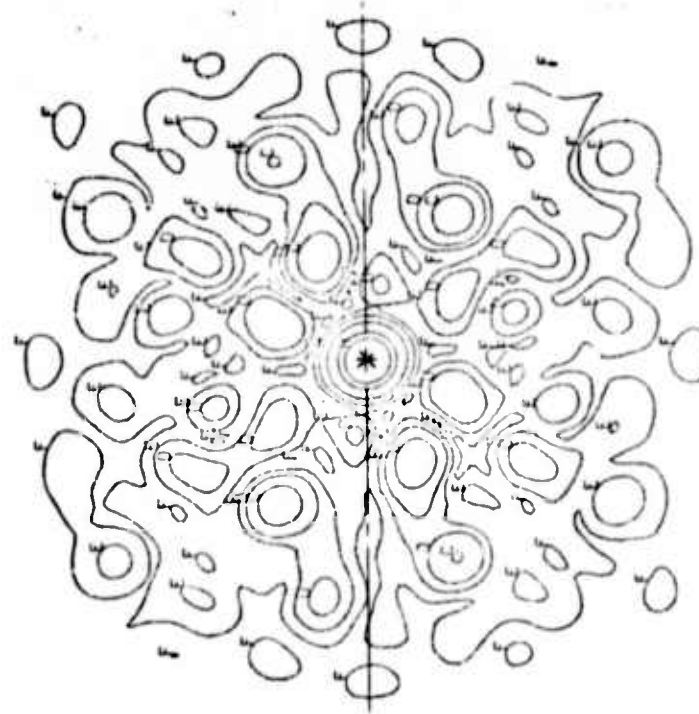
The propagation range to be used during the atmospheric measurements phase of the program consists of a 94-meter-long segment over a flat horizontal rock-on-asphalt roof terminating at the target area. The beam is conducted from the ground-floor laboratory containing the COAT system up 15 meters to the roof-top path via a periscope. Photographs of the range and target area were given in the proposal. Experiments were conducted during this quarter to characterize the path with the following objectives in mind:

1. It was necessary to determine the range of turbulence conditions available over the path as a function of time of day, weather, and height above the roof surface. Given these data, the COAT system transmitting aperture and element sizes could be determined along with path height for best match to the turbulence structure.
2. A determination was needed as to whether a match of aperture to turbulence was better accomplished by fixing the aperture and adjusting the path height or by fixing the path height and adjusting the aperture, or by fixing both and waiting for daily changes.
3. It was imperative that the several methods for determining  $C_n^2$  be compared and correlated.

6-2521-29

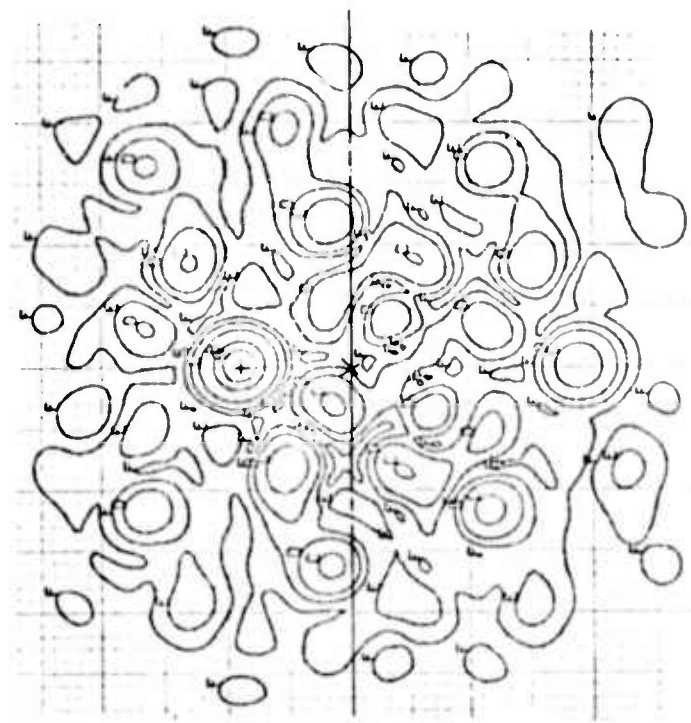
CONTOURS	
+	0 dB
A	-3 dB
B	-5 dB
C	-10 dB
D	-15 dB
E	-20 dB
F	-25 dB
G	GEOMETRIC AXIS

A



BORESIGHT - COMPUTED

B



SCANNED - COMPUTED

C

Fig. 48. Pseudo random 18-element array on  $8 \times 8$  grid. (A) Radiating element distribution. (B) Far-field pattern with array on boresight. (C) Far-field pattern with array scanned off-boresight vertically, as shown.

4. A determination was needed as to which method or methods should be used on-line during the measurements program.

Measurements were made to determine  $C_n^2$  by measuring thermal fluctuations using a differential fast response microthermal probe-pair at one location, and by measuring the optical MTF from resolution bar chart photographs taken over the entire path. A third technique is being prepared wherein a helium-neon laser scintillometer beam will be sent over the same path as the COAT system.

The microthermal measurements employed probe designs and electronic circuit designs originally worked out by Ochs and Lawrence at N. O. A. A., Boulder, Colorado, which are now well-accepted throughout the atmospheric optics community. One such instrument was made at the Hughes Ground Systems Group, and was used on the 94-m range for a series of measurements. Over several weeks of data taking, turbulence conditions ranged from  $5 \times 10^{-17} \text{ cm}^{-2/3}$  (after a rain) to  $4 \times 10^{-14} \text{ cm}^{-2/3}$  (sunny day). Although turbulence was found to vary as a function of height above the roof, this will probably not be a reliable means of path turbulence adjustment. Turbulent mixing is not complete within the first 40 to 50 cm above the roof as it is at 80 cm or greater. We suspect that laminar horizontal layers exist which cause gross beam steering effects. A path height of 100 cm (fixed) was therefore chosen for the COAT experiments.

Recordings of the unsmoothed rms output of the thermal probe bridge are shown in Fig. 49. This output must be integrated for intervals of 100 sec or more before meaningful values of  $C_n^2$  are obtained, but the raw data give some indication of the time variation and magnitude of the fluctuations observed. Traces for both relatively quiet conditions and relatively turbulent conditions are shown.

A second dual-probe instrument of similar design was fabricated at Hughes Research Laboratories and will be employed during the next quarter to cross check the calibration of the first instrument. It will then be installed on the test range to provide a second monitoring point.

A helium-neon laser scintillometer, also of a design used by Ochs, is being fabricated at HRL and will be ready soon for cross comparisons with both thermal probe instruments. This instrument should agree within 20%

2521-48

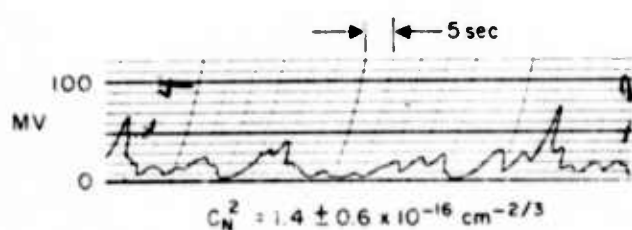
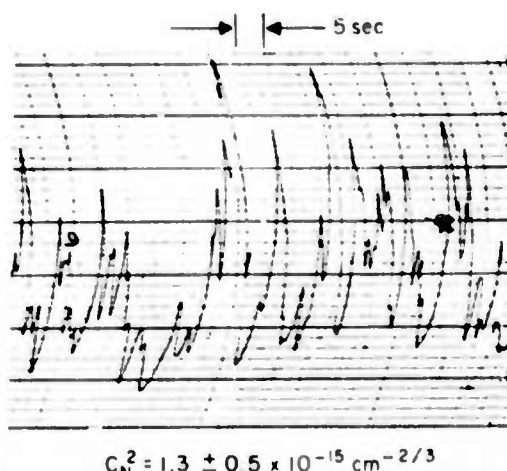
9 JUNE 1973  
0910 hrII JUNE 1973  
1320 hr

Fig. 49. Recordings of the dual temperature probe bridge rms output for low and moderate turbulence conditions. The value of  $C_n^2$  given are for 100 sec average of the strip chart output mode with a planimeter. The two probes were located at the midpoint of the 94 meter path, 78 cm above the roof.

or so for relatively low values of turbulence over our 94-m range (according to Ochs - Private communication). For the higher values of turbulence, optical path saturation will limit the usefulness of the scintillometer data, and we will have to rely on the microthermal measurements.

To date, the results of the photographic MTF measurements using the technique described in the proposal have not agreed satisfactorily with the microthermal measurements; the MTF measurements have yielded substantially higher values of  $C_n^2$ . These MTF measurements were made with a 0.1 sec exposure time during the 100-sec microthermal averaging time, and thus may have seen uncharacteristic samples. While we do not expect perfect agreement between two such diverse measurement techniques, we should have better agreement than the present order-of-magnitude. We will continue to try to reconcile these measurements during the next quarter.

#### G. Target Design

##### 1. Glint Design

Several types of targets have been looked at and tried on one of the present operating COAT systems. These include corner cubes, Scotchlite, and ball bearings; but none were able to meet fully the requirements imposed by our planned measurements program. The target glints must be stable, reliable, repeatably adjustable in intensity, be relatively insensitive to orientation or slight variations in geometry. These glints must measure power incident on them, and they must be able to be closely spaced with other glints. Finally, the glint entrance aperture must be small compared to the smallest expected array pattern main lobe over the 109-m path from 4 cm optics.

A variation of the "cat's eye" reflector was considered and accepted on the basis of the results of a series of glint return spatial distribution experiments. A cat's eye reflector consists of a reflecting surface positioned at the focal plane of an input lens. Changes in angle of the incident light are translated by this lens into changes in position on the reflector, thus making the reflection angularly independent. The reflectivity of an experimental cat's eye was measured as a function of the reflecting surface position with respect to the focal plane of an f/2 microscope objective. The results are

given in Figs. 50 and 51 for diffuse and mirrored surfaces, respectively. It can be seen that the paper target was highly scintillating (spatially not temporally) compared to the mirror, but the paper was extremely insensitive to internal orientation whereas the mirror was. It was found that the requirement to have a glint return which is uniform over approximately a  $3^{\circ}$  field was easily satisfied along with a 20 dB intensity adjustment.

We feel that sufficient internal alignment accuracy can be maintained to use a mirrored reflection in the cat's eye. The resulting glint configuration is shown in Fig. 52. The arrangement consists of a multilayer dielectric mirror mounted on a fine thread drive and positionable about the focal plane of an f/2 microscope objective. The mirror is made partially transmitting so that 1% of the incoming light is collected by a photodetector located behind the mirror and is subsequently recorded as glint power. In order to accommodate the placement of two glints contiguously, a small prism or folding mirror is placed as shown in the figure.

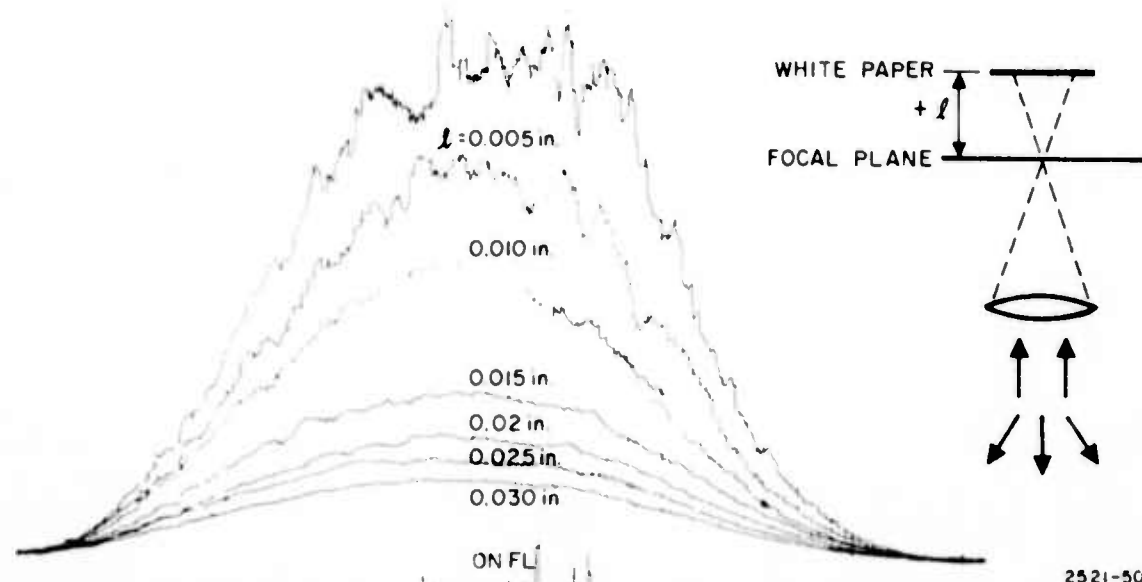
An earlier version of a cat's eye reflector which utilized a beam splitter to sample the incident beam was considered but rejected because of the polarization sensitivity of the sampling fraction to rotation.

## 2. Target System Layout

The glint structures described above can be used alone for single-glint tests or with others for multi-glint tests. A three-glint configuration is shown in Fig. 53. Each of the three glints is held onto a circular base by a radially adjustable mount with 5-cm travel. The 3-glint apparatus is shown as viewed by the COAT transmitter. There are no intervening optical elements along this path during static target measurements.

The apparatus is modified for dynamic target tests by including two flat folding mirrors in the manner shown in Fig. 54. The apparent glint position is moved up to 10 mrad./sec by tilting the mirror on the right along two orthogonal axes. The motion of the target as viewed by the COAT transmitter is virtual, but it nevertheless accurately portrays real target motion and atmospheric effects provided the path from the glint to the scanning mirror is short.

2521-49



2521-50

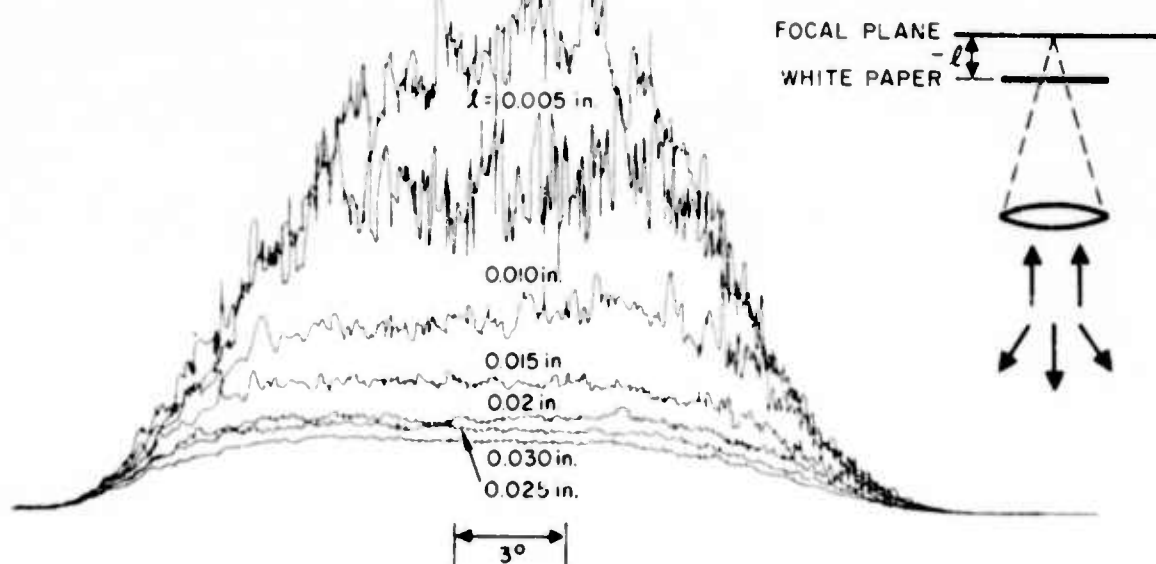


Fig. 50. Glint return spatial distribution measurements - diffuse reflector (white paper).

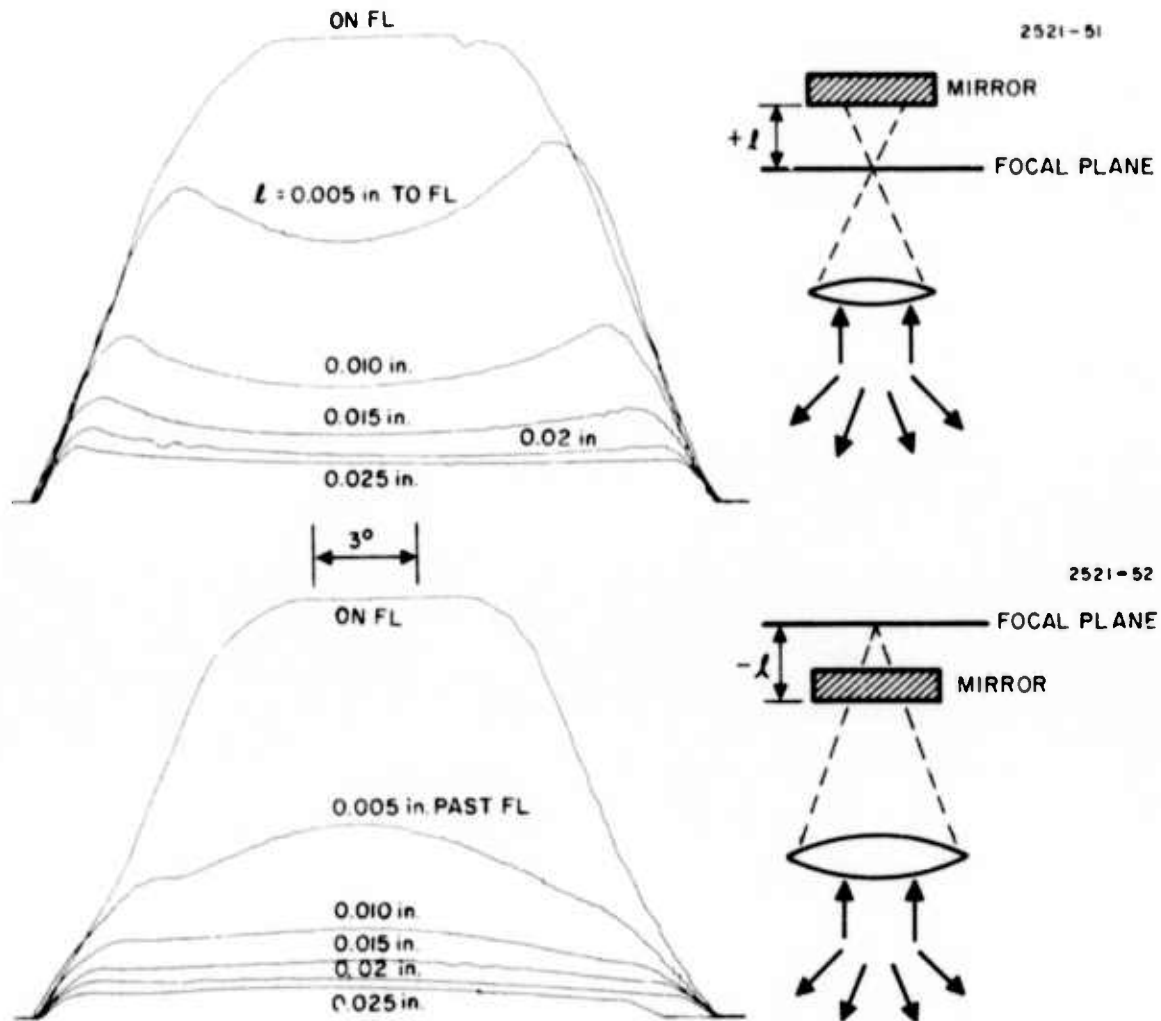


Fig. 51. Glint return spatial distribution measurements — mirrored reflector.

2521 37

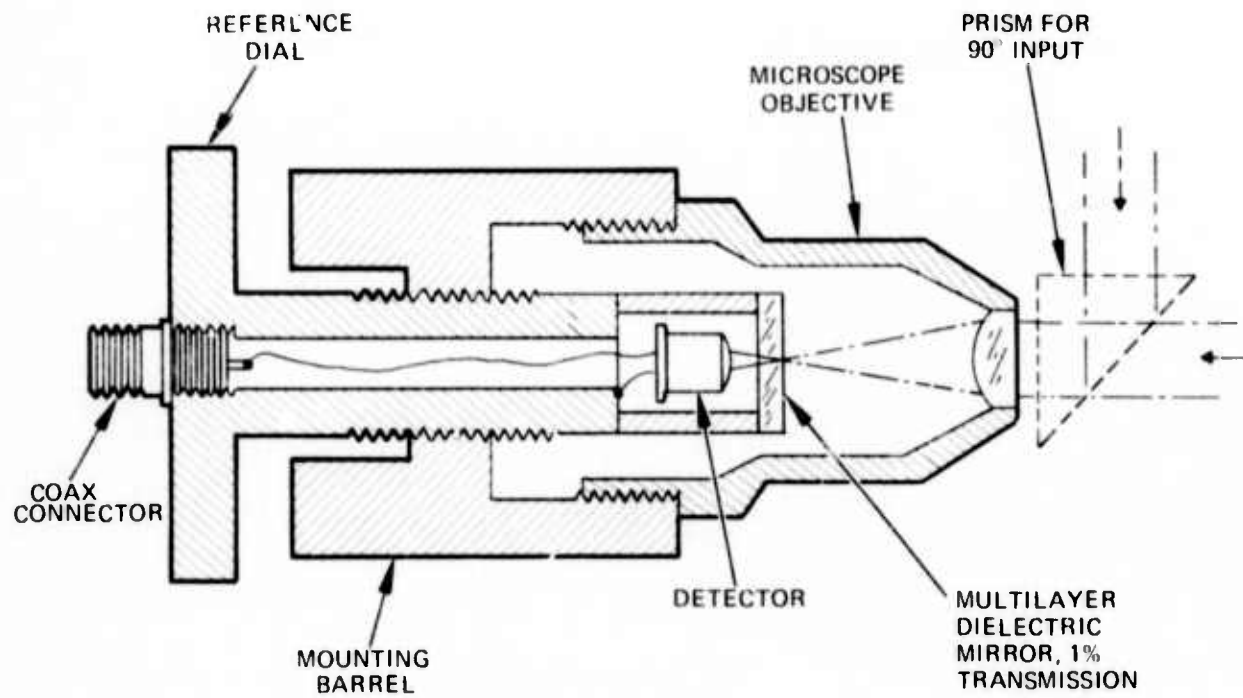


Fig. 52. Schematic cross-section of cat's eye glint using a multilayer dielectric mirror with a detector.

2521-38

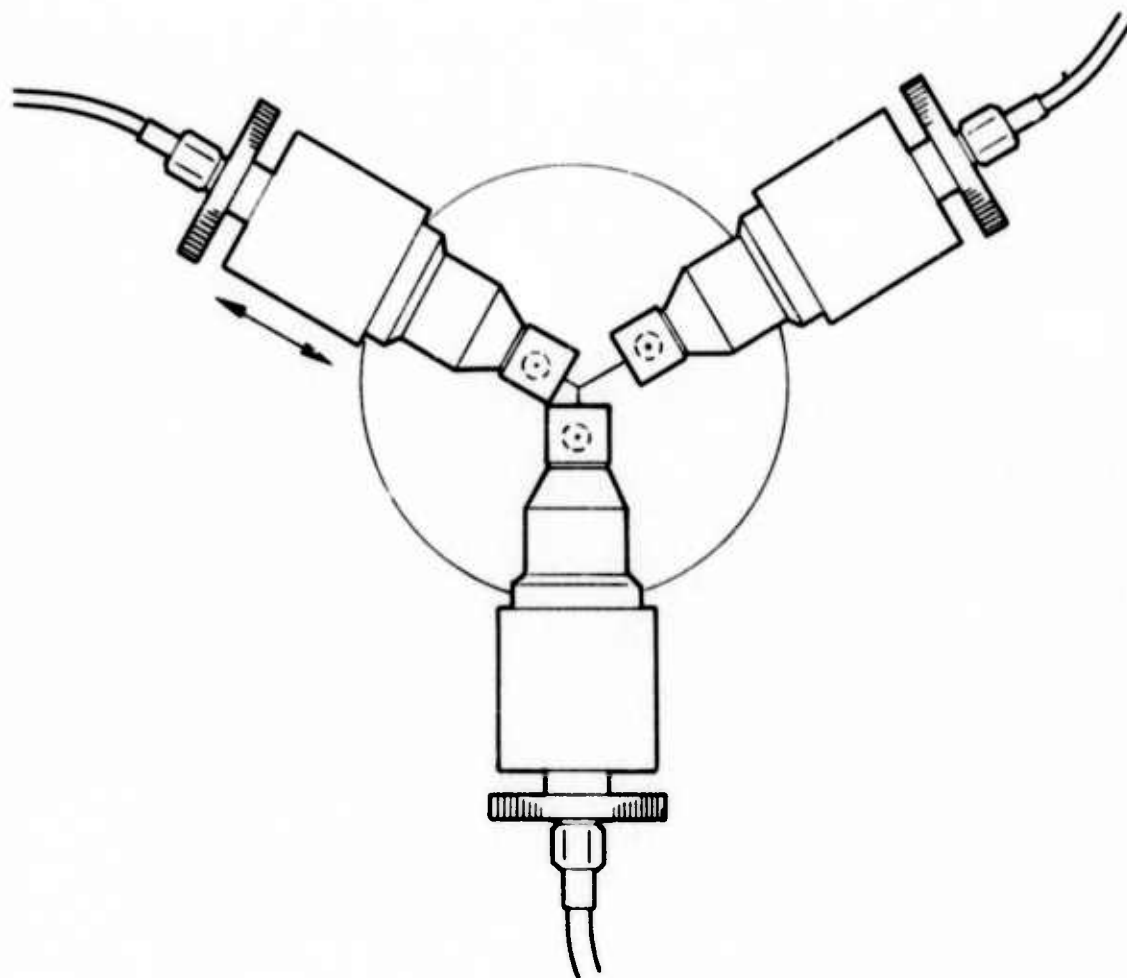


Fig. 53. Three-glint mounting for multi-glint target.

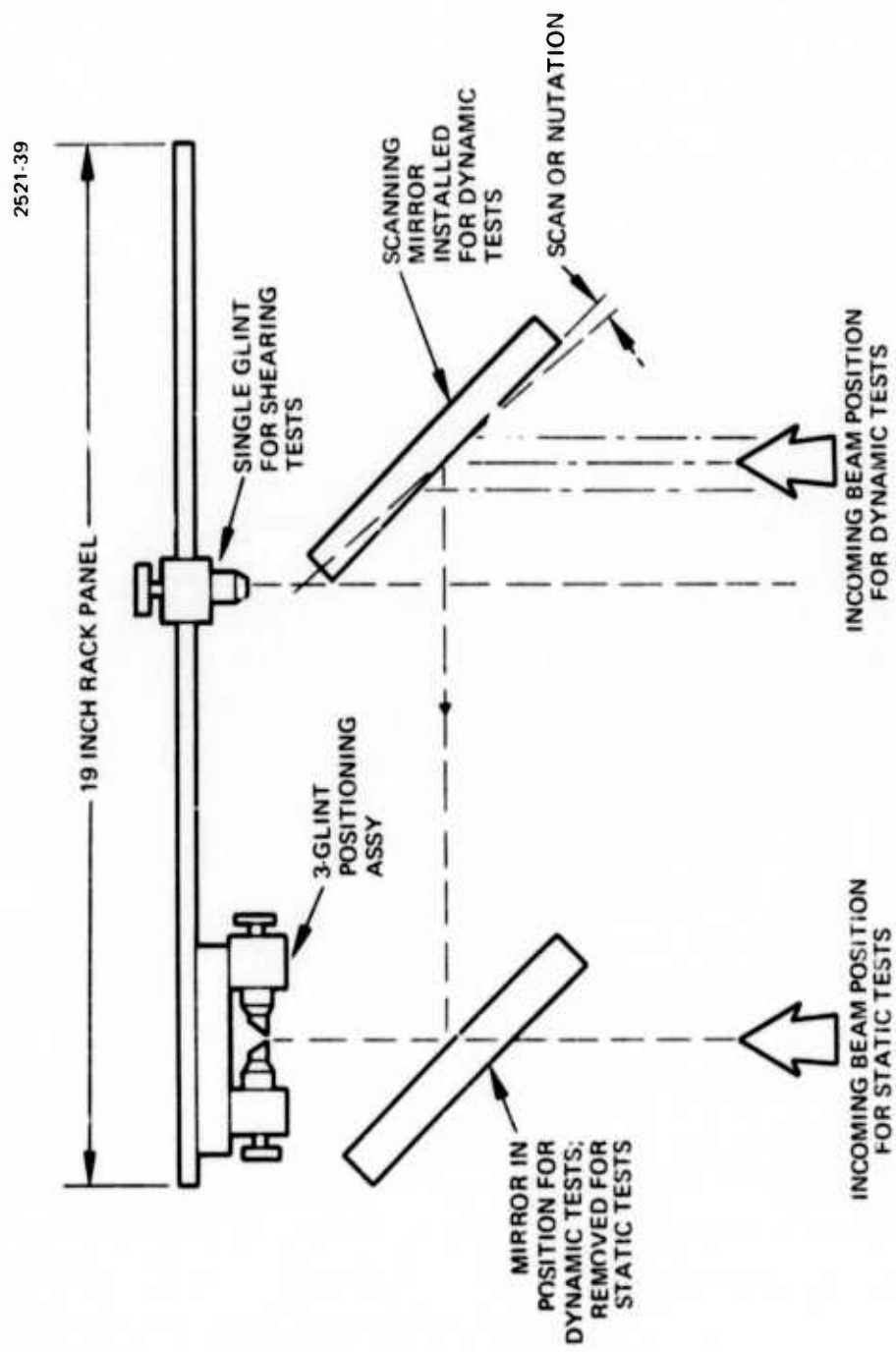


Fig. 54. Overall target configuration.

A stationary single glint can also be positioned near the edge of the nodding mirror (as viewed by the COAT system). Thus even more complex glint patterns, with changing intraglint distances can be produced. The entire glint target is mounted on a 19-in. relay rack and integrated with the date recording instrumentation as described in the next section.

#### H. Instrumentation

Instrumentation will be required to monitor all essential parameters, in real time during all convergence and tracking experiments in four basic areas. These are: (1) Target plane beam spatial intensity distribution; (2) Propagation path characteristics and meteorological conditions; (3) Target geometry and glint power; (4) Control system behavior. Figure 55 summarizes the general layout of the resultant instrumentation. We have found from previous work that television video tape recording of target plane beam spatial characteristics is a very convenient technique, one that is amenable to subsequent analysis, but it does have some drawbacks. First, intensity information although available via A-scope presentation line-by-line, is not readily interpretable from a conventional monitor display. Second, the standard television format frame rate of 1/60 of a second is not sufficient to record the temporal fine structure changes taking place during the convergence process.

Our solution to the problem of displaying intensity contour maps of the beam is to introduce an amplitude quantizer in the Vidicon output and drive a color monitor with three three-color composite signal. The result will be a color-contoured display in which areas of constant color are areas of equal intensity.

Our solution to the frame rate limitations is to add a high speed motion picture camera to the instrumentation package. The camera which is presently available as Hughes test equipment is capable of 11,000 fps and has a 200 ft loading capacity. A 6000 fps rate is considered necessary to record the motion taking place during the worst-case tests (those which include 10 mr/s track rates on single glints). Because of the high film footage rate this camera will be used only during selected tests where it is necessary to examine the high speed details. Figures 56 and 57 show the layout of the television camera and motion picture camera with respect to the glint simulator.

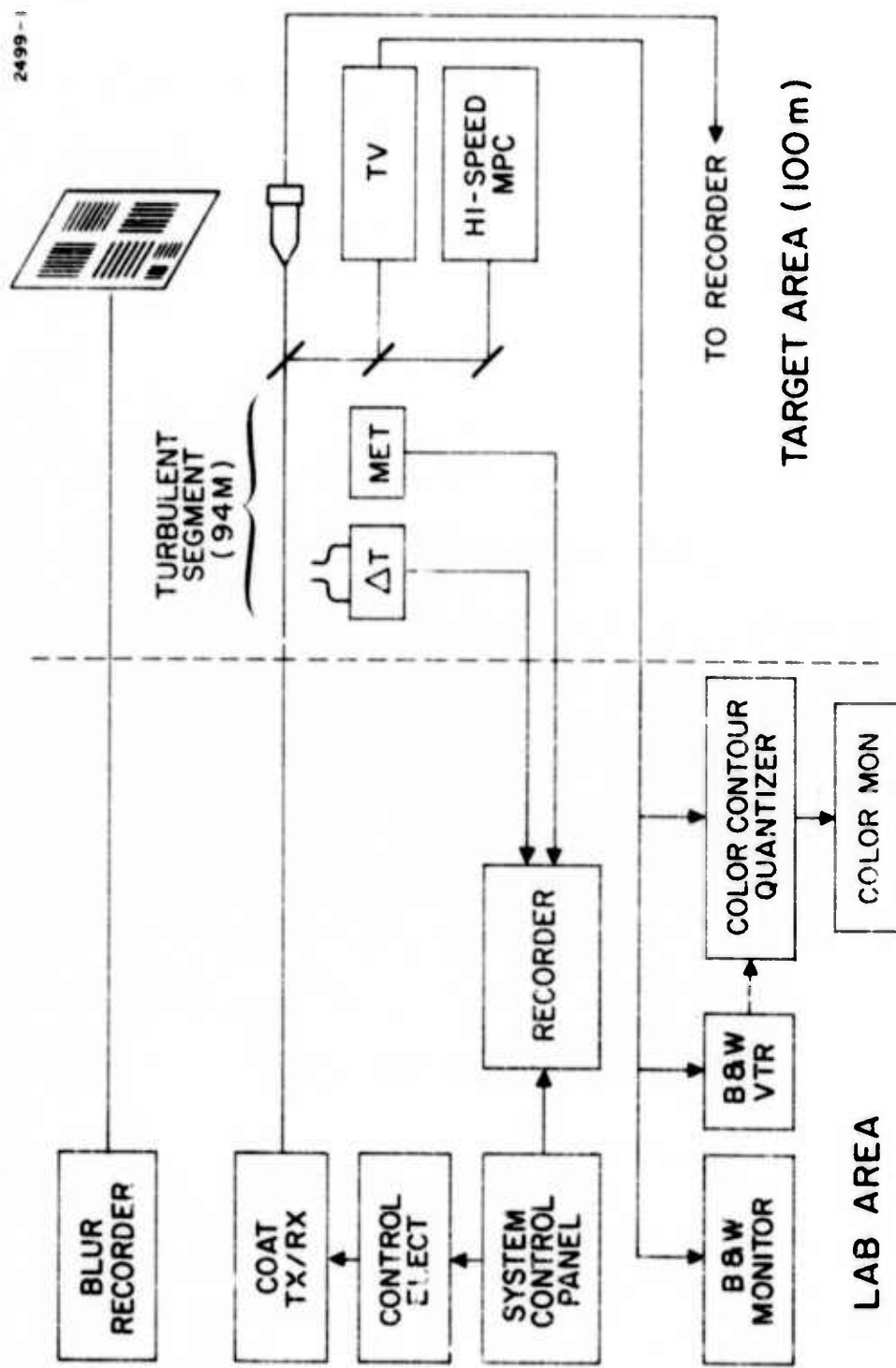


Fig. 55. Instrumentation and recording system.

2521 41

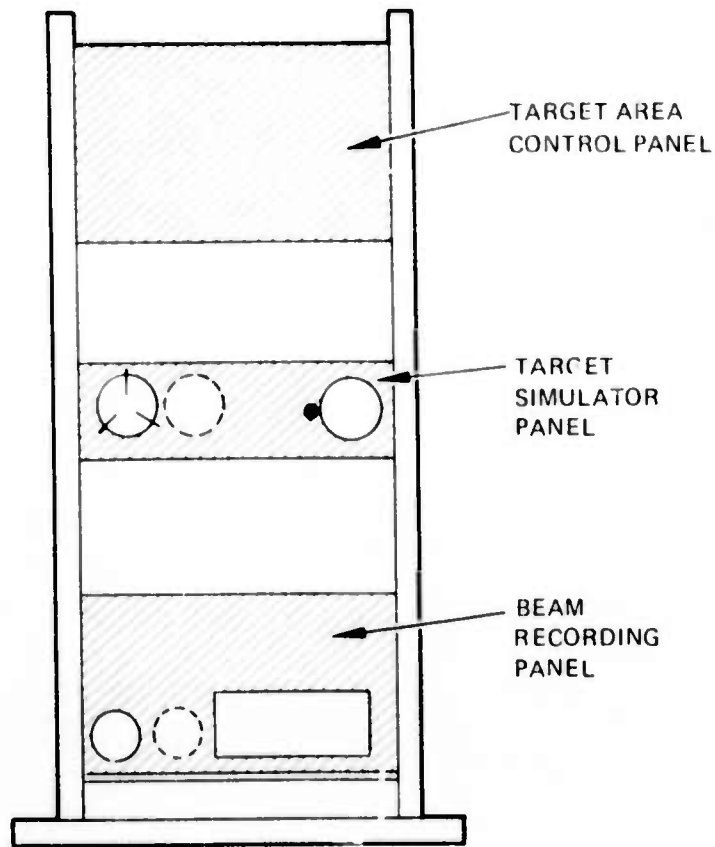


Fig. 56. Target simulator and diagnostic sensors.

2521-40

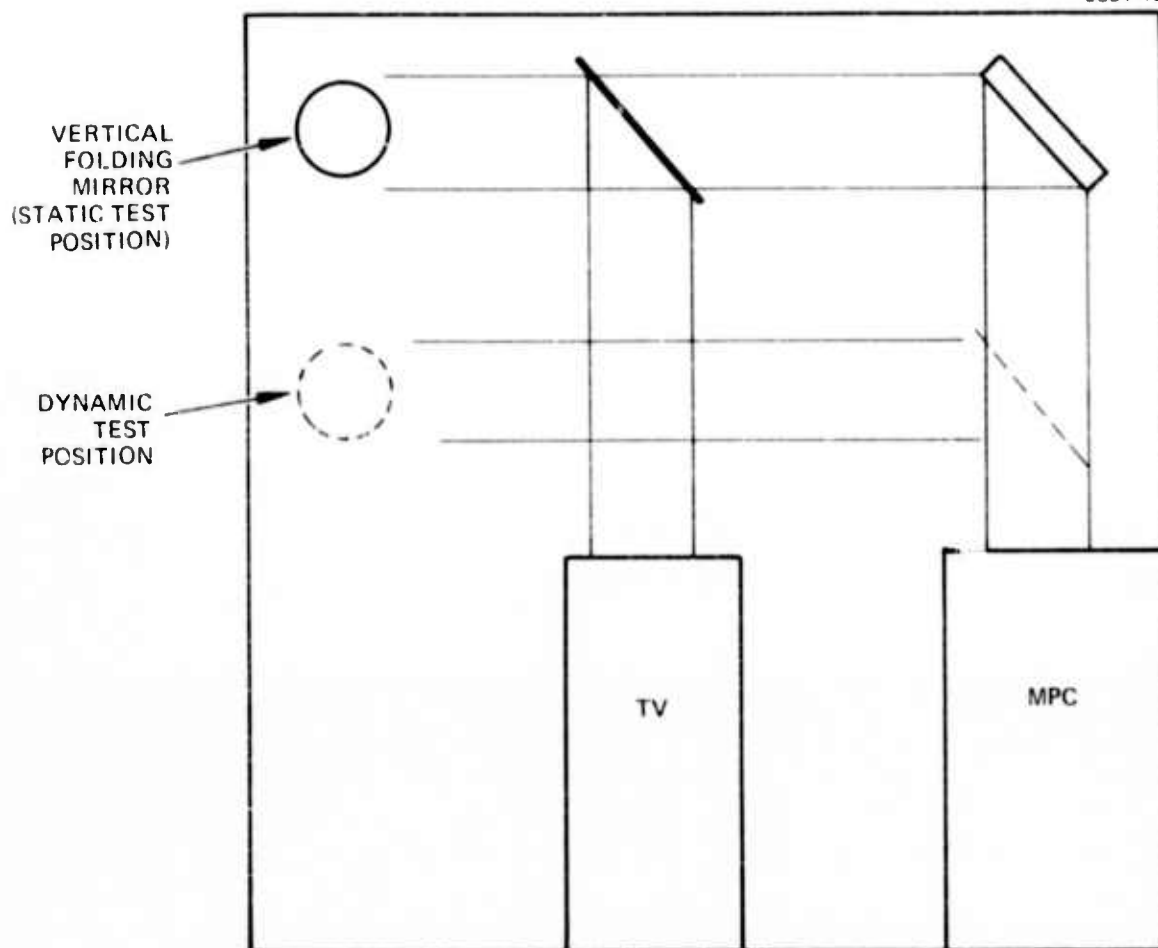


Fig. 57. Target plane beam recording panel.

Glint power will be measured using a photodetector within the glint itself, as described in the previous section. The output will be recorded in two places. Oscilloscope and strip chart recordings will be made and retained for detailed analysis. In addition, a length-modulated line will be superimposed onto the television video for each glint.

Propagation path characteristics will be monitored and recorded continuously during all experiments. Optical MTF will be recorded photographically once per data run. The  $\Delta T$  sensors and the scintillometer will be operated continuously and recorded in strip-chart form both in fast response form and in 100 sec integrated form.

## SECTION IV

### MEASUREMENTS PROGRAM

According to the schedule given in Fig. 1, the COAT system will be ready in October for approximately one month of calibration tests, followed by 5 months of on-range measurements. The exact procedure for performing the calibration and on-range measurements will actually be developed during the next quarter, but we can give a listing of the quantities that must be measured both for calibration and for system performance. These are given in a sequence of tables.

#### A. Calibration Measurements

Tables IX, X, and XI list the optical, temporal and subsystems calibration measurements that will be made. The accuracy of the optical beam profile and distributions listed in Table IX will be sufficient for comparison with the computer runs and comparison with the system performance on-range.

#### B. On-Range Measurements

Tables XII, XIII, XIV, and XV and the sketches therein indicate the general nature of the measurements that will be made on-range. Most of these measurements will also have been performed as part of the calibration runs to exercise both the COAT system and the target. The actual number of runs and their exact scheduling will depend to some extent on the availability of suitable atmospheric conditions. Fortunately, the winter months in Southern California should yield a wide variety of turbulence conditions.

TABLE IX  
COAT System Calibration - Optical

2521-53

- Near- and Far-Field Intensity Profiles for Each Element
- Total Power Out of Each Element
- Alignment Stability for Each Element
- Converged Beam Distribution for Full Array for Each Array Variation

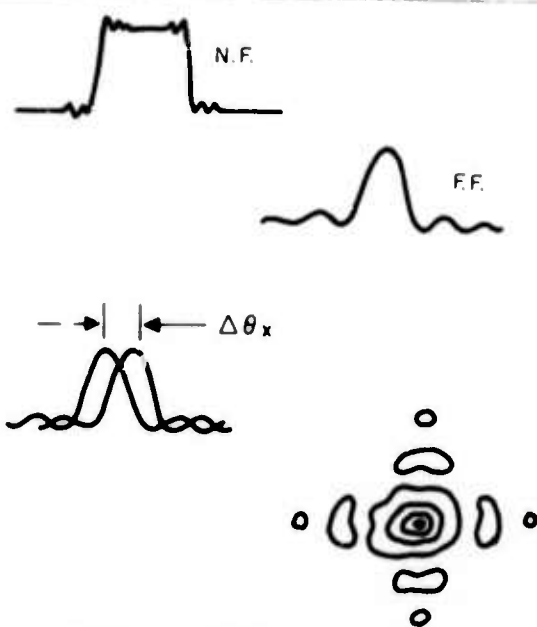


TABLE X  
COAT System Calibration - Temporal

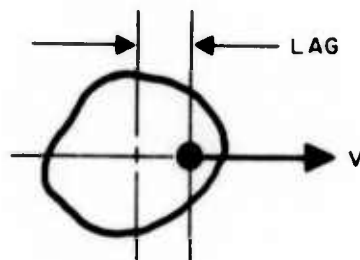
- Convergence Time and Open-Loop Gain for Each Control Loop in Two-Element Tests (Single-Glint)
- Convergence Time for the Entire Array for Each Array Variation and Target Configuration
- Beam Offset Control Characteristics for Both Microslewing Mirrors and Direct Element Phase Control

TABLE XI  
COAT System Calibration - Subsystems

- Control Loop Filter Transfer Function
- Control Phase Shifter Transfer Function
- AGC Compression and Frequency Response
- Microthermometer, Scintillometer, MTF "Round Robin" Comparison on Range
- T. V. and Glint Point Detector Response

TABLE XII  
Single-Glint Tests

- Determine Statistical Convergence Stability as a Function of Atmospheric Conditions
- Determine Convergence Stability as a Function of Glint Velocity



2406-24

TABLE XIII  
Static Multiple Glint Tests

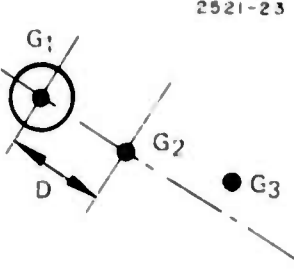
 <p>2521-23</p>	<ul style="list-style-type: none"> <li>• Determine smallest D</li> <li>• Determine limits</li> </ul> <p>on <math>\frac{G_1}{G_2}</math></p> <p>on <math>\frac{G_1}{\sum_{n=1}^N G_n}</math></p>
	<ul style="list-style-type: none"> <li>• Determine size, duration of time-varying glint <math>G_2(T)</math> to capture; hold</li> <li>• Relate glint switching statistics to <math>C_n^2</math></li> </ul>

TABLE XIV  
Moving Multiglint tests

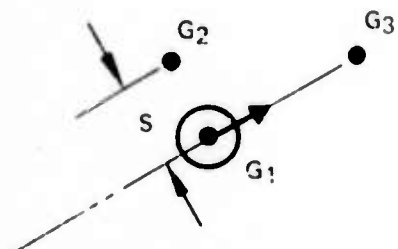
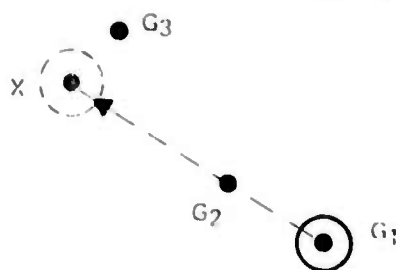
 <p>2521-22</p>	<ul style="list-style-type: none"> <li>• Determine distance S to capture COAT System if <math>G_1 \approx G_2</math></li> <li>• Determine strength of <math>G_3</math> necessary to capture. What does system do as <math>G_1</math> passes through <math>G_3</math>?</li> </ul>
--	--

TABLE XV  
Beam Offset/Scan Tests

2521-21	<ul style="list-style-type: none"><li>• Determine effects of <math>G_2</math> in path to aim point X.</li><li>• Determine effects of <math>G_3</math> nearby desired aim point X.</li><li>• Determine reacquisition time of <math>G_1</math> as a function of offset control strategy.</li></ul>
---------	--



S E C T I O N V  
PLANS FOR THE NEXT QUARTER

The next quarter, July through September, will be taken up fully with equipment fabrication. The computer simulation program will be used to predict system performance for the conditions expected in the measurements program.

**Preceding page blank**

## APPENDIX I

### INCREMENTAL OPEN LOOP GAIN

Incremental open loop gain (IOLG) in the  $m^{\text{th}}$  channel of an  $N$ -channel COAT system is determined by the incremental change of the  $m^{\text{th}}$  low-pass filter output in response to an incremental voltage applied to the  $m^{\text{th}}$  bias phase shifter. The single channel loop considered in determining IOLG is shown in Fig. I-1. The total field incident on the  $i^{\text{th}}$  target glint is given by<sup>1</sup>

$$E_i = \sum_{m=1}^N E_{mi} \cos(\psi_m + \phi_{mi}) = \operatorname{Re} \sum_{m=1}^N E_{mi} e^{i(\psi_m + \phi_{mi})} \quad (1)$$

where  $\operatorname{Re}$  denotes the "real part of" and

$E_{mi}$  = electric field amplitude at  $i^{\text{th}}$  glint from the  $m^{\text{th}}$  array element

$\psi_m$  =  $\psi_o \sin \omega_m t$  = dither phase modulation

$\phi_{mi}$  = (bias phase) + (propagation phase change)

= total phase change in  $m^{\text{th}}$  channel to  $i^{\text{th}}$  glint

The total phase change can also be written as

$$\phi_{mi} = k(L_{mi} + K_B V_{Bm}) \quad (2)$$

where  $k = 2\pi/\lambda$  is the optical wave vector,  $L_{mi}$  is the optical path length from the  $m^{\text{th}}$  array element to the  $i^{\text{th}}$  glint,  $K_B$  is the phase-shifter constant (volts/meter), and  $V_{Bm}$  is the voltage applied to the  $m^{\text{th}}$  phase shifter.

The total field reradiated by all the target glints and incident on the receiver is

---

<sup>1</sup>The essentials of the following derivation are also given in the Appendices of Hughes Technical Proposal 73M-3186/C8902, COAT Planar Array, January 1973.

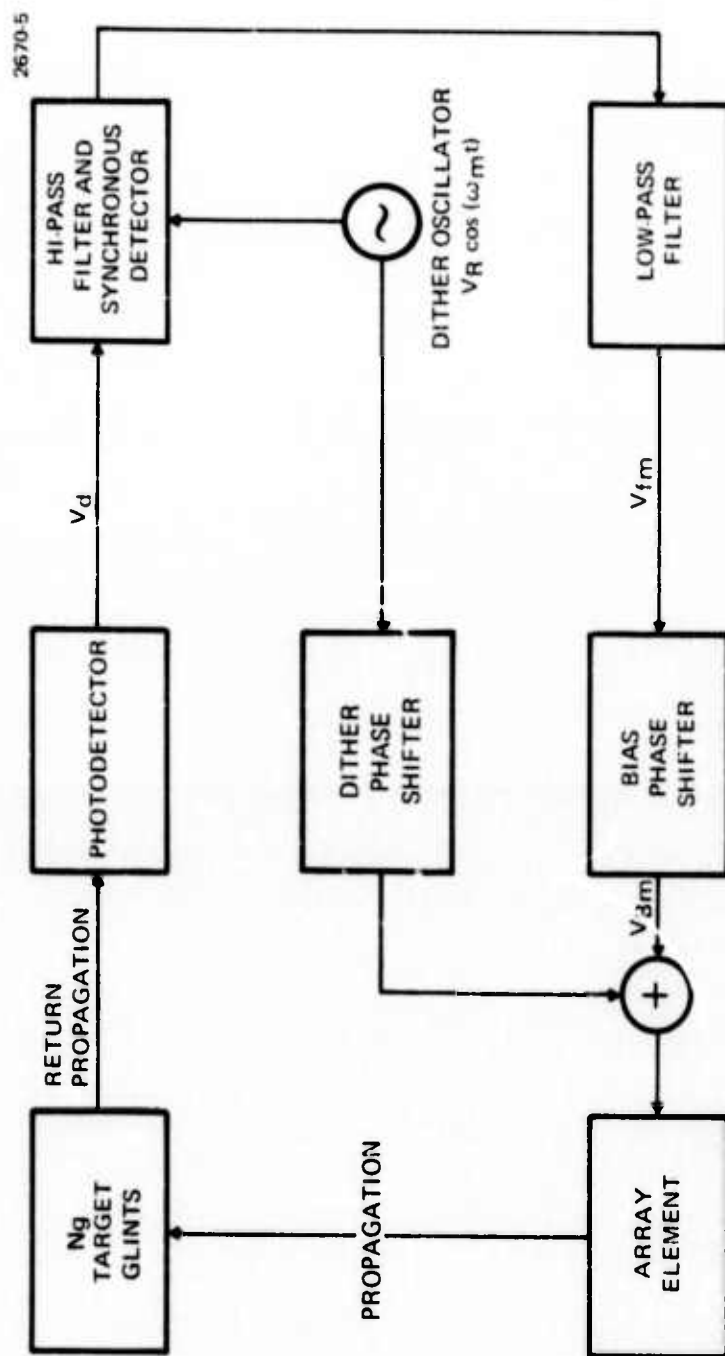


Fig. I-1. Single channel ( $m^{\text{th}}$ ) of an  $N$ -channel COAT signal processing loop.

$$E_R = \sum_{i=1}^{N_g} E_i \rho_i \frac{\exp(ik|\underline{x} - \underline{x}_i|)}{|\underline{x} - \underline{x}_i|} \quad (3)$$

where  $\rho_i$  is the complex amplitude reflectivity of the  $i^{\text{th}}$  glint,  $\underline{x}$  defines the receiver plane and  $\underline{x}_i$  is the location of the  $i^{\text{th}}$  glint in the target plane referred to an arbitrary origin. If the receiver is placed at the origin of the coordinate system, and all glints are assumed to lie in a plane which is parallel to the plane of the receiver, then for large distances we can express  $|\underline{x} - \underline{x}_i|$  as

$$\begin{aligned} |\underline{x} - \underline{x}_i| &\approx z - z_i + \frac{|\underline{x}_T - \underline{x}_{Ti}|}{2(z - z_i)} \\ &\approx R_o + \frac{|\underline{x}_T|^2}{2z} - \frac{\underline{x}_T \cdot \underline{x}_{Ti}}{z} + \frac{|\underline{x}_{Ti}|^2}{2z} \end{aligned} \quad (4)$$

where  $R_o$  is the range (distance between receiver and target planes, and the subscript, T, refers to the transverse coordinates, x and y, referred to the boresight axis. Note that  $|\underline{x}_{Ti}|$  is the distance of the  $i^{\text{th}}$  glint from the boresight axis.

The received intensity is found by integrating  $|E_R|^2$  over the receiver aperture:

$$I \propto \int_{\substack{\text{rcv'r} \\ \text{aperture}}} |E_R|^2 dx_T \quad (5)$$

Using Eq. (3) in Eq. (5), and performing the integrations for a circular receiver aperture gives

$$P = \frac{2\pi a^2}{Z_o^2 R_o^2} \sum_{i,j=1}^{N_g} E_i E_j^* \rho_i \rho_j^* \frac{J_1\left(\frac{ka}{R_o} |\underline{x}_{Tj} - \underline{x}_{Ti}| \right)}{\frac{ka}{R_o} |\underline{x}_{Tj} - \underline{x}_{Ti}|} \quad (6)$$

where  $Z_o = 377$  ohms,  $N_g$  is the number of glints,  $a$  is the receiver aperture radius, and

$$|\underline{x}_{Ti} - \underline{x}_{Tj}| = |\underline{x}_{Ti}|^2 + 2 \underline{x}_{Ti} \cdot \underline{x}_{Tj} + |\underline{x}_{Tj}|^2$$

Equation (6) together with equation (1) contains all the propagation and coherence effects which result from a multi-element transmitting array and a multi-glint target. The effects of receiver aperture size are also included.

The photodetector output is proportional to  $P$ , a high-pass filter removes the dc component, and a synchronous detector selects out the component at  $\omega_m$ . The output of the  $m^{\text{th}}$  low-pass filter for small dither amplitudes is then

$$V_{fm} = C_m' \sum_{i,j=1}^{N_g} \sum_{\substack{n=1 \\ n \neq m}}^N f_{ij}(\underline{x}_T) E_{mi} E_{nj} \sin(\phi_{mi} - \phi_{nj}) \quad (7)$$

where

$$C_m' = \frac{\pi a^2}{Z_o R_o^2} G_{LM} G_H K_d V_R C_S \psi_o$$

$G_{LM}$  = gain of  $m^{\text{th}}$  low-pass filter at  $\omega_m$

$G_H$  = gain of high pass filter

$K_d$  = photodetector constant in meters/volts

$V_R$  = reference voltage applied to the synchronous detector

$C_S$  = 1 for sine-wave synchronous detection or  $\pi/4$  for square-wave detection

$\psi_o$  = dither amplitude

$$f_{ij}(\underline{x}_T) = \rho_i \rho_j^* \frac{J_1\left(\frac{ka}{R_o} |\underline{x}_{Tj} - \underline{x}_{Ti}|\right)}{\frac{ka}{R_o} |\underline{x}_{Tj} - \underline{x}_{Ti}|}$$

The incremental open loop gain in dB in the  $m^{\text{th}}$  channel can now be written as

$$(IOLG)_m = 20 \log \left| \frac{dV_{fm}}{dV_{Bm}} \right| \quad (8)$$

Using equations (2) and (7), we can write

$$\frac{dV_{fm}}{dV_{Bm}} = C_m \sum_{ij=1}^N g_{ij} \sum_{\substack{n=1 \\ n \neq m}}^N f_{ij}(x_T) E_{mi} E_{nj} \cos(\phi_{mi} - \phi_{nj}) \quad (9)$$

where  $C_m = kK_B C_m'$ . Equations (2), (5), and (9) constitute the desired result for IOLG.